

SCANNING TRANSMISSION X-RAY MICROSCOPY

**X-RAY MAGNETIC CIRCULAR DICHROISM
OF INDIVIDUAL MAGNETOSOMES IN
MAGNETOTACTIC BACTERIA BY
SCANNING TRANSMISSION X-RAY
MICROSCOPY**

By

KAREN LAM, B.Sc.

A Thesis

Submitted to the School of Graduate Studies

in Partial Fulfillment of the Requirements

for the Degree

Master of Science

McMaster University

© Copyright by Karen Lam, March 2010

MASTER OF SCIENCE (2010)
(Chemistry and Chemical Biology)

McMaster University
Hamilton, Ontario

TITLE: X-ray Magnetic Circular Dichroism of Individual
Magnetosomes in Magnetotactic Bacteria by Scanning
Transmission X-ray Microscopy

AUTHOR: Karen Lam, B.Sc. (University of Toronto)

SUPERVISOR: Professor A. P. Hitchcock

NUMBER OF PAGES: xx, 134

ABSTRACT

Magnetotactic bacteria (MTB) produce single-domain nano-crystals (typically 30-60 nm in size) of magnetite (Fe_3O_4) or greigite (Fe_3S_4) enclosed in a biomembrane. Known as magnetosomes, these chains of ferrimagnetic nanocrystals, each comprising a single magnetic dipole, allow MTB to align themselves with respect to the earth's magnetic field, and then migrate to their preferred habitat at the oxic-anoxic transition zone of aquatic environments. Recently, magnetotactic bacteria and magnetosomes have received much attention for their potential in various medical, environmental, biotechnological and technological applications as nano-magnetic material. Using the soft X-ray scanning transmission X-ray microscopes (STXM) at the Canadian Light Source (Saskatoon) and Advanced Light Source (Berkeley, CA), the magnetic properties and biochemistry of the magnetosomes were studied at high spatial resolution (30 nm). In order to probe the permanent magnetic moment and magnetic orientation of individual magnetosomes, X-ray magnetic circular dichroism (XMCD) was used.

Although this technique has previously been applied to ensembles of magnetotactic bacteria as reported in the literature, the work presented in this thesis marks the first time that Fe $L_{2,3}$ XMCD signal was measured from single 30-nm diameter Fe_3O_4 magnetosomes in individual MTB, in particular, those of a marine vibrio, strain MV-1 [1]. Furthermore, recent major improvements to the

STXM data acquisition process have allowed measurement of much higher quality XMCD data, by using XMCD-stacks in which the left and right circularly polarized signals are measured alternately at each photon energy. As well, the associated biochemistry was explored by speciation and quantitative biochemical mapping at the Cls and Ols absorption edges. Studies on magnetotactic bacteria will lead to a deeper understanding of the genetic and environmental factors and mechanisms involved in magnetosome chain formation, which may be a precursor to understanding biomineralization processes present in higher-level organisms, such as birds and bees.

[1] KP Lam *et al.* (2010), *Chem. Geol.* 270, 110.

ACKNOWLEDGEMENTS

First and foremost, I would like to express my sincerest gratitude to my supervisor, Professor Adam Hitchcock. Not only did he allow me to embark on such an incredible learning journey with him, but he has been most supportive, trusting and encouraging throughout. One of the most important lessons that I have learned from Professor Hitchcock through this journey is not how to work effectively and write concisely (on which I am still working!), but how to tackle challenges from a different angle (literally), how to be open-minded to trying the new and the unknown, and most importantly, how to persevere through difficulties with enthusiasm and optimism. Thank you, Professor Hitchcock, for your patience in guiding and taking an inexperienced, such as myself, under your wing; and for being there to pull me through times of disappointment and struggles, and leading me to uncover surprises and find success. And of course, thank you for having to endure all the tedious proofreading of drafts of this thesis!

Secondly, I would like to thank Dr. Gillian Goward for attending my committee meetings, allowing me to present my research to her, and most of all, for taking the time to understand my research in order to give me helpful advice, suggestions and constructive feedback. Furthermore, the success and completion of this project would not have been possible without the valuable contributions of my collaborators - whether it be advice or assistance in sample preparation and/or culturing (Martin Obst, John Lawrence, George Swerhone and Gary Leppard);

technical development, assistance and support at the ALS or CLS beamline facilities (Tolek Tyliczszak, Chithra Karunakaran, Jian Wang); and the provisioning of candidate and promising samples to even allow the work and measurements in this thesis to be carried out at all (Olav Hellwig & Eric Fullerton (Hitachi Global Storage Technologies), Jeff Kortright, Arash Komeili, and Professors Dennis Bazylinski and Ulysses Lins). As well, I must thank the kind assistance of those whom I have met along the way, including Marcia West (TEM assistance), Lindsay Kalan (assistance with cell culturing at McMaster) and Neil Telling (provider/developer of Q-Fit software program). NSERC is thanked for financial support.

Finally, a big thank you goes out to all of my past and current group members, or group “brothers” (Glyn Cooper, Ebi Najafi, Jeffrey Li, Adam Leontowich, Sam Kalirai) and “sisters” (Bonnie Leung, Katie Harding, Anne-Marie Smith) as I prefer to call them, for providing me with such a comfortable, friendly and supportive working atmosphere; and for contributing to stimulating group discussions in which you offered fresh ideas (eg. Bonnie, thanks for suggesting the practical concept of the wedge sample mount! It works very well!). Also, I would like to thank all of my friends both on and off campus for always listening and being my cheerleaders. Last but not least, I cannot even begin to thank my family, especially my parents – for their unconditional love for me, for being so supportive and proud of my endeavours, and for always being

there for me, no matter what. Especially to my mother, thank you for the innumerable times that you have driven me in and out of Hamilton to and from Toronto (and even in and out of Mississauga, in my undergrad years) to allow me to maintain my weekend commitments. Despite the fact that I own a multiple-ride GO bus pass, you continue insisting to drive me to prevent me from waiting for buses and commuting late at night. I dedicate this thesis to you.

TABLE OF CONTENTS

Preliminaries	Page
Descriptive Note.	ii
Abstract	iii
Acknowledgements	v
Table of contents	viii
List of Figures.	xii
List of Tables	xvii
List of Abbreviations and Symbols	xviii
Chapter 1 INTRODUCTION	1
1.1 Magnetotactic bacteria (MTB)	2
1.1.1 History	2
1.1.2 Properties and function of magnetosomes	5
1.1.3 Composition and structure of magnetosomes.	14
1.1.4 Biomineralization of magnetosomes	16
1.1.5 Techniques applied to the study of magnetic properties of magnetosomes.	19
1.2 Magnetite: Crystal, electronic and magnetic structures	20
1.3 X-ray Magnetic Circular Dichroism (XMCD)	22
1.3.1 History of X-ray magnetic dichroism	22
1.3.2 XMCD at $L_{2,3}$ edges	24
1.3.3 Fe $2p$ $L_{2,3}$ XMCD of magnetite	26
1.3.3.1 XMCD of biogenic magnetite	29
1.4 Why study MTB and magnetosomes?	31
1.5 Goals of thesis.	34

Chapter 2	METHODS	35
2.1	Synchrotron radiation	36
2.2	Scanning Transmission X-ray Microscopy (STXM)	36
2.2.1	Instrumentation, spatial and energy resolution of STXM	38
2.3	X-ray Absorption Spectroscopy (XAS)	43
2.3.1	Near Edge X-ray Absorption Fine Structure (NEXAFS)	45
2.3.2	X-ray Magnetic Circular Dichroism (XMCD)	46
2.3.1.1	Properties and production of circularly polarized X-rays	49
2.3.1.2	XMCD of Co-Pt test samples to demonstrate CLS ability	52
Chapter 3	EXPERIMENTAL	54
3.1	Sample preparation.	55
3.2	Data acquisition procedure	59
3.2.1	STXM measurements	59
3.2.2	Sample mounting	64
3.2.3	XMCD measurement	66
3.2.3.1	XMCD maps	66
3.2.3.2	Fe 2 <i>p</i> spectroscopy of magnetite	69
3.2.3.3	XMCD stacks	71
3.3	Data processing and analysis	72
3.3.1	Image alignment	72
3.3.2	Maps: on/off elemental and XMCD	75
3.3.3	I ₀ Region	77
3.3.4	Extracting XMCD from image sequences	79
3.3.5	Verification of data	80

3.3.6	Spectral fitting (Q-Fit) for determining site occupancies	81
3.4	Sequence of experimental studies	82
Chapter 4	CHARACTERIZING MAGNETISM OF INDIVIDUAL MAGNETOSOMES BY X-RAY MAGNETIC CIRCULAR DICHROISM IN A SCANNING TRANSMISSION X-RAY MICROSCOPE	85
4.1	Introduction.	86
4.2	Materials & Methods	87
4.2.1	Growth and preparation of bacteria	87
4.2.2	Fe $L_{2,3}$ X-ray magnetic circular dichroism (XMCD)	87
4.2.3	Data analysis	88
4.3	Results	88
4.4	Discussion.	90
Chapter 5	ADDITIONAL STUDIES.	93
5.1	Improved XMCD using XMCD-scanning	94
5.2	Fe in cytoplasm of MV-1	96
5.3	Biochemical studies by C-N-O NEXAFS	98
Chapter 6	SUMMARY & FUTURE WORK.	102
6.1	Summary and significance of work	103
6.2	Future directions	105
6.2.1	Study of other MTB strains	105
6.2.2	Investigation of magnetosome anomalies	106
6.2.3	Outlook	108

APPENDICES.	109
A.1 Collection of MTB cells from Princess Point/Hamilton Harbour	109
A.2 Preparation of MTB Growth Medium: Liquid and Semisolid Media	110
A.3 STXM Measurements on Multi-cellular Magnetotactic Prokaryote (MMP)	112
A.4 Preliminary STXM Measurement on a Magnetite- and Greigite-Producing Magnetotactic Bacterium	115
A.5 Data analysis using Q-Fit	117
A.6 Magnetosome anomalies	119
REFERENCES.	123

LIST OF FIGURES

<i>Label</i>	<i>Description</i>	<i>Page</i>
Chapter 1		
Fig. 1.1	Electron micrograph of thin-sectioned magnetotactic cells of strain MS-1.	5
Fig. 1.2	Electron hologram of a region of the magnetosome chain in <i>Magnetospirillum Magnetotacticum</i> , strain MS-1.	8
Fig. 1.3	Schematic showing how polar magneto-aerotaxis keeps cells at the preferred oxygen concentration in the oxic-anoxic transition zone (OATZ) in chemically stratified water columns and sediments.	10
Fig. 1.4	Schematic depicting the formation of magneto-aerotactic bands in flat capillary tubes with both ends open placed in a magnetic field, H.	12
Fig. 1.5	Dark-field STEM and brightfield scanning-transmission electron micrographs of a rod-shaped magnetotactic bacterium showing tooth-shaped magnetite (Fe_3O_4) and pleomorphic greigite (Fe_3S_4) magnetosomes co-organized within the same chains.	14
Fig. 1.6	Example of some of the magnetosome crystal habits found in magnetotactic bacteria.	15
Fig. 1.7	Schematic of possible reactions leading to magnetite biomineralization in known, cultured species of magnetotactic bacteria.	18
Fig. 1.8	The crystal system of spinels in the Face Centered Cubic (FCC) unit cell.	21
Fig. 1.9	The structure of a ferrite spinel showing the octahedral and tetrahedral sites.	22
Fig. 1.10	Illustration of the XMCD effect in Fe.	26

Fig. 1.11	XAS of magnetite (Fe_3O_4) recorded at left and right circular polarizations of light and calculated Fe components of the XMCD spectrum of magnetite.	28
-----------	---	----

Chapter 2

Fig. 2.1	Plan view of the CLS soft x-ray spectromicroscopy beamline, in which STXM is located.	38
Fig. 2.2	Schematic of the operation of STXM.	39
Fig. 2.3	Focusing scheme in STXM.	39
Fig. 2.4	Illustration of the x-ray magnetic circular dichroism process.	48
Fig. 2.5	Circularly polarized light comprises two perpendicular electromagnetic plane waves of equal amplitude with a 90° phase shift and is characterized by a rotating electric field vector.	51
Fig. 2.6	Schematic illustrating the importance of in-plane magnetized samples to be tilted/rotated for the detection of XMCD.	51
Fig. 2.7	STXM images and XMCD spectra of a Co-Pt multilayer test sample at the Co $L_{2,3}$ edges.	53

Chapter 3

Fig. 3.1	The progression of various different MTB sample preparations in attempts to minimize cell lysis.	59
Fig. 3.2	Photo of the tomography rotation stage, along with the inserted tomo stub containing a mounted TEM grid; and a zoomed-in view of the geometry and configuration of the ZP, OSA, sample and tomo stage components within STXM.	65
Fig. 3.3	Wedge dimensions and zoomed-out view of wedge mounted on a sample plate.	66
Fig. 3.4	Screenshot of the STXM control window.	67

Fig. 3.5	Fe L_3 spectra of magnetite measured with the magnetic moment aligned parallel and anti-parallel to the helicity of circular polarized x-rays, with the resulting XMCD difference spectrum plotted along the bottom.	70
Fig. 3.6	Illustration of the effect of magnetosome chain orientation on the detection of the in-plane magnetic moment.	71
Fig. 3.7	Two images from an image sequence showing drift in the field of view over time.	73
Fig. 3.8	Image distortion occurring in a pair of discrete XMCD stacks.	74
Fig. 3.9	Single component mapping of Fe in MV-1 cells.	76
Fig. 3.10	Example of an XMCD map.	76
Fig. 3.11	A STXM image showing an appropriate internal I_0 region within the field of view.	78
Fig. 3.12	XMCD difference images generated by the subtraction of one stack at a given polarization from the other.	80
Fig. 3.13	Illustration of the effect of sample geometry on the magnitude of the measured XMCD signal relative to the intrinsic in-plane XMCD signal.	81

Chapter 4

Fig. 1	Color composite of two STXM images of intact cells of strain MV-1.	88
Fig. 2	(a) Fe $L_{2,3}$ optical density image at 709.3 eV of several MV-1 magnetosome chains (recorded with horizontal linear polarization). (b) The sum of 10 OD images in the region of the Fe L_3 peak (706-708 eV) minus the sum of 14 images in the pre-Fe $L_{2,3}$ region (697-704 eV). (c) Expansion of the Fe $L_{2,3}$ image of two MV-1 magnetosomes (different region of the same sample). (d) 3D presentation of the signal in 3(c), using an e^{OD} scaling showing distinct resolution of adjacent magnetosomes at the 8% contrast level.	89

Fig. 3	Fe L _{2,3} spectrum of nine magnetosomes from one horizontal chain recorded with circularly polarized light parallel and anti-parallel to the magnetic moment of the sample, compared to that of magnetite.	89
Fig. 4	Overplot of the average spectra of 9 magnetosomes in a horizontal chain recorded with circularly polarized X-rays parallel and anti-parallel to the magnetic moment of the sample.	89
Fig. 5	Spectra of 4 individual magnetosomes in the horizontal chain - at both circular polarizations of light, with the resulting XMCD signal superimposed on a scaled XMCD signal of magnetite.	90

Chapter 5

Fig. 5.1	Comparison of EPU-phase changes and the resulting acquired LCP/RCP spectra before and after August 2009.	95
Fig. 5.2	(a) A non-rescaled overplot of the magnetosomal and cytoplasmic spectra; (b) cytoplasmic spectra measured at both polarizations reveal no XMCD; (c) a rescaled overlay of the cytoplasmic and magnetosome spectra.	97
Fig. 5.3	Spectra of MV-1 measured at the C1s and O1s edges, compared against reference spectra of various biological components.	99
Fig. 5.4	Spectral comparison (using Zimba) of various components present in the MV-1 sample.	100
Fig. 5.5	Three-component RGB mapping allows for visual differentiation of different chemical components present in the sample.	101

Appendices

Fig. A.1	Fe maps of MMP show that the magnetosomes are arranged in multi-chain arrays, located near the periphery of the entire cell cluster.	114
Fig. A.2	Spectra of MMP measured at the C1s and O1s edges, compared against reference spectra of various biological components.	114
Fig. A.3	Left: Iron mapping on two overlapping cells of a magnetite- and greigite-producing MTB. Centre: Zoomed-in image shows irregularity in both the morphology and alignment of magnetosomes. Right: Oxygen mapping reveals differential composition of magnetosomes within the same chain.	116
Fig. A.4	Examples of spectral fitting of magnetosome (magnetite) spectra using Q-Fit.	118
Fig. A.5	XMCD spectra measured for two overlapping magnetosome chains of distinct cells.	120
Fig. A.6	XMCD spectra revealing opposing directionality in the magnetic moments of overlapping magnetosome chains.	121
Fig. A.7	XMCD images at each of the peak energies in the magnetite XMCD spectrum.	122
Fig. A.8	An interesting magnetosome anomaly – the observation of a circular arrangement of magnetosomes in MV-1.	122

LIST OF TABLES

Chapter 1

Table 1.1	Summary of different types of magnetism	6
Table 1.2	Summary of literature XMCD studies on biogenic magnetite	30

Chapter 3

Table 3.1	EPU control codes	68
Table 3.2	Sequence and summary of experimental studies	83-84

LIST OF ABBREVIATIONS AND SYMBOLS

Å	Angstrom
A_1	Experimentally determined constant parameter in STXM focussing
A_0	Distance between sample and order-sorting aperture
ALS	Advanced Light Source
AMB-1	<i>Magnetospirillum magneticum</i> (bacterial strain)
ATCC	American Type Culture Collection (bioresource centre)
B	Magnetic Field
CLS	Canadian Light Source
CXRO	Center for X-Ray Optics
δ_{rN}	Width of the Most Outer Zone (Nth) of a Zone Plate
$\Delta\delta$	Deviation in Site Occupancy from Stoichiometry
Δr	Diffraction Limited Spatial Resolution
D	Zone Plate Diameter
E	Energy
emu	Electromagnetic Unit
erg	unit of energy or work (centimeter-gram-second system)
f	Focal Length
FOV	Field of View
G	Gauss
H	Magnetic Field Strength
HOMO	Highest Occupied Molecular Orbital
I_t	Transmitted Photon Intensity
I_0	Incident Photon Intensity
K	Kelvin (unit of temperature)
k_B	Boltzmann constant, 1.38×10^{-16} erg/K

λ	Wavelength of light
LCP	Left Circular Polarization (Polarized Light)
LUMO	Lowest Unoccupied Molecular Orbital
M	Magnetic Moment
MC-1	<i>Magnetococcus sp.</i> (bacterial strain)
$\mu(E)$	Energy Dependent Mass Absorption Coefficient
MMP	Multi-cellular Magnetotactic Prokaryote
MS-1	<i>Magnetospirillum magnetotacticum</i> (bacterial strain)
MSR-1	<i>Magnetospirillum gryphiswaldense</i> (bacterial strain)
MTB	Magnetotactic Bacteria
MV-1	Marine Vibrio (bacterial strain)
NEXAFS	Near Edge X-Ray Absorption Fine Structure
NS	North-Seeking (bacterial motility)
NWRI	National Water Research Institute
OATZ	Oxic-Anoxic Transition Zone
OD	Optical Density
OSA	Order Sorting Aperture
PBS	Phosphate-Buffered Saline Solution
PGM	Plane-grating Monochromator
RCP	Right Circular Polarization (Polarized Light)
ROI	Region of Interest (in STXM images)
rpm	Revolutions per Minute
ρ	Sample Density
σ	Energy-dependent Mass Absorption Coefficient
s	Second
SGM	Spherical-grating Monochromator
SS	South-Seeking (bacterial motility)
STXM	Scanning Transmission X-Ray Microscopy

SVD	Singular Value Decomposition
t	Sample Thickness
T	Temperature
TEM	Transmission Electron Microscopy
TEY	Total Electron Yield
UNLV	University of Nevada, Las Vegas
XAS	X-ray Absorption Spectroscopy
XANES	X-ray Absorption Near Edge Structure
XMCD	X-Ray Magnetic Circular Dichroism
XMLD	X-Ray Magnetic Linear Dichroism
ZP	Fresnel Zone Plate

Chapter 1

INTRODUCTION

This chapter is a brief survey of magnetotactic bacteria, as well as the x-ray magnetic circular dichroism (XMCD) technique used to study their magnetic properties. Progress and development of research in these fields, including their current applications, are discussed. This chapter concludes with a description of the goals for this thesis and the significance of the work to the field of magnetotactic bacteria.

1.1 Magnetotactic Bacteria (MTB)

1.1.1 History

Magnetotactic bacteria (MTB) are motile, aquatic, Gram-negative and microaerophilic bacteria that can migrate and orient themselves with respect to the earth's magnetic field. Existing in various morphologies, including cocci, short or long rods, vibrios, spirilla and multicellular forms, magnetotactic bacteria are ubiquitous in sediments from diverse aquatic environments (eg. Marine habitats, lakes, rivers, ponds, estuary, deep sea, wet soil, etc.). Yet, due to their fastidious nature, only a few MTB species are capable of being grown in pure culture.

Microbiologist Richard P. Blakemore first reported evidence of magnetotactic bacteria (Blakemore 1975). From Blakemore's discovery and subsequent published works, the study of these exotic bacteria has blossomed and incited interest in many diverse disciplines. In the past 30 years, research has shed light on their special magnetic properties, their behaviour and mechanisms of motility as influenced by the presence of an external magnetic field, as well as their physiological and biomineralization processes. Today, there is an ever-growing interest to exploit the magnetic properties and capabilities of magnetotactic bacteria for applications in environmental, technological and biotechnological industries (Faivre and Schüler, 2008).

Although Blakemore is generally credited as first to discover and publish on magnetotactic bacteria, and is given much attention and acknowledgement for

his initial ground-breaking findings in this field, it has recently come to light that MTBs had also been discovered previously and separately by an MD, Salvatore Bellini, at the University of Pavia in Italy. Bellini's written accounts of magnetotactic bacteria date back to 1963 and are considered to be the first observation of MTB. His documents consist of two manuscripts, which only appeared in a publication of the University of Pavia's Institute of Microbiology. However, following the 'finding' of these original manuscripts in 2007 (Frankel 2009) by Dr. Henrique Lins de Barros (Brazil) and Prof. Dennis A. Bazylinski (USA), they were translated from the original Italian into English, edited for scientific clarity by Prof. Richard B. Frankel (USA), and published (Bellini 2009a, 2009b).

Bellini's first manuscript (2009a) describes the observation of a group of bacteria which migrated consistently towards the North end of water drops on microscope slides. At the time, Bellini named this phenomenon as "magnetosensitivity". Other observations described in this document include: a) application of an external magnetic field greater than the geomagnetic field to control the direction of the bacterial migration; b) dead cells continue to align themselves with the magnetic field although there is no migration; c) cells placed in demineralized solutions showed significant decrease or even complete loss of magnetosensitivity, which was restored by the addition of soluble iron salts of up to 3 mg/L. From these observations, Bellini concluded: a) the presence of a

biomagnetic “compass” within the bacterial cells; b) that iron compounds are responsible for the bacteria’s magnetosensitive behaviour; c) the magnetosensitive behaviour in the bacteria could have evolved in response to the amount of oxygen in the environment; d) that bacteria present in the southern hemisphere should swim toward the magnetic south. Bellini’s follow-up ‘magnetic’ and aerobic vs. anaerobic experiments on these bacteria (Bellini 2009b) hypothesizes that bacterial magnetic orientation is linked to the search of optimal low-oxygen environments preferred by these bacteria. Bellini’s observations are consistent with those of Blakemore and others.

In 1975, Blakemore collected surface sediments from the marine marsh muds of Cape Cod and Buzzards Bay (Massachusetts) in attempts to isolate a bacteria, *Spirochaeta plicatilis*. Like Bellini, he observed the migration of microorganisms towards one side of the mud droplets on the microscope slides and confirmed this to be a response to the Earth’s magnetic field. Blakemore first introduced the term “magnetotaxis” to describe this phenomenon (Blakemore 1975), which, he defined as “cell motility directed by a magnetic field” (Blakemore 1982). In his 1975 paper, Blakemore further noted that there were several morphologically distinct types of the magnetotactic organisms ranging in size from 1-3 μm . Each type contained one or more intracellular chains consisting of five to ten electron-dense, iron-rich, crystal-like particles, now known as magnetosomes. The size, number and shape of the magnetosomes

depend on the cell type. The chains of iron-rich crystal inclusions in *Aquaspirillum magnetotacticum* (strain MS-1) were first analyzed by Mössbauer spectroscopy, which revealed they are magnetite (Fe_3O_4), also known as lodestone (Frankel *et al.* 1979, see Figure 1.1). Magnetite is a ferrimagnet – the types of magnetic material are summarized in Table 1.1. Thus, Blakemore's work confirmed that magnetosomes are the agent responsible for magnetotactic behaviour (Balkwill *et al.* 1980).

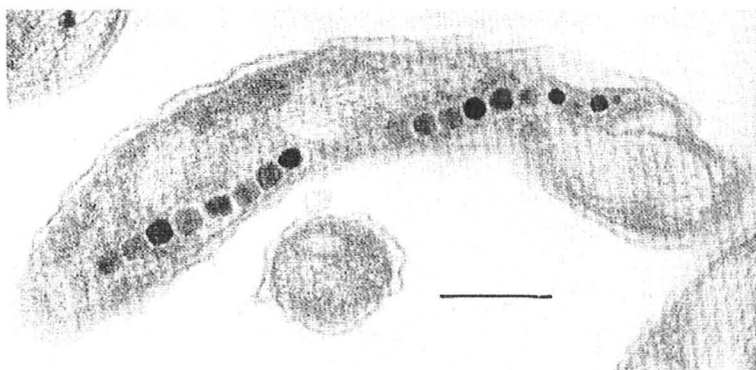


Figure 1.1 – Electron micrograph of thin-sectioned magnetotactic cells of strain MS-1. Chains of crystals known as magnetosomes are observed within the cell. Scale bar: 250 nm (Frankel *et al.*, 1979; Figure reproduced with permission from the *American Association for the Advancement of Science (AAAS)*).

1.1.2 Properties and function of magnetosomes

Magnetosomes are single crystals with sizes between 35 and 120 nm (Bazylinski *et al.*, 1994), which is within the single magnetic domain size range of 40-100 nm (Butler & Banerjee, 1975; Dunlop, 1973; Kirschvink & Lowenstam, 1979; Muxworthy & Williams, 2006). Smaller superparamagnetic (see Table 1.1)

Table 1.1 – Summary of different types of magnetism

Type of Magnetism	Characteristics	Illustration	Examples
Diamagnetism	Weak and negative susceptibility to an applied magnetic field		Non-magnetic substances; Graphite, water, wood, living tissue, silver, gold
Paramagnetism	Weak and positive susceptibility to an applied magnetic field		Aluminum, copper, platinum
Ferromagnetism	Strong and positive susceptibility to an applied magnetic field due to parallel alignment of equal magnetic moments		Iron, nickel, cobalt
Antiferromagnetic	No net magnetization due to antiparallel alignment of equal magnetic moments		Terbium
Ferrimagnetism	Strong and positive susceptibility to an applied magnetic field due to antiparallel alignment of unequal magnetic moments		Magnetite
Superparamagnetism	Large magnetic susceptibility and saturation of magnetization at strong magnetic fields		Ferro- or ferri- magnetic single-domain nanoparticles

particles may occasionally be present as well (Blakemore 1982). According to Jacobs & Bean (1955), single domain crystals in a chain will be aligned in a head-to-tail fashion such that the magnetic axis of each crystal will be parallel. Thus, a chain of magnetosomes serves as a single magnetic dipole or “biomagnetic compass” for the cell (Frankel & Blakemore, 1980). The total magnetic moment of the chain is the sum of the magnetic moments of the individual particles (Blakemore 1982), which has been confirmed by magnetic measurements (Peninga *et al.*, 1995), magnetic force anisotropy (Proksch *et al.*, 1995) and electron holography (Dunin-Borkowski *et al.*, 1998, refer to Figure 1.2).

By considering the number of magnetosomes in a cell (which can range from 5 to 40 per cell), the size of the magnetosomes, and the known magnetic moment per unit volume of magnetite ($480 \text{ emu/cm}^3 = 480 \text{ erg/(G}\cdot\text{cm}^3)$), also known as the saturation magnetization value, Frankel *et al.* (1980) showed that the chain’s magnetic moment is large enough to align the cell with the earth’s magnetic field ($H = 0.5 \text{ Gauss}$) and overcome the Brownian motion which would lead to random orientation in water at ambient temperatures (300 K).

Magnetospirillum magnetotacticum (MS-1) has an average of 22 cuboidal magnetosomes each measuring 50 nm on a side (Figure 1.2). The magnetic moment (M) as calculated by Frankel *et al.* (1980) is $1.3 \times 10^{-12} \text{ erg/G}$ (or emu) per bacterium. In a 0.5-G geomagnetic field, the magnetic dipole energy ($E = M\cdot H = MH \cos \theta$, where θ is the angle between the magnetic moment and

magnetic field directions) of the cell would be 6.6×10^{-13} erg, which is greater than the thermal energy ($k_B T$, where $T = 300$ K) of 4.1×10^{-14} erg, by more than an order of magnitude.

Although magnetotactic bacteria orient along the geomagnetic field, it is important to note that alignment is passive such that the cells are not “pulled” towards either magnetic pole. This is verified by the fact that dead cells merely align, but are not moved by the magnetic field. On the other hand, “living cells behave like tiny, self-propelled magnetic compass needles” (Bazylinski and Frankel, 2004) and demonstrate magnetotaxis by means of their flagella, which

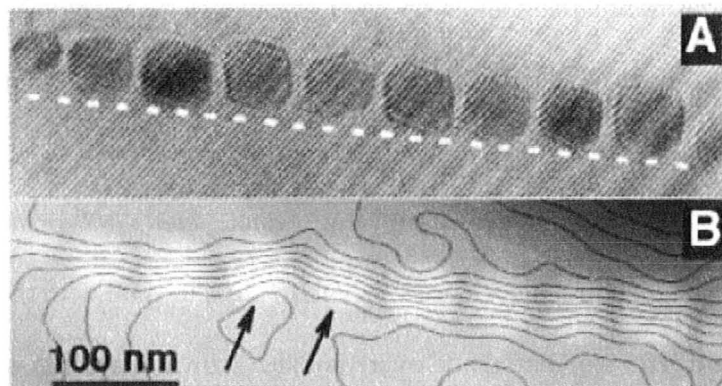


Figure 1.2 – Electron hologram of a region of the magnetosome chain in *Magnetospirillum Magnetotacticum*, strain MS-1. (A) Electron interference pattern with dotted line showing the slight offset of crystals from the chain axis. (B) The confinement of magnetic field lines derived from the interference pattern superimposed on the positions of the magnetosomes is indicative of single magnetic domains, with the entire chain of magnetosomes acting as a single magnetic dipole. (Dunin-Borkowski *et al.*, 1998; Figure reproduced with permission from the *American Association for the Advancement of Science (AAAS)*).

can be either polar, bipolar or tufts. Depending on the bacterial strain, the mechanism for magnetotaxis may be either polar or axial (Blakemore *et al.*, 1980). Polar magnetotaxis refers to the mechanism of unidirectional motility relative to the magnetic field, in which the bacteria are either North-seeking (NS) or South-seeking (SS), which is dependent on the magnetic dipole orientation in the cell (Blakemore *et al.*, 1980). On the other hand, axial magnetotaxis allows motility in both directions, towards the geomagnetic North and South (Bazylnski & Frankel, 2004). Furthermore, it is possible for the direction of the bacterial magnetic dipole to be reversed by strong magnetic pulses (300-600 Gauss for 1-2 μ s,) to induce an orientation antiparallel to the migration direction (Kalmijn & Blakemore, 1978).

Since the geomagnetic field has a radial component, NS and SS magnetotactic cells migrate along the inclined field lines towards the low-oxygenated sediments and away from the harmful high-oxygen concentrations in the surface waters, (Blakemore *et al.*, 1980; Kirschvink 1980). Thus, in each hemisphere, there is a predominant cell polarity found in the magnetotactic bacterial population. At the equator, roughly equal numbers of both polarities of magnetotactic bacteria are found, since the vertical component of the geomagnetic field at the equator is zero and therefore does not select for either polarity (Frankel *et al.*, 1981).

Donaghay *et al.* (1992) observed that magnetotactic cells are predominantly found at the oxic-anoxic transition zone¹ (OATZ) of chemically stratified water columns (Figure 1.3) rather than in the sediments. This suggested that OATZ provided optimal environmental conditions for the bacteria, which led to a revised hypothesis of magnetotaxis, in that optimal oxygen concentration is also a factor in the migration of the bacteria. In order to investigate the response of magnetotactic bacteria to oxygen-concentration gradients, experiments involving open-ended thin and flat capillary tubes were performed (Frankel *et al.*,

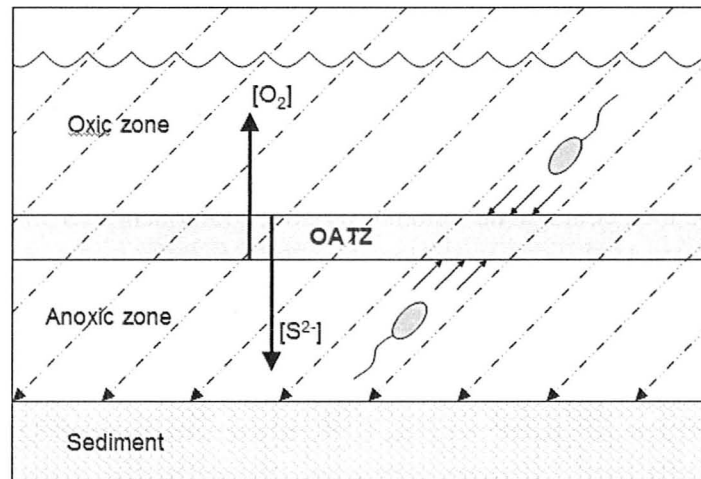


Figure 1.3 – Schematic showing how polar magneto-aerotaxis keeps cells at the preferred oxygen concentration in the oxic-anoxic transition zone (OATZ) in chemically stratified water columns and sediments.

¹ The oxic-anoxic transition zone is the boundary or horizontal interface between the O_2 (oxic) and S^{2-} (anoxic) concentration gradients present in chemically stratified water columns, sediments or marine environments. This is typically located at a depth of approximately 3-5 m in chemically stratified water columns (~20 m), in which both oxygen and hydrogen sulfide are present at low concentrations. This is a result of oxygen from the surface diffusing downwards and sulphide diffusing upwards from bacterial sulphate reduction processes in anaerobic sediment.

1997, refer to Figure 1.4). The open-ended tubes each created an oxygen-concentration gradient, in which $[O_2]$ increased from the centre of the tube to each end. When magnetotactic bacteria were introduced into the tubes, bands of bacteria were formed at a preferred or optimal $[O_2]$ in the tube, which were located somewhere in the region between the centre and either ends of the tube. The formation of such bands was evidence of aerotaxis, which is the migration of bacteria towards optimal oxygen concentrations.

When the tube was placed in a static magnetic field of a few gauss, differences in the behaviour of polar and axial magnetotactic bacterial strains were observed. In the case of polar magnetotactic bacteria, only a single aerotactic band was observed, while two bands were observed for axial magnetotactic bacteria. When the magnetic field was reversed, the polar bacteria migrated towards the optimal $[O_2]$ in the opposite direction, whereas the bands remained the same in the case of axial bacteria. These results have led the phenomenon of “magnetoaxis” to be renamed as “magnetoaerotaxis” in the case of oxygen-sensitive magnetotactic bacteria (Frankel *et al*, 1997). Magnetoaerotaxis simplifies the search for low-oxygen environments to a 1-D search rather than a 3-D search normally associated with other aerotactic organisms (Bazylinski and Frankel, 2004).

Farina *et al.* (1990) and Mann *et al.* (1990) reported that some bacteria in anoxic, anaerobic and sulfidic environments contained magnetosomes that are

composed of greigite (ferrimagnetic iron sulphide, Fe_3S_4). Given the anaerobic and sulfidic conditions in which greigite-producing magnetotactic bacteria are typically found (Rogers *et al.*, 1990; Bazylinski *et al.*, 1993a), it is thought that the production of Fe_3S_4 occurs in the absence of oxygen. Several considerations arose from these findings: 1) diagenesis of biogenic minerals (ie. magnetite and

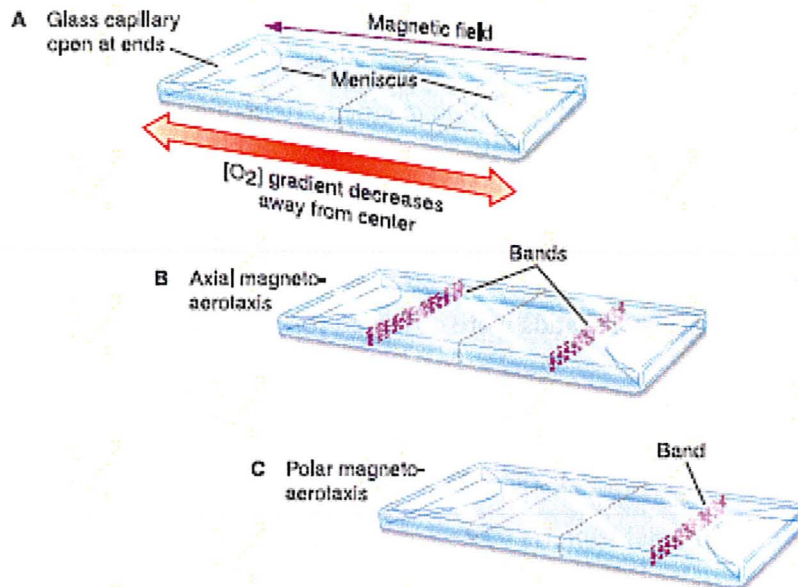


Figure 1.4 - Schematic depicting the formation of magneto-aerotactic bands in flat capillary tubes with both ends open placed in a magnetic field H . (a) Diffusion of air into both ends results in a double oxygen concentration gradient in the tube, with the minimum oxygen concentration at the centre. (b) Bacteria with the axial magneto-aerotactic mechanism form bands at both ends of the tube. (c) Northern hemisphere bacteria with the polar magneto-aerotactic mechanism form a band only at end of the tube for which the B is antiparallel to the oxygen gradient (c). Southern hemisphere bacteria would form a band only at the other end of the tube. (Frankel *et al.*, 1997; figure taken from Frankel & Bazylinski 2004 - Reproduced with permission from the *American Society for Microbiology (ASM News 70, 176.)*

greigite), in addition to the biological mediation of iron- and sulphate-reduction by microbes, could be contributors of the remanent magnetization in sediments and soils (Petersen *et al.*, 1986; Mann *et al.*, 1990; Kim *et al.*, 2005; Oldfield 2007); 2) environmental conditions, for example, redox and/or oxygen/sulphide concentrations could play a role in determining magnetosome composition.

Interestingly, Bazylinski *et al.* (1995) reported the presence of both magnetite and greigite within a single magnetotactic bacterium, (no species name as not yet isolated), found at or below the OATZ of a semianaerobic estuarine basin of Pettaquamscutt River Estuary, Narragansett, Rhode Island, in which both Fe_3O_4 and Fe_3S_4 magnetosomes were observed to be present within the same chain with distinct morphologies (Fe_3O_4 : arrowhead/tooth-shaped vs. Fe_3S_4 : rectangular; refer to Figure 1.5). Furthermore, it was found that the proportion of magnetite or greigite produced was linked directly to the external environmental conditions. Cells collected from both the OATZ and oxic zones were mainly magnetite-producers, while those from the anoxic and sulfidic zone were greigite producers. Similar to aerotactic responses, these observations suggest the possibility of chemo- or redox-tactic response mechanisms, that is, a response to the chemical or redox environment, and not only to the magnetic field and oxygen concentrations. Bazylinski *et al.* (1995) also confirmed that the sizes of the two types of minerals formed were within the respective permanent single-magnetic-domain-size ranges of magnetite and greigite (Butler & Banerjee, 1975;

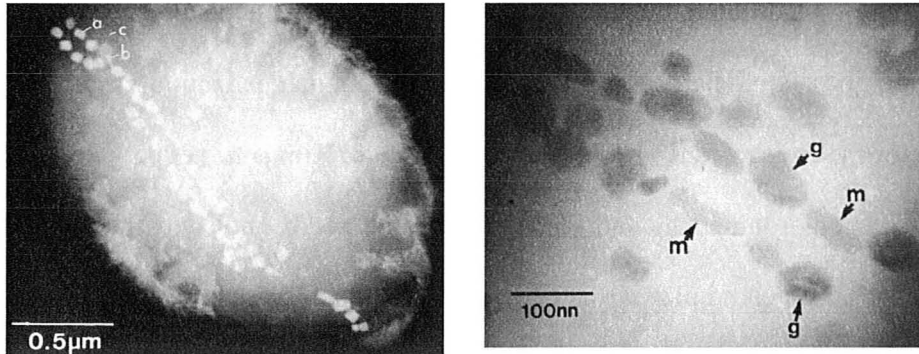


Figure 1.5 – Dark-field STEM (top) and brightfield scanning-transmission electron micrograph (bottom) of a rod-shaped magnetotactic bacterium showing tooth-shaped magnetite (Fe_3O_4) and pleomorphic greigite (Fe_3S_4) magnetosomes co-organized within the same chains. (Bazylinski *et al.*, 1995; Bazylinski & Frankel, 2003; Figures reproduced with permission from the *Mineralogical Society of America.*)

Hoffmann 1992).

1.1.3 Composition and structure of magnetosomes

Comparisons of iron oxide and iron sulphide magnetosomes of distinct crystal morphologies and sizes across various strains of magnetotactic bacteria have shown that magnetosome size distribution, composition and crystal habits are uniform and specific within a species or strain (Bazylinski *et al.*, 1994; Devouard *et al.*, 1998). Based on 2-D projections from electron microscopy, the main crystal morphologies (Figure 1.6) in magnetotactic bacteria are: cuboidal (Balkwill *et al.*, 1980; Blakemore 1982; Bazylinski *et al.*, 1994; Mann *et al.*, 1984), elongated prismatic (Moench & Konetzka, 1978; Towe & Moench, 1981; Blakemore 1982; Meldrum *et al.*, 1993a, 1993b; Bazylinski *et al.*, 1994) and

tooth-, bullet- or arrowhead-shaped (Mann *et al.*, 1987a, 1987b.; Thornhill *et al.*, 1994).

A general trend that has been observed in the biogenic mineral crystal structures are that most of the crystal morphologies have shown to consist of elongated projections, resulting in anisotropic crystal habits, of which the tooth-, bullet- or arrowhead-shape is the most anisotropic. It is thought that this anisotropy arises from either anisotropic interactions or ion flux through the

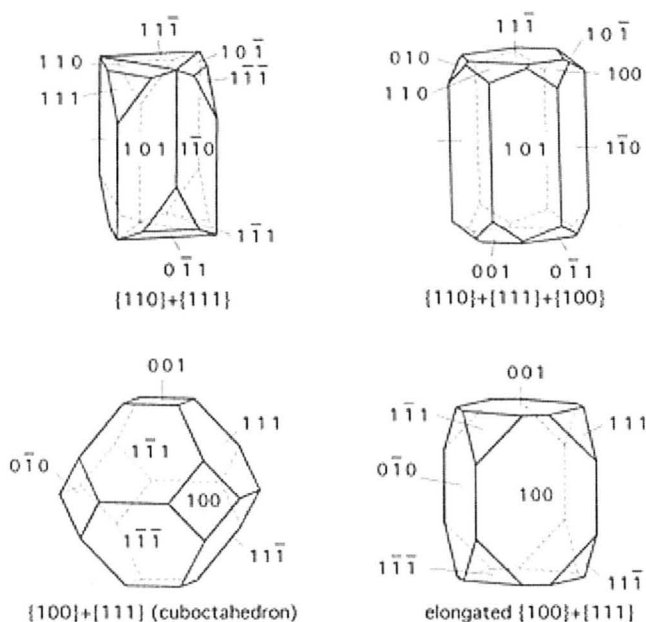


Figure 1.6 – Examples of some of the magnetosome crystal habits found in magnetotactic bacteria. Cuboctahedra (lower left) are found in both magnetite and iron sulfide magnetosomes. Two elongated habits (upper right and upper left) are found in magnetite magnetosomes. The lower right elongated habit is found in iron sulfide magnetosomes. (Figure adapted from Devouard *et al.*, 1998; Reproduced with permission from the *Mineralogical Society of America.*)

membrane surrounding the crystal during growth (Mann & Frankel, 1989). Since anisotropic crystals are rarely observed except in recent and ancient sediments, as well as in the Martian meteorite ALH84001 (McKay *et al.*, 1996), they have been considered as magnetofossils (Chang & Kirschvink, 1989). In other words, the unusual crystals are evidence that magnetotactic bacteria have previously existed in aquatic environments and sediments (Chang & Kirschvink, 1989; Stolz *et al.*, 1986, 1990), and even suggest the possibility that life had occurred on ancient Mars (McKay *et al.*, 1996; Thomas-Keprta *et al.*, 2000, 2001, 2002). Recently it has been shown that elongated magnetite crystals can be synthesized abiotically (Golden *et al.*, 2001).

1.1.4 Biomineralization of magnetosomes

The specificity of crystal morphologies, sizes and composition within a species is strong evidence that the process of magnetosome formation is under strict genetic control in a process referred to as “biologically controlled mineralization”, or “biomineralization” (Lowenstam 1981). After Mössbauer spectroscopy established that magnetosome chain(s) are fixed within the cell (Ofer *et al.*, 1984), further TEM studies showed that magnetosomes are surrounded by a lipid bilayer 3-4 nm thick, that contains components similar to those found in the cytoplasmic membrane, as well as some soluble and

transmembrane proteins specific only to the magnetosome membrane (Gorby *et al.*, 1988; Grunberg *et al.*, 2001).

In 2006, using electron cryotomography, Komeili *et al.* found that “magnetosomes are invaginations of the cell membrane flanked by a network of cytoskeletal filaments”, which enable the magnetosomes to be anchored to the cell membrane while being organized in a chain parallel to the long axis of the cell. Bazylinski and Frankel (2003) have proposed a series of discrete steps involved in the complex process of magnetosome formation (refer to Figure 1.7): (i) the invagination of the cell membrane to form magnetosome vesicles; (ii) iron uptake by the cell; (iii) iron transport into the magnetosome vesicle; (iv) controlled magnetite or greigite biomineralization within the magnetosome vesicle; and (v) the organization of the vesicles in chains. Uptake of iron by the cell has been shown to occur in both the ferric and ferrous iron forms, depending on the strain studied (Schüler & Baeuerlein, 1996; Faivre *et al.*, 2007).

In the case of *M. magnetotacticum*, Frankel *et al.* (1983) proposed that the iron transported into the magnetosome membrane vesicle forms a hydrous Fe (III) oxide (ferrihydrite: $\text{Fe}_2\text{O}_3 \cdot n\text{H}_2\text{O}$), which, upon the reduction of one-third of Fe(III) ions and pH adjustment, nucleates Fe_3O_4 within the vesicle. Alternatively, it has been suggested that this nucleation step could involve the adsorption of sequenced and many of the proteins and the roles they code for have been identified. However, much still remains to be understood about the

biomineralization of magnetosomes and the uptake and metabolism of iron in magnetotactic bacteria.

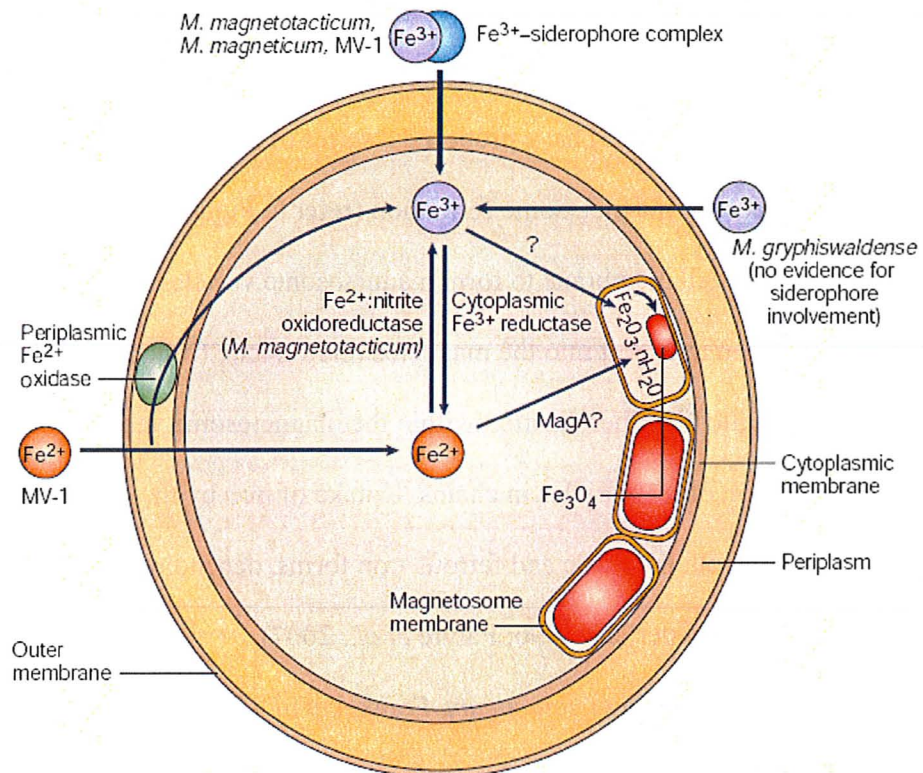


Figure 1.7 - Schematic of possible reactions leading to magnetite biomineralization in known, cultured species of magnetotactic bacteria. (Bazylinski & Frankel, 2004; Figure reproduced with permission from the Nature Publishing Group.)

1.1.5 Techniques applied to the study of magnetic properties of magnetosomes

A variety of techniques have been applied to magnetosomes for the determination of their magnetic properties. However, of particular interest and relevance to this thesis are those techniques which have previously investigated intact, yet unfixed, magnetotactic cells. These techniques include light scattering (Rosenblatt *et al.*, 1982a), magnetically-induced birefringence (Rosenblatt *et al.*, 1982b), pulsed magnetic-field remanence in a bacteriodrome (Hanzlik *et al.*, 2002) and low-temperature superconducting quantum interfering device (SQUID) magnetometry (Moskowitz *et al.*, 1993), in which living or dead cells were investigated in wet environments.

On the other hand, techniques that measured magnetic properties of dry (air-dried or freeze-dried) unfixed intact cells include magnetic force microscopy (MFM) (Dahlberg *et al.*, 1995), ferromagnetic resonance (Fischer *et al.*, 2008), off-axis electron holography (EH) in the transmission electron microscope (TEM) using Lorentz lens (Dunin-Borkowski *et al.*, 1998; McCartney *et al.*, 2001; Simpson *et al.*, 2005) and x-ray magnetic circular dichroism (XMCD) (Coker *et al.*, 2007).

1.2 Magnetite: Crystal, electronic and magnetic structures

Magnetosomes are intracellular ferrimagnetic nanocrystals that are biomineralized by magnetotactic bacteria (MTB) and are composed of either Fe_3O_4 (magnetite) or Fe_3S_4 (greigite). Since the strains of MTB studied in this project produced only Fe_3O_4 magnetosomes, this section will focus solely on the description of the crystal, electronic and magnetic structures of magnetite.

Magnetite (Fe_3O_4) is a member of the spinel group, a class of ferrimagnetic minerals that have the standard formula, $X^{2+}Y_2^{3+}O_4^{2-}$. Ferrimagnetism is a type of magnetic ordering in which the magnetic moments on different sub-lattices are opposed yet have unequal magnitudes, resulting in a net magnetic moment. Typically, X and Y represent two different metal ions that occupy specific sites in the crystal structure. Needless to say, magnetite, Fe_3O_4 , is one exception to this case.

The spinel group adopts a cubic (or isometric) crystal system, in which the unit cell consists of oxide anions arranged in a close-packed face-centered cubic array (Figure 1.8), while transition metal ions occupy some or all of the tetrahedral (A) and octahedral (B) sites in the lattice (Hurlbut & Klein, 1985). The preference of a metal ion to adopt a certain coordination geometry or occupy a certain sub-lattice (A or B) in the spinel structure may be predicted from crystal field theory, as it relates the d electron configuration of the metal ion and its crystal field stabilization energy (CFSE) to the symmetry of the surrounding

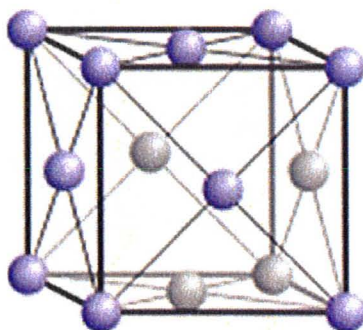


Figure 1.8 – The crystal system of spinels is the Face Centered Cubic (FCC) unit cell, in which there is one oxide anion at each corner and in each face of the cube. This close-packed array provides the maximum packing efficiency for spheres of equal radius. (Courtesy of E. Generalic, from <http://www.periodni.com/en/ar.html>)

ligands (Burns 1993), which is O^{2-} in the case of magnetite. Therefore, different cation distributions may be found in spinel structures, resulting in either the normal spinel structure, $(M^{2+})^A(M^{3+} M^{3+})^B O_4$, or the less common inverse spinel structure, $(M^{3+})^A(M^{2+} M^{3+})^B O_4$. Magnetite has an inverse spinel structure, $(Fe^{3+})^A(Fe^{2+} Fe^{3+})^B O_4$, which is thought to be due to the tendency of the Fe^{3+} ions to form hybrid sp^3 bonds, leading to a preferred occupation in the smaller tetrahedral (*A*) site (Goodenough and Loeb, 1955) and thereby, displacing the Fe^{2+} and the remainder of the Fe^{3+} ions to the octahedral (*B*) sites (Figure 1.9).

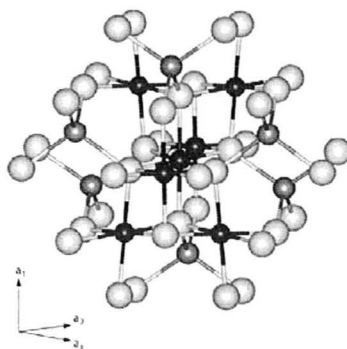


Figure 1.9 - The structure of a ferrite spinel showing the octahedral sites (small black spheres), tetrahedral sites (small grey spheres) and oxygen anions (large light grey spheres) after Patrick *et al.* (2002); Reprinted with permission from Schweizerbart (<http://www.schweizerbart.de>).

1.3 X-ray magnetic circular dichroism (XMCD)

1.3.1 History of X-ray Magnetic Circular Dichroism

The term “dichroism” refers to differential photon absorption based on a material’s orientation with respect to light polarization. In particular, x-ray magnetic dichroism refers specifically to the application of x-rays to investigate the differential absorption of polarized light (linear or circular) due to anisotropies in the magnetic properties of the material. In 1975, Erskine and Stern made the first predictions for an x-ray magnetic circular dichroism experiment from the calculation of the $M_{2,3}$ absorption spectrum of ferromagnetic nickel. This was soon followed by the work of Thole *et al.* (1985), who developed a theoretical model to predict and quantify the x-ray magnetic linear dichroism effect at the $3d$

absorption edges of rare-earth materials based on atomic multiplet calculations. These developments revealed the possibility of using x-rays for the determination of magnetic structure of magnetically ordered materials. Such pioneering work also suggested that magnetic structures could be studied using circular and linear polarized x-rays, which respectively give the average value of the local magnetic moment, $\langle M \rangle$, and square of the magnetic moment, $\langle M^2 \rangle$.

Soon after in 1986, the x-ray magnetic linear dichroic effect was proven experimentally on terbium iron garnet by van der Laan and coworkers (van der Laan *et al.*, 1986). Along with the development of high brilliance x-ray synchrotron sources with well-defined polarizations (linear or circular), x-ray magnetic dichroism has since become widely used to determine local magnetic properties of atoms in transition and rare-earth metal systems.

One type of x-ray magnetic dichroism is x-ray magnetic circular dichroism (XMCD), which was first performed by Schütz *et al.* in 1987 at the *K* absorption edge of iron using hard x-rays. As the name suggests, XMCD is a core-level absorption technique based on the differential absorption of left and right circularly polarized light. Strong XMCD effects are exhibited in the soft X-ray range, contributing to more than 20% of the spin-averaged absorption in some cases such as at the $L_{2,3}$ edges of Fe, Co and Ni metals (Sette *et al.*, 1990, Eimüller *et al.*, 2001). Since the soft x-ray signal is much stronger than that at *K* edges (where it is <1%), soft x-ray XMCD experiments with synchrotron radiation

dominate the use of x-rays to probe magnetism. The soft x-ray region allows probing of $L_{2,3}$ (core $2p$ to valence $3d$) excitations in ferromagnetic transition metals and $M_{4,5}$ (core $3d$ to valence $4f$) excitations in rare-earth magnetic materials.

Over the years, XMCD has become popular as it is element-, symmetry- and site-selective, providing “information on the polarization of the electronic states at the Fermi level and on local magnetic moments separated into spin and orbital contributions” (Schütz *et al.*, 1997). Using sum rules developed by Thole *et al.* (1992), Carra *et al.* (1993) and Altarelli (1993), XMCD can be used to determine the individual spin and orbital contributions to the magnetic moment. However, since sum rules were not applied in this project, they will not be discussed further.

1.3.2 XMCD at $L_{2,3}$ edges

The application of XMCD is particularly advantageous to studies conducted at metal $2p$ edges, as is the case with this project. Some of the more important advantages are: (1) multiplet structures are sharp, due to the core-hole lifetime broadening being only 100-300 meV, (2) L_3 and L_2 peaks are well separated, and (3) the dipole transition is from the $2p$ state to the $3d$ shell, which contains the magnetic moment (van der Laan and Thole, 1991). Methods to calculate $L_{2,3}$ absorption spectra for different x-ray polarizations have been

developed by van der Laan and Thole (1991) and de Groot's software program, CTM4XAS, from which computed XMCD spectra can be derived from the difference between spectra calculated for each polarization.

Briefly, the differential absorption of circularly polarized light in XMCD arises from the imbalance of spin-up and spin-down electrons in ferro- and ferri-magnetic materials. Spin selectivity in the x-ray absorption process leads to x-ray absorption spectra showing different peak intensities for different polarizations. By convention, the XMCD spectrum is produced by taking the difference of the absorption spectra measured with the magnetization anti-parallel and parallel to the x-ray beam, respectively (Brice *et al.*, 2005). When the magnetization is fixed, as is the case with the magnetosomes, changing the helicity (ie. circular polarization) of the beam is equivalent to reversing the magnetic field, thereby allowing for measurement of dichroic spectra. The mechanism of XMCD is explained in detail in section 2.3.2. Figure 1.10 shows an example of a Fe $L_{2,3}$ absorption spectra of Fe, along with the resulting XMCD difference spectrum at the bottom. It is important to note that the L_3 and L_2 XMCD peak intensities are inverted relative to each other due to the opposite spin-orbit coupling at the L_3 ($2p_{3/2}$) and L_2 ($2p_{1/2}$) levels (see section 2.3.2).

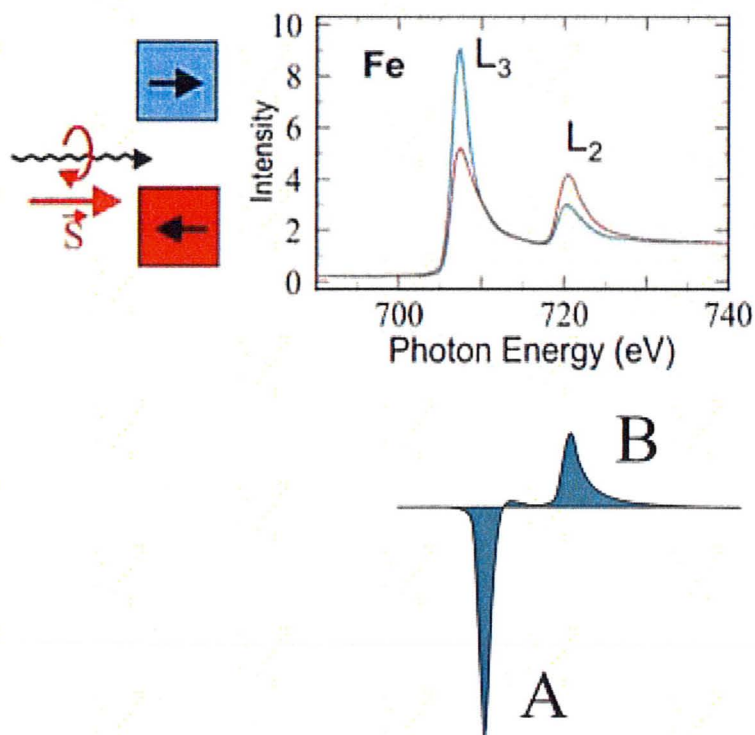


Figure 1.10 – Illustration of the XMCD effect in Fe; Top: Fe $L_{2,3}$ XAS of Fe measured with the magnetic moment aligned parallel and anti-parallel to the helicity of the circularly polarized x-rays; Bottom: Resulting XMCD difference spectrum. (Courtesy of J. Stohr, <http://www-ssrl.slac.stanford.edu/stohr/xmcd.htm>)

1.3.3 Fe 2p $L_{2,3}$ XMCD of magnetite

In the case of magnetite, Fe_3O_4 , the XMCD spectrum consists of three peaks at the L_3 edge, as shown in Figure 1.11. The detailed structure is related to the occupancy of Fe ions in three distinct sites: $d^6 \text{O}_h$ (octahedral Fe^{2+} site), $d^5 \text{T}_d$ (tetrahedral Fe^{3+} site) and $d^5 \text{O}_h$ (octahedral Fe^{3+} site) (Patrick *et al.*, 2002). The negative-positive-negative sense of these contributions is the result of the

antiferromagnetic coupling between the spins on the O_h and T_d sites such that tetrahedral sites are occupied by spin-down Fe^{3+} ions, and the octahedral sites are occupied by spin-up Fe^{3+} and Fe^{2+} ions (Lefever 1980; Kuiper *et al.*, 1997). The spin arrangement may be denoted as $(Fe^{3+}\downarrow)[Fe^{2+}\uparrow Fe^{3+}\uparrow]O_4$, where round and square brackets represent tetrahedral and octahedral sites, respectively (Cornell and Schwertmann, 2003).

Since the Fe^{3+} spins on the tetrahedral and octahedral sites are antiparallel, their magnetic moments cancel each other, leaving behind net ferrimagnetism from the Fe^{2+} on the O_h sites. The site occupancies or relative amounts of Fe present in the three sites for a given magnetite sample can be obtained from the relative intensities of their XMCD components. Comparisons of the experimental XMCD spectrum with that calculated using ligand field atomic multiplet theory have shown that the proportion of magnetic contributions from the Fe^{2+} (O_h): Fe^{3+} (T_d): Fe^{3+} (O_h) in fully magnetically saturated (endmember) magnetite is nearly stoichiometric, 1:1:1 (Carvallo *et al.*, 2008; Morrall *et al.*, 2003).

In the case of non-stoichiometric magnetite, in which vacant cation sites are present in the structure due to either additional oxidation or under-oxidation of Fe^{2+} to Fe^{3+} , deviations in the site occupancies from those of stoichiometric magnetite can be identified in the relative XMCD peak intensities. For the oxidation of Fe (II) to Fe (III) in the octahedral sites, a structure having the formula, $(Fe^{3+})[Fe^{2+}_{1-3\delta}Fe^{3+}_{1+2\delta}\Delta_{\delta}]O_4^{2-} = Fe_{3-\delta}O_4$ would result, in which δ

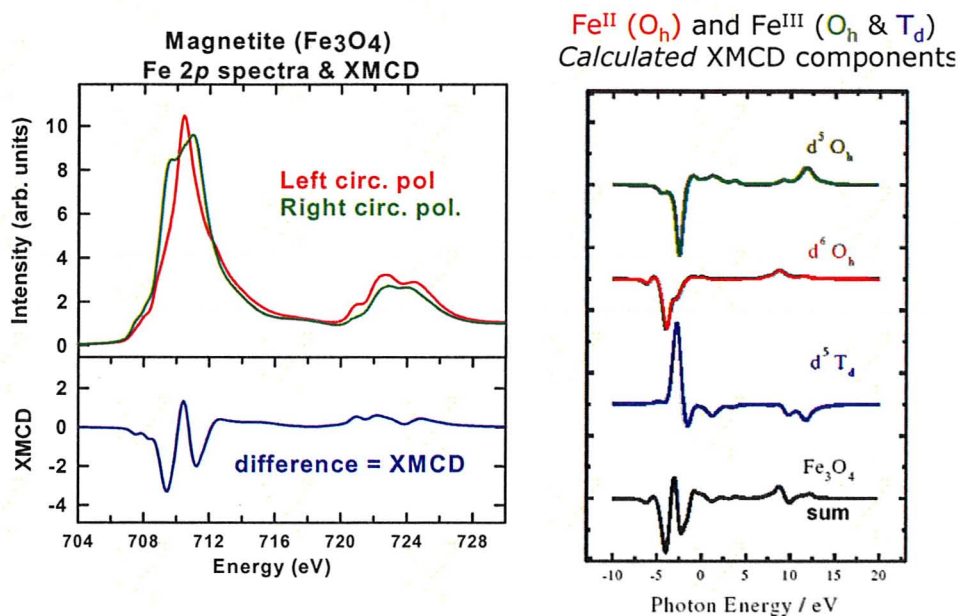


Figure 1.11 – Left: $L_{2,3}$ XAS of magnetite (Fe_3O_4) recorded at left and right circular polarizations of light (diagram constructed with data from: Goering *et al.*, 2007); Right: Calculated Fe components of the XMCD spectrum of magnetite. (Patrick *et al.*, 2002) (Figure modified with permission from Schweizerbart (<http://www.schweizerbart.de>)).

represents the deviation from stoichiometry due to cation vacancies (Pearce *et al.*, 2006). Therefore, accurate measurements of XMCD of biogenic magnetite, such as the magnetosomes studied in this project, may be used to deduce information about site occupancies and net magnetic properties, which in turn may provide insight into biomineralization mechanisms and biochemical control of inorganic crystallization.

1.3.3.1 XMCD of biogenic magnetite

Within the last decade, XMCD has become a more widely used synchrotron-based technique for the probing of magnetic structure and character of magnetic materials. It has been applied to the study of many different magnetic materials, including magnetite (Goering *et al.*, 2006, 2007), GdFe and PtCo layered systems (Fischer *et al.*, 1999), Co monolayers sandwiched between Au (Stöhr, 1999) and data storage devices (van der Laan & Welbourne, 1996). Most recently, XMCD has been used in several magnetosome studies. These include: the study of greigite magnetosomes (Letard *et al.*, 2005); comparison studies involving bulk samples of biogenic, abiogenic and synthetic nano-magnetite to investigate the cation site occupancy (Coker *et al.*, 2007); the monitoring of the *in-vivo* formation of magnetosomes in *Magnetospirillum gryphiswaldense*, strain MSR-1 (Staniland *et al.*, 2007); and the investigation of *in-vivo* doping of cobalt in magnetosomes of three strains of *Magnetospirillum* to increase magnetic hardness and coercivity for potential use in nanotechnological applications (Staniland *et al.*, 2008).

To date, there are only a total of eight studies reporting on the application of XMCD to studies of biogenic intracellular and extracellular magnetite (Table 1.2). Evidently, XMCD as it pertains to the study of MTB and magnetosomes is relatively fresh and unexplored. It is important to note that each study listed in Table 1.2 involved the measurement of the XMCD signal from an *ensemble* of

Table 1.2 – Summary of literature XMCD studies on biogenic magnetite

Nature of biogenic magnetite studied	Comments	Author and Year
Extracellular magnetite resulting from respiration of Fe(III) oxyhydroxides by <i>Geobacter sulfurreducens</i>	A study of the changes in partitioning of arsenic-sorbed ferrihydrite during bacterial reduction to magnetite	Coker <i>et al.</i> , 2006
Extracellular magnetite produced by <i>Geobacter sulfurreducens</i> and <i>Geothrix fermentans</i> ; Purified/isolated magnetosomes from MSR-1 ²	Determination and comparison of cation site occupancies in extracellular, intracellular and chemical magnetite	Coker <i>et al.</i> , 2007
Purified/isolated magnetosomes from MSR-1	A study of the real-time formation of magnetosomes in a magnetotactic bacterium	Staniland <i>et al.</i> , 2007
Extracellular magnetite produced by <i>Shewanella putrefaciens</i>	Comparison of compositions between biogenic and abiogenic magnetite using XMCD	Carvallo <i>et al.</i> , 2008
Extracellular magnetite produced by <i>Geobacter sulfurreducens</i> and <i>Shewanella oneidensis</i>	Determination of site occupancies in Co-, Ni- and Mn-substituted biogenic magnetite	Coker <i>et al.</i> , 2008
Purified/isolated magnetosomes from MSR-1, MS-1 and AMB-1	A study of cobalt content and magnetization in Co-doped magnetosomes	Staniland <i>et al.</i> , 2008
Extracellular magnetite produced by <i>Geobacter sulfurreducens</i>	Determination of crystallographic structure, site occupancies and valence states of biogenic magnetite and cobalt ferrite nanoparticles	Coker <i>et al.</i> , 2009
Extracellular magnetite produced by <i>Geobacter sulfurreducens</i>	A study of the remediation of Cr(VI) by biogenic magnetite nanoparticles	Telling <i>et al.</i> , 2009

² AMB-1: *Magnetospirillum magneticum* (bacterial strain)

MS-1: *Magnetospirillum magnetotacticum* (bacterial strain)

MSR-1: *Magnetospirillum gryphiswaldense* (bacterial strain)

intracellular (magnetosomes) or extracellular magnetite isolated from many cells. In addition, each study used total electron yield (TEY) detection, which only probes the outer few nanometers (< 5 nm) of the magnetic material, a region which is known to be subject to air oxidation.

1.4 Why study MTB and magnetosomes?

The tight constraints imposed by genetics on the size and shape of magnetosomes have allowed the discrimination of biogenic intracellular magnetite (magnetosomes) from biogenic extracellular magnetite and geological magnetite, using high-resolution electron microscopy (EM) (Arato *et al.*, 2005; Glasauer *et al.*, 2003; Taylor & Barry, 2004; Thomas-Keprta *et al.*, 2000), iron and oxygen isotopic studies (Mandernack *et al.* 1999), and crystal size distribution analyses (Faivre & Zuddas, 2006). Magnetosomes are attracting much attention from various disciplines since they have narrow size and shape distribution, high quality magnetic properties, and can be bioengineered or functionalized.

“The highly organized structures often exhibit excellent physical and/or chemical properties that outperform artificial materials, and, in comparison with the usual synthetic methods, the intricate architectures of these biominerals can be formed under conditions that are incredibly mild.” (Arakaki *et al.*, 2008)

Magnetotactic bacteria and magnetosomes are being considered as candidate materials for a broad range of environmental, technological,

biotechnological and medical applications, as they provide an alternative to the use of artificial magnetic nano-particles synthesized by advanced methods. Recent applications include the use of magnetotactic bacteria in the recovery of radionuclides and removal of Au(III) and from wastewater (Bahaj *et al.*, 1998; Song *et al.*, 2008, respectively) and in the development of controlled, MRI-trackable propulsion and steering systems for medical nanorobots operating in the human microvasculature (Martel *et al.*, 2009). Other proposed uses include magnetosomes as potential materials in the advancement of nano-technological materials, such as magnetic recording media and magnetic fluids (ferrofluids) (Safarik & Safarikova, 2002), as well as in the development of biotechnological and diagnostic techniques, such as magnetic resonance imaging, magnetic separation, DNA-extraction, bioassays, drug delivery and hyperthermia (Pankhurst *et al.*, 2003; Matsunaga *et al.*, 2004). Magnetosomes to be used in biotechnological applications would require them to be functionalized, which could be achieved through genetic and/or chemical modifications (Lang *et al.*, 2007; Arakaki *et al.*, 2008).

Aside from using magnetosomes directly, the biomineralization process in MTBs may also assist in the development of novel magnetic materials. For example, magnetic Co_2B_{10} arrays have been synthesized by Cao *et al.* (2003) using a biomimetic strategy inspired by magnetotactic bacteria, while Prozorov *et al.* (2007) used specific MTB proteins in order to control crystal size and habit of

synthesized magnetite nanocrystals. Other work has shown the possibility of manipulating the biomineralization process via the introduction and doping of metals other than iron, such as cobalt (Staniland *et al.*, 2008), manganese (Keim *et al.*, 2009), and, zinc and nickel (Kundu *et al.*, 2009), into the growth medium of the magnetotactic bacterium. Together, these studies reveal the importance of studying magnetosomes, as well as understanding the biomineralization mechanisms of magnetotactic bacteria. The knowledge gained from MTB studies will enable the development of advanced magnetic nanomaterials tailored with specific, desired and innovative magnetic properties, depending on the intended application.

Last but not least, studies of magnetotactic bacteria and magnetosomes are driven by the common desire to attain a more fundamental understanding of the biomineralization process, to uncover possible phylogenetic and evolutionary links between organisms and the geomagnetic field, and to elucidate the origins of paleomagnetism and environmental magnetism.

1.5 Goals of thesis

The goals of this thesis study are:

- (1) To develop XMCD in a scanning transmission X-ray microscope (STXM) to make magnetic measurements at high spatial resolution (30 nm);
- (2) To apply that capability to studies of individual magnetosomes in magnetotactic bacteria.

The project was successful since XMCD was measured at high spatial resolution (30 nm) using soft x-ray scanning transmission X-ray microscopy (STXM); (2) STXM-XMCD was applied to *Magnetococcus sp.* (strain MC-1), a multi-cellular magnetotactic prokaryote (MMP), and a marine vibrio (strain MV-1) to probe the magnetic properties of the individual Fe₃O₄ magnetosomes. This work is the first XMCD measurement of non-isolated individual magnetite magnetosomes in intact bacterial cells at high spatial resolution (30 nm).

Chapter 2

METHODS

This section describes the physical principles of the experimental methods used in this study, which include STXM, NEXAFS and XMCD.

2.1 Synchrotron Radiation

Synchrotron radiation is light that covers the electromagnetic spectrum continuously from infrared to hard x-ray and which is generated through the acceleration of high-energy electrons in a ring from deflections by a magnetic field. The Canadian Light Source (CLS) and Advanced Light Source (ALS) are both third-generation synchrotron sources in which insertion devices are used. Insertion devices are magnetic structures, such as wigglers or undulators, which are installed along straight sections of the particle trajectory to enhance the flux and brightness of the light beam by causing wiggles (low frequency) or undulations (high frequency) in the motion of the accelerated electrons. For this reason, synchrotron radiation from third-generation synchrotron facilities is highly bright and intense, in addition to being highly polarized and fully tunable.

2.2 Scanning Transmission X-ray Microscopy (STXM)

Scanning Transmission X-ray Microscopy (STXM) is a synchrotron-based technique, which combines x-ray spectroscopy and microscopy, thereby allowing for high-spatial resolution, chemical-sensitive imaging and characterization of heterogeneous materials via the recording of images at one or more photon energies and spectra from small spots. STXM is widely used in the analyses of materials such as polymers and biological materials (Ade & Hitchcock, 2008). Compared to traditional spectroscopy and transmission electron microscopy

techniques, the main advantage of x-ray spectromicroscopy is that it allows for quantitative chemical mapping at a sub-micron spatial scale, which is achieved through Near-Edge X-ray Absorption Fine Structure (NEXAFS). At the same time, the degree of radiation damage by STXM is estimated to be two orders of magnitude lower, compared to that of analytical electron microscopy techniques based on core level electron energy loss spectroscopy (Rightor *et al.*, 1997; Wang *et al.*, 2009a, 2009b).

Currently, the state-of-the-art spatial resolution of STXM is 15 nm while the microscope used in this work routinely operates with 30-nm resolution. The STXM measurements reported in this thesis were made at the CLS and ALS, which are synchrotron facilities based in Saskatoon, SK and Berkeley, California, respectively. Figure 2.1 is a plan view of the CLS soft x-ray spectromicroscopy beamline, in which STXM is one of the endstations. The plan view shows that the synchrotron radiation generated by the elliptically polarizing undulator (EPU) passes through a series of focusing and dispersing optics, before reaching the STXM endstation.

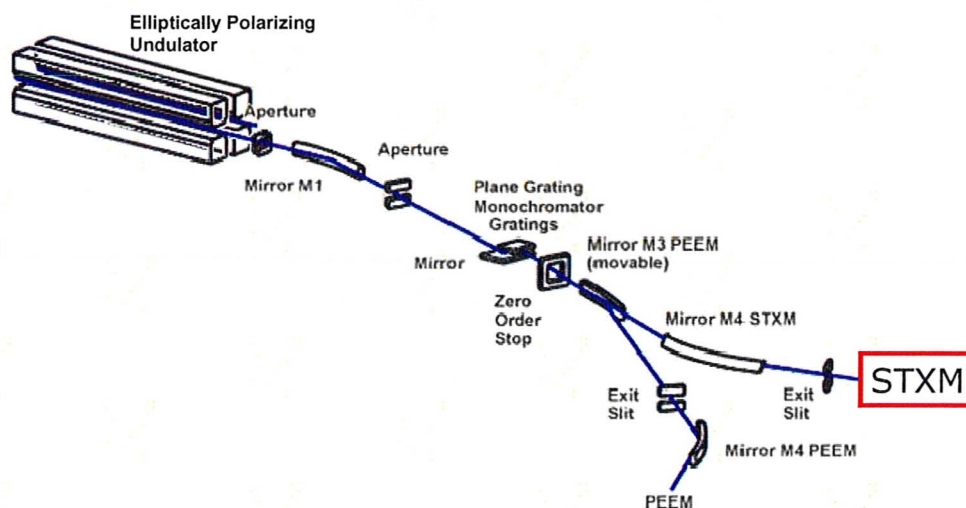


Figure 2.1 – Plan view of the CLS soft x-ray spectromicroscopy beamline, in which STXM is located.

2.2.1 Instrumentation, spatial and energy resolution of STXM

STXM operates by having a monochromatic soft x-ray beam focused to a small point by a Fresnel zone plate (Figure 2.2). Soft x-rays refer to x-rays in the range between 100 eV and 3 keV ($\lambda \sim 0.4 - 12 \text{ nm}$), which have the ability to penetrate a few millimeters of air. An order-sorting aperture (OSA), typically 60-90 μm in diameter, is then used to isolate the desired first order light, from the undesired zeroth order light, as seen in Figure 2.3. The sample intersects the light at the focal point and transmitted x-rays are detected by a phosphor that converts the X-rays to visible photons, which are then counted by a photomultiplier tube (PMT). To generate a transmission image, a thin sample ($\sim 100 \text{ nm}$ thickness) is

raster-scanned on the x- and y- axes and the transmitted signal intensity is acquired at each pixel.

The quality of the data collected by STXM is dependent on the spatial and energy resolution of STXM. The high spatial resolution (30 nm) of STXM is made possible due to the combination of various STXM components and their

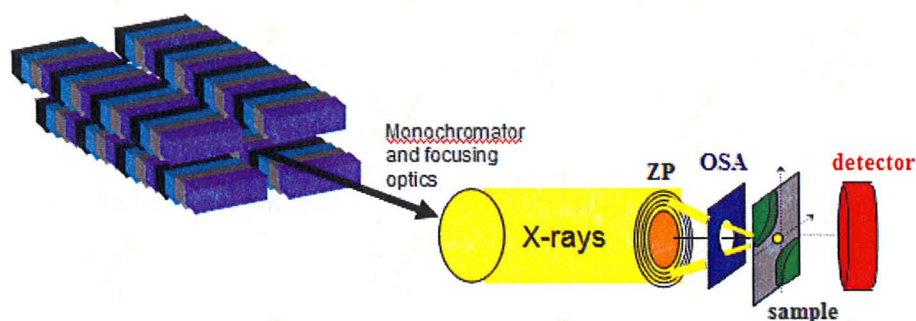


Figure 2.2 – Schematic of the operation of STXM.

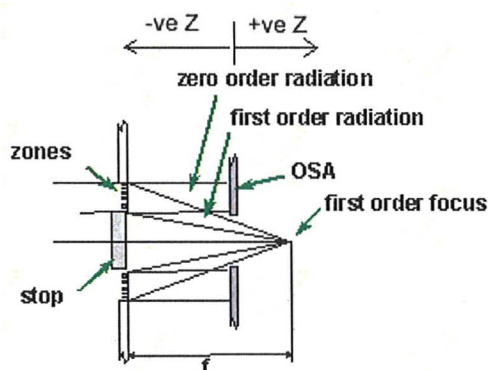


Figure 2.3 – Focusing scheme in STXM (Source: STXM 5.3.2 User Manual)

specific configuration within the instrument. Of all the STXM components involved, the properties of the Fresnel zone plate are most critical to achieving high spatial resolution.

The Fresnel zone plate (ZP), which is the focusing “lens” in STXM, is a circular diffraction grating with variable line-spacing. ZPs are highly delicate and expensive components manufactured using cutting-edge nano-lithography technology. They are composed of accurately positioned sub-micron concentric rings (“zones”) that alternate between opaque (Au) and transparent (silicon nitride). Light is focused by the zone plate based on the diffraction occurring around opaque zones, which are accurately positioned in a way that allows constructive interference of the light at the focal point. The relationship between the size of the outermost zone and the focal length (f) required at a certain photon wavelength (λ) [or photon energy (E), where E (eV) = 1239.852 / λ (nm)], is given by:

$$\text{(Eq. 2.1)} \quad f = D \cdot \delta_{rN} / \lambda$$

in which D and δ_{rN} refer to the diameter and the width of the outermost zone, respectively. The zone plate used in this study has a diameter and outermost zone width of 240 μm and 25 nm, respectively. This gives a focal length of approximately 1.5 mm at the C $1s$ edge (300 eV) and 3.4 mm at the Fe $2p$ edge

(710 eV). The outermost zone determines the diffraction-limited spatial resolution (Δr) according to the equation:

$$\text{(Eq. 2.2)} \quad \Delta r = 1.22 \cdot \delta_{rN}$$

Further explanations of the principles involved in the operation of Fresnel zone plates may be found in the CXRO Handbook of synchrotron radiation (Kirz & Attwood, 1986; Thompson *et al.*, 2001) and the textbook by Attwood (1999). It is important to note that STXM zone plates contain a central stop - an opaque region in the centre which serves, in combination with the OSA (Figure 2.1), to filter out unwanted diffraction orders of light (eg. zeroth order) that would otherwise lower the spatial resolution.

Aside from the zone plate, many other operational parameters and beamline settings need to be fully optimized in order to achieve the best possible resolution. These parameters include the OSA position, ZP focus, sample-OSA distance, sample focusing and the accuracy of the energy scale. For example, since the focal length (f) varies with photon energy (E), the distance between the sample and order-sorting aperture (OSA), also referred to as A_o , needs to be adjusted according to the following equation:

$$\text{(Eq. 2.3)} \quad f = A_1 E + A_o$$

in which A_1 is the experimentally determined change in focal length with photon energy. As the OSA-sample distances are on the order of hundreds of microns, working with such small distances requires movements and positioning of various STXM components to be carefully and precisely controlled (within ~ 500 nm accuracy in z and 10 nm accuracy in x -, y - directions) in order to maintain a stable and focused beam. To achieve this, STXM employs high precision stepping motor and piezo stages in conjunction with a laser interferometry feedback-control system, which continuously adjusts the sample position to maintain the desired point of the sample at the position of the focused X-ray spot (Kilcoyne *et al.*, 2003).

The energy resolution of STXM is determined by the monochromator and the sizes of entrance (if present) and exit slits. To select a particular energy, a spherical-grating monochromator (ALS 5.3.2. SGM) or entrance-slit-less plane-grating monochromator (CLS-SM and ALS 11.0.2 PGM) is used to disperse the soft x-ray regime. The energy band of the dispersed light that passes through the exit slit defines the energy resolution. Currently, the CLS offers an energy range of 130-2500 eV with 0.1 eV resolution and a flux of 10^8 photons per second (from 300-1800 eV) at the sample in STXM. The sample may be mounted in air or He, or in a fully hydrated environment with up to 2- to 3- μm thickness of water sandwiched between two 75-nm-thick X-ray-transparent silicon nitride windows

with areas of 0.5 mm² or 1 mm². In the case of this thesis, the samples were dry and mounted in He at 1/5 to 1/3 atmospheric pressure.

2.3 X-ray Absorption Spectroscopy (XAS)

Thanks to recent improvements in synchrotron sources, especially the development of high-brilliance third-generation synchrotron facilities, the last decade has witnessed rapid growth in core level spectroscopy and spectromicroscopy using X-ray techniques. Although there are different types of core level spectroscopy, this section will be limited to discussing X-ray absorption spectroscopy (XAS), which is the spectroscopy involved in this thesis.

X-ray absorption spectroscopy (XAS) measures the dependency of the absorption of x-rays on photon energy. XAS features are associated with excitation of core electrons to empty states (ie. conduction bands or unfilled molecular orbitals). As core-level processes are specific for each element, absorption features are element-specific and even site-specific so that specific transitions can be correlated with specific sites in a complex material like magnetite. XAS requires tunable X-rays which are best provided by a synchrotron source.

In X-ray studies, the absorption edges are labeled using two notations, either x-ray spectral (K, L, M, N, O and P) or quantum (principal quantum numbers, $n = 1, 2, 3, 4, 5$ and 6). Furthermore, orbital angular momentum (l) and

the influence of spin-orbit coupling on core-level states are taken into account by labeling the states with a core-level vacancy by the orbital angular momentum ($l = s; 2, 3 = p; 4, 5 = d$) and by total angular momentum, $J = l \pm s$, where l (with values from 0 to 3) and s ($1/2$ for spin-up and $-1/2$ for spin-down) are the orbital and spin angular momentum quantum numbers, respectively. This thesis involves the $2p \rightarrow 3d$ transitions of Fe in Fe_3O_4 to probe the magnetic properties which are contributed mostly by the $3d$ states. The Fe $2p$ XAS transitions will be referred throughout this thesis by either the orbital notation ($2p_{1/2}$ and $2p_{3/2}$) or the spectroscopic label (L_2 and L_3).

For a non-zero orbital angular momentum quantum number, spin-orbit coupling is present and gives rise to two peaks in the XAS spectra, which are separated by spin-orbit splitting. Spin-orbit coupling is a relativistic effect arising “from the interaction between the electronic spin and the magnetic field experienced by an electron as it orbits a positively charged nucleus” (Lovesey & Collins, 1996). Therefore, a single vacancy in an atomic core level of a given orbital angular momentum, l , results in two states with different total angular momentum, J . The splitting between the pairs of states in core holes is large because core electrons are tightly bound and orbiting fast, leading to a strong relativistic character which is the source of the spin-orbit coupling. The energy of each state is determined by the coupling between the electron spin angular momentum and the orbital angular momentum, such that parallel coupling, as in

the $J = 3/2$ state ($p_{3/2}$), is energetically less favourable and thus, less tightly bound than the $J = 1/2$ state ($p_{1/2}$), which has net antiparallel coupling.

Therefore, in the case of Fe $2p$ ($l = 1$) XAS spectra, two peaks corresponding to $J = 1/2$ and $3/2$ are observed, which are labeled L_2 and L_3 , respectively (refer back to top of Figure 1.10). The relative intensity of the two peaks is related to a number of factors – the degeneracy of the states, the magnitude of the exchange interaction and details of the multiplet splittings. The influence of spin-orbit coupling on the XMCD effect is further discussed below in section 2.3.2.

2.3.1 Near Edge X-ray Absorption Fine Structure (NEXAFS)

The chemical sensitivity of STXM is a result of the near-edge X-ray absorption fine structure (NEXAFS), which is an acronym referring to XAS close to an absorption edge (Stöhr 1992). For unsaturated and saturated molecular compounds, the spectroscopy involves transitions to the lowest unoccupied molecular orbitals (LUMO), the π^* and σ^* orbitals. For crystalline inorganic solids, which are the focus of this study, the features correspond to transitions to empty conduction band states highly modified by the core hole. Through the circular polarization dependence (XMCD), NEXAFS is sensitive to the magnetic properties and is therefore, a powerful technique to study magnetic materials.

Each inner-shell energy level of each element has an associated characteristic absorption edge, which is determined by the binding energy of the inner-shell. Thus, NEXAFS is sensitive to elemental content of the sample. Since the structure of the unfilled orbitals or conduction bands depends on the bonding and the geometric structure of the sample, the NEXAFS spectral details are characteristic for each site in a sample and provide information on the bonding environment of the element at each site. NEXAFS can be used not only for qualitative identification, but also quantitative analysis since the transition intensity is proportional to the amount of material contributing to the measured signal.

2.3.2 X-ray Magnetic Circular Dichroism (XMCD)

According to de Groot & Kotani (2008), “one of the most powerful applications of XAS to magnetic properties of materials is the circular polarization effect of XAS.” Briefly, the XAS intensity in ferro- and ferri-magnetic materials is dependent on the handedness or helicity (+/-, or, right/left) of the circularly polarized incident X-rays. The difference of the XAS spectra collected at both circular polarizations is called X-ray magnetic circular dichroism (XMCD).

XMCD is a probe of the imbalance in spin-polarized densities or populations of empty states above the Fermi energy. It is this anisotropy of the

population of “spin-up” and “spin-down” filled states which contributes to the d band spin moment in magnetic materials. The reason for the sensitivity of XMCD to spin is due to the presence of core-hole spin-orbit coupling.

Spin-orbit coupling allows XMCD to be capable of producing strong spin sensitivity because the photon helicity or angular momentum of photons of a given circular polarization (left ($-\hbar$) or right ($+\hbar$)) is transferred or ‘couples’ to the atomic orbital angular momentum in the same way that an electron’s spin and orbital angular momenta couple together to form spin-orbit split states. Due to the opposite nature of the spin-orbit coupling of the L_3 ($p_{3/2}$) and L_2 ($p_{1/2}$) states, the polarization of the photon spin needed to excite the L_3 and L_2 transitions is opposite, which is reflected in the opposite peak intensities of XMCD spectra (bottom of Figure 1.10). The absorption of circularly polarized photons in XMCD can be explained in terms of a two-stage process (Stöhr 1995; Lovesey & Collins, 1996). In the first stage, a circularly polarized photon is absorbed and excites a core-level electron of a certain spin (ie. up or down). Next, the excited electron populates an unoccupied spin-polarized valence state of the appropriate spin. Thus, the transition probability is proportional to the number of available final states that have the same spin state as that of the excited electron. In other words, due to the conservation of spin in x-ray absorption processes, $2p \uparrow$ electrons can only be excited into $3d \uparrow$ states, and $2p \downarrow$ electrons can only be excited into $3d \downarrow$ states.

In magnetic materials, the population of the empty states of the two spin-polarizations, spin-up and spin-down, differ. Thus, $2p \uparrow$ and $2p \downarrow$ electrons have different transition probabilities, thereby giving rise to differential absorption of the two circular polarizations of light (Figure 2.4). The transition probabilities to the spin-polarized empty states determine the x-ray absorption intensities at a given circular polarization, such that the intensities are directly proportional to the number of the empty d states of a given spin.

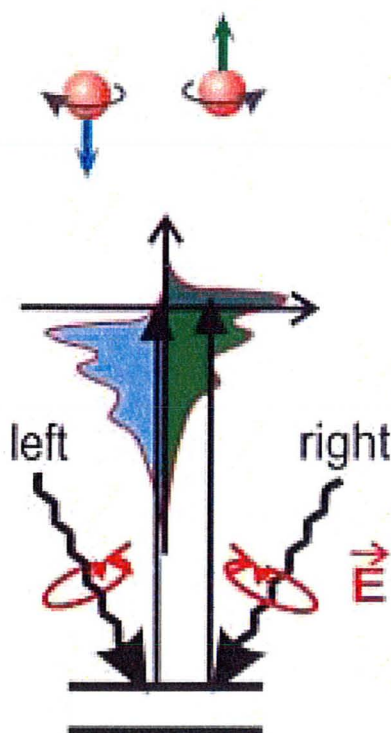


Figure 2.4 – Illustration of the x-ray magnetic circular dichroism process – the excitation of electrons to spin-polarized empty states via the absorption of circularly polarized photons. (Courtesy of J. Stöhr, <http://www-ssrl.slac.stanford.edu/stohr/xmcd.htm>)

2.3.1.1 Properties and production of circularly polarized X-rays

At the CLS SM (10ID-1) and ALS MES (11.0.2) beamlines, circularly polarized x-rays are produced with the help of elliptically polarizing undulators (EPU), consisting of two (ALS) or four (CLS) moveable magnetic quadrants, respectively. In the EPUs, four magnetic structures provide arrays of horizontal and vertical magnetic fields through which the synchrotron electron beam accelerates in a spiral motion. Observing the beam head-on, the electrons would appear to travel in circular orbits, thereby, emitting circularly polarized radiation.

In the 200-900 eV range, the CLS and ALS EPUs provide nearly 100% circularly polarized light (Kaznatcheev *et al.*, 2007) when the magnetic structures are appropriately positioned. The advantage of EPUs is that they allow for switching of polarizations so that samples with fixed magnetizations can be studied. An alternative to switching the helicity of the photon is to use fixed helicity and then reverse the magnetization of the sample with an applied magnetic field, most conveniently using an electromagnet. Since magnetite is a hard magnetic material, a very large magnetic field is required to re-orient its magnetization. Thus, switching of photon helicity is more practical. In addition, the focus of the work is to study the magnetism of MTBs without changing either the magnitude or orientation of their magnetization.

Circularly polarized light comprises two perpendicular electromagnetic plane waves of equal amplitude with a 90° phase shift and is characterized by a

rotating electric field vector. For example, circular polarized light with a clockwise rotation of the electric field along the propagation direction is referred to as right circular polarization, and vice versa (Figure 2.5). For each wavelength of circular polarized light that is propagated, the electric field vector makes one complete revolution.

In order for magnetic moments to be measured by circular polarized x-rays, selection rules for the transition require that the direction of the magnetic moment be parallel (or anti-parallel) to the direction of the circularly polarized X-ray beam. In other words, XMCD measurements may only be made on samples containing out-of-plane magnetic moments, when such samples are placed perpendicularly to the X-ray beam. Thus, the conventional STXM sample configuration with the sample normal to the beam is only sensitive to out-of-plane magnetization, which is less common than in-plane magnetization. Since the magnetization of magnetosome chains in MTBs are in-plane, a tilted sample mount is necessary to create a component of the magnetic moment of the sample that is parallel (or anti-parallel) to the circularly polarized X-ray beam (Figure 2.6). Various sample mounts can achieve the required sample orientations. In addition, methods of rotating samples inside STXM for the XMCD investigation of magnetosomes have been developed as part of this project and these are discussed in Chapter 3.

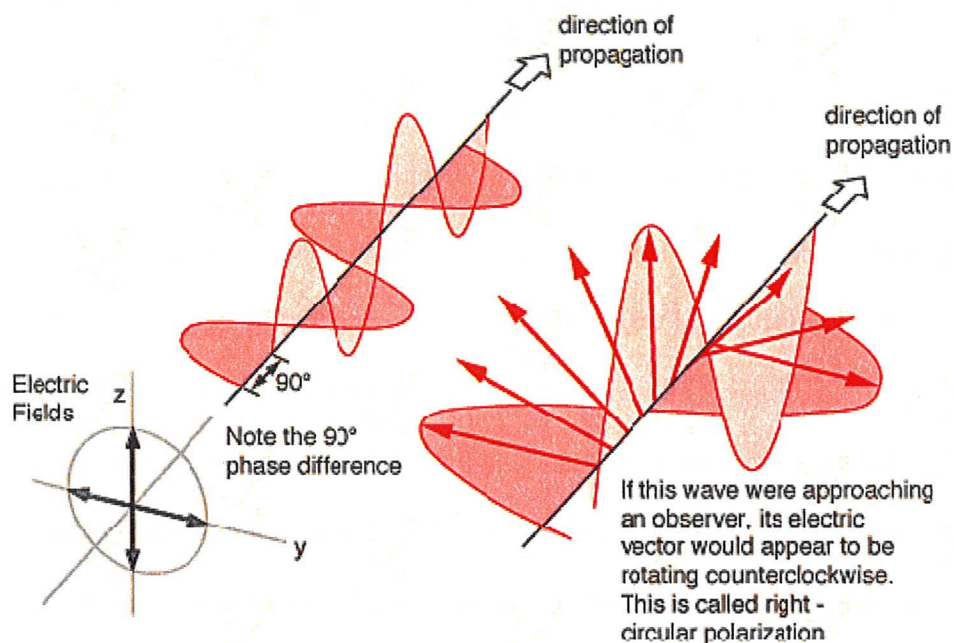


Figure 2.5 - Circularly polarized light comprises two perpendicular electromagnetic plane waves of equal amplitude with a 90° phase shift and is characterized by a rotating electric field vector. (Courtesy of R. Nave, <http://hyperphysics.phy-astr.gsu.edu/hbase/phyopt/polclas.html>)

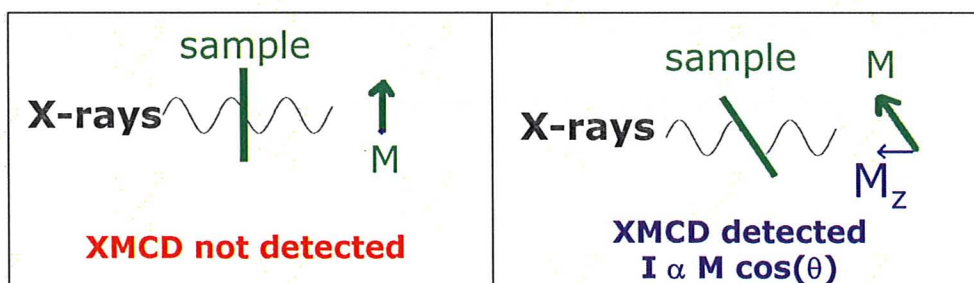


Figure 2.6 – Schematic illustrating the importance of in-plane magnetized samples to be tilted/rotated for the detection of XMCD.

2.3.1.2 XMCD of Co-Pt test sample to demonstrate CLS ability

In order to demonstrate the ability of CLS BL 10ID-1 to use X-ray magnetic circular dichroism (XMCD) for the investigation of magnetic structure at fine spatial scales, test measurements were made on a magnetic Pt(20)[Co(0.4)Pt(0.7)]₅₀Pt(2) multilayer sample supplied by Hitachi Global Storage Technologies (Fischer *et al.*, 1999). This sample consists of a labyrinth stripe domain pattern on a ~100 nm length scale where the two domains have opposite out-of-plane magnetic moments. High quality XMCD images of the domain structure were easily achieved using the CLS STXM with short (1 ms/pixel) dwell times (Lam *et al.*, 2008) and showed the expected XMCD spectra and spatial variation of magnetization changes (Figure 2.7). In addition, when high quality Co $L_{2,3}$ spectra (and images at the Co L_3 peak) were obtained using linear polarization, there was no evidence of the magnetic domain pattern (Lam *et al.*, 2008), indicating the EPU and optical system at the CLS spectromicroscopy beamline performs very well for XMCD measurements.

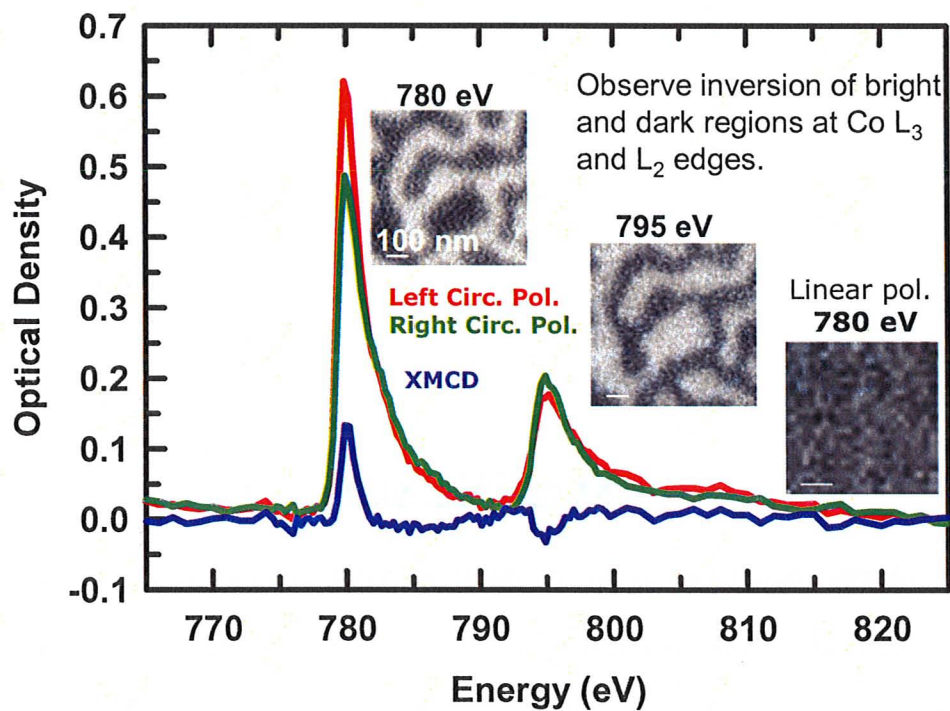


Figure 2.7– STXM images and XMCD spectra of a Co-Pt multilayer test sample at the Co $L_{2,3}$ edges. Note: There is no magnetic contrast in the image recorded with linear polarization.

Chapter 3

EXPERIMENTAL

This chapter describes sample preparation, data acquisition procedures by STXM-XMCD and data analysis. It concludes with a historical summary of the evolution of the experimental studies performed throughout this project.

3.1 Sample preparation

In the course of this thesis, the investigation of MTBs involved two separate attempts to culture MTBs. The first attempt involved a sample of strain MC-1 MTBs acquired from Dr. Arash Komeili (University of California, Berkeley). The required growth medium was prepared in a manner similar to the one described by Blakemore *et al.* (1979). Despite unsuccessful attempts to culture MC-1 at McMaster University, Martin Obst, working at the NWRI lab in Saskatoon with George Swerhone, was able to culture the MC-1 sample. Several samples from these cultures were examined in the course of developing the STXM-XMCD method. However, the best samples, and the ones on which the final results were based, were those prepared on TEM grids at UNLV by Professors Ulysses Lins and Dennis Bazylnski (see below).

The second attempt involved the isolation and culturing of MTBs from several water-sediment samples collected from Princess Point/Hamilton Harbour. Despite having followed MTB collection and enrichment procedures mentioned in the work of Adamkiewicz *et al.* (1991), Blakemore *et al.* (1979) and Moench & Konetzka (1978), no MTBs were found in any of the collected water samples. Experimental details regarding the sampling and culturing of MTBs are documented in Appendices 1 and 2.

Since I was not successful in my attempts to culture and enrich magnetotactic bacteria, cultured MTB samples were additionally obtained from

collaborators, Professors Ulysses Lins and Dennis Bazylinski. The acquired MTBs consisted of the MC-1 (coccoid - spherical), MMP (multicellular magnetotactic prokaryote) and MV-1 (vibroid - curved) cells. The samples for STXM were prepared at UNLV by Dr. Lins using the following protocol: Three mL of a liquid culture of the MTB was centrifuged at 4 °C at 10,000 g and washed twice in artificial seawater (NaCl - 16.43 g/L, MgCl₂ - 3.49 g/L, Na₂SO₄ - 2.74 g/L, CaCl₂•2H₂O - 0.386 g/L, KCl - 0.465 g/L). A drop (5–10 µL) of the washed cells was deposited onto 200-mesh glow-discharged copper grids coated with a thin layer of carbon (~3 nm, TedPella Inc. Catalog # 01822, www.tedpella.com). The drop was left to stand for 1 min prior to removing excess liquid by placing the grid over a piece of filter paper, followed by air-drying the sample.

Samples for STXM were deposited on either silicon nitride (Si₃N₄) windows or formvar-coated transmission electron microscopy (TEM) grids. In the case of MTB samples, STXM sample preparation requires a pre-concentration of MTBs and de-salting of the culture medium prior to the sample deposition step. MC-1 was successfully cultured at the National Water Research Institute (NWRI) in Saskatoon by collaborators, John Lawrence and George Swerhone. To pre-concentrate and de-salt a MC-1 sample, 1mL of bacterial culture was centrifuged at 6000g for 4-5 minutes. Half to 2/3 of the supernatant was removed, followed by re-suspension in deionized water added to make up the volume to 1mL. This

process was repeated five times. Placing a magnet at the bottom of the centrifuge tube, 2 μl of the desalted MTB culture was taken from the bottom of the tube, deposited on a silicon nitride (Si_3N_4) window and then let to air-dry.

Initial STXM measurements on MC-1 samples did not show the expected and spherical morphology characteristic of MC-1 cells, but rather smears and open circles (Figure 3.1). This was because cell lysis had occurred, probably due to osmotic shock – the rapid movement of water into the cell, in response to a sudden change in the concentration of salts around the cell, thereby, leading to rupture of the cell membrane. In order to avoid cell lysis, serial dilutions alternating with centrifugation steps were undertaken.

The total salt concentration of the growth medium was approximately 7.5mM. A 5-step serial dilution procedure was followed, which involved the use of graded salt solutions made with a phosphate-buffered saline solution (PBS). Five PBS solutions were made such that consecutive solutions were diluted by a factor of 2 to 3. In this case, the final PBS solution resulted in a concentration of 0.31mM. Into a 1mL centrifuge tube, 0.2 mL of MC-1 sample and 0.1 mL of 7.5mM PBS solution was added. The tube was centrifuged at 6000 rpm for 5 minutes. The MTB cells at the bottom of the tube (~ 0.1 mL) were transferred to a new centrifuge tube and the second graded PBS solution (2.5 mM) was added to make up the volume to 0.3 mL. This procedure was repeated with the addition of consecutive serially-diluted PBS solutions for 5 times. Following the last

centrifugation, the pellet observed at the bottom of the tube was transferred and deposited on a TEM grid. Multiple trials of this serial-dilution-centrifugation method were carried out with variations in the centrifugation rate (5000 vs. 10,000 rpm), centrifugation time (5 vs. 10 mins.) and sampling area (supernatant vs. bottom of centrifuge tube). The reason for also considering the supernatant is due to the possibility that cells may become buoyant in the event that microbubbles from the solution adhere to the cells causing them to float in the supernatant layer. The resulting TEM grids were all inspected for the presence of intact MC-1 cells by visible light microscopy (VLM), in which one particular trial was successful.

Another method that was used to pre-concentrate the MC-1 without causing osmotic shock involved depositing a concentrated suspension of MC-1 cells onto a TEM grid and dipping the grid sequentially in droplets of serially diluted PBS solutions to wash away excess salts. The final method also involved deposition of a concentrated suspension of MC-1 cells. However, in this method, the growth medium solution was removed by using the edges of a piece of filter paper to suck away the excess salt solution surrounding MC-1 cells. This was the most successful of the sample preparation methods with which I was involved, but the resulting sample (Figure 3.1) was still not as good as the MV-1 sample provided by Dr. Lins (see Chapter 4).

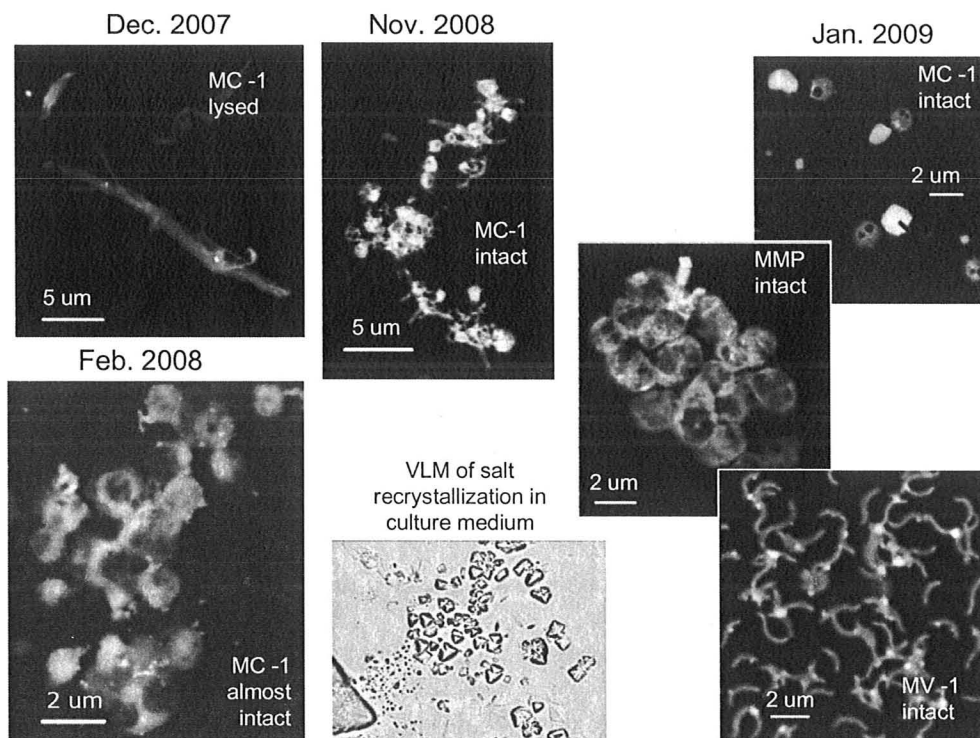


Figure 3.1 – The progression of various different MTB sample preparations in attempts to minimize cell lysis. Sample preparations from January 2009 were provided by collaborator, Professor Ulysses Lins. The VLM image shows a recrystallization of the high concentration of salts present in the MTB culture growth medium.

3.2 Data acquisition procedure

3.2.1 STXM measurements

STXM provides spectral data by measuring transmission signal at a range of photon energies. Data is collected by recording at a single location (point XANES mode), recording the same line at a sequence of energies (line scan spectra mode), or recording complete images at a sequence of energies (image

sequence or “stack” mode). The photon energies used are specific to the absorption edge of interest and the variable point spacing is optimized to track relevant spectral features while minimizing the radiation dose. STXM measures the transmitted X-ray signal at a given pixel by single photon counting for a specified dwell time interval. Depending on the type of data being collected, dwell times range from 0.2 to 10 ms per pixel at each photon energy.

Radiation damage and carbon build-up both limit the useable time with which one can study the MTB sample. Radiation damage refers to the induced chemical or structural modifications in a sample as a result of exposure to ionizing radiation such as x-rays. The extent and type of damage depends on the nature of the material. Organic and biological molecules are much more sensitive and susceptible to radiation damage than inorganic materials. It is possible that the spectral signature of XMCD may be altered at high radiation dose. The organic surroundings are certainly heavily damaged by the doses needed to measure XMCD. Thus, the C 1s, O 1s and other non-Fe edges are measured in an area of interest before starting the XMCD measurements. Fortunately, inorganic magnetite magnetosomes are relatively robust under radiation, thereby leaving their XMCD signals largely unaffected.

Carbon build-up refers to the cracking of hydrocarbon contaminants on the surface of the sample when it is irradiated for the many minutes needed to measure XMCD. Carbon build-up can contribute to an overestimate of the

thickness of the sample (due to increased absorption by the sample). This latter aspect is especially problematic for XMCD measurements where the different polarization signals are measured sequentially, since the subtle dichroic spectral differences between LCP and RCP measurements can be masked by the increased absorption of carbon build-up on the sample.

Since the carbon XAS signal from (biological) organic components are impacted the most by carbon build-up and radiation damage, the C1s edge should be studied first. Another advantage of starting measurements at the C1s edge is that it allows for identification of regions on the sample which contain the biological material. This is especially helpful in cases where the cells or biological material of interest is only sparsely distributed on the TEM grid or Si₃N₄ window. In order to locate cells, one records a biology map, which is the difference of images obtained on (288.2 eV) and off (280 eV) the strong C1s → π*_{C=O} amide peak of protein. Once suitable areas are located, analytical measurements such as linescan spectra (recording the same line at a sequence of energies) or stacks (recording complete images at a sequence of energies) are performed. It is important to note that in all spectroscopy, a measurement of the incident flux signals or an I₀ region (off of the region of interest) is needed in order to convert the transmission signal into optical density (absorbance). The conversion involves the Beer-Lambert Law:

(Eq. 3.1a)
$$I_t = I_0 e^{-\sigma \rho t}$$

or

$$\text{(Eq. 3.1b)} \quad \text{OD} = \ln(I_0/I_t) = \sigma(E)\rho t$$

where I_0 and I_t represent the incident and transmitted x-ray photon intensity and are measured separately by performing an energy scan on and off the region of interest, respectively. The natural logarithm of the ratio, I_0/I_t , gives the optical density (OD), which is related to the density (ρ), thickness (t) and energy-dependent mass absorption coefficient (σ) of the sample.

An I_0 measurement involves having the light path traverse a bare region of Si_3N_4 (for samples mounted on a silicon nitride window) or on formvar (for samples mounted on a formvar-coated TEM grid). The I_0 measurement could either take the form of a single point scan or be included within the field of view of the stack measurement. The latter, which constitutes the measurement of an *internal* I_0 (like double-beam spectrophotometry), as opposed to an *external* I_0 (like single-beam spectrophotometry) is preferred, particularly for XMCD, since it can help correct for variations in the beam intensity due to shifts in the trajectory of the electron beam in the storage ring and also for changes in transmission due to carbon build-up.

Following C1s measurements, the Fe 2p edge of MTB samples was studied. Fe^(III) maps (on/off: 710/702 eV) were used to locate magnetosomes and full Fe 2p stacks (700-730 eV) or Fe L_3 (702-716 eV) stacks was recorded with sufficient pixel density and dwell time to allow measurement of the weak XMCD.

Since magnetosomes are only 30-50 nm wide, care must be taken to ensure proper focus. The investigation of individual magnetosome chains requires the acquisition of stack measurements at a very small scale (ie. image dimensions \sim 1-2 μm or less) in order to visualize the individual particles. However, drifts (caused by thermal effects or misalignment) of up to 0.1-0.5 μm , typically towards the top-left corner, occurred during extended periods of stack acquisition (3-6 hours) (see Figure 3.7). In order to compensate for this drift without requiring excessively large scan regions, the initial field of view was offset such that the magnetosomes remained in view throughout the drifting stack. This step is especially crucial in the case of small-scale stacks, regardless of the edge being studied. Additionally, the dimensions of the small-scale stacks must be enlarged by the magnitude of the expected drift (0.1-0.5 μm) in order to avoid losing the region of interest from the field of view (FoV). To inspect the level of radiation damage and carbon build-up following prolonged stack measurements, a damage image, in the form of an image 2-3 μm larger than the stack FoV, is measured, using a photon energy most sensitive to the damage (288.2 eV or 708 eV) or to the carbon (289 eV) and pre-Fe 2*p* regions.

3.2.2 Sample Mounting

The detection of in-plane MTB magnetic moments requires a tilted/rotated sample mount in order to create a component of the magnetic moment parallel to the propagation direction of the beam of circularly polarized x-rays (see Section 2.3.1.1, Figure 2.5). Various tilted sample mounts were used throughout the course of this project. The first tilted sample mount used in this project during measurements in April 2008 at the ALS STXM 11.0.2, involved mounting the sample STXM plate onto a base, whose angle could be rotated by 30° and then fixed into place by screws. This proved to be effective in detecting XMCD. However, since the sample scanning is limited to scan only the x-direction of the tilted stage, the range of in-focus sample scanning was very small (~1-2 μm). In addition, extreme care had to be taken when making large x motions to avoid hitting the OSA.

The second method used a tomography rotation stage (Johansson *et al.*, 2007) (Figure 3.2 (a)) that is affixed to the STXM sample plate and allows user-specified, in-situ rotation executed by the computer-controlled encoded motor. The sample on a TEM grid is mounted on a thin copper plate, which is attached to a tomo stub (Figure 3.2 (b)), which is subsequently inserted into the rotation structure. This method worked well since the rotation structure is compact and therefore, did not pose any physical obstructions to the tight working space of

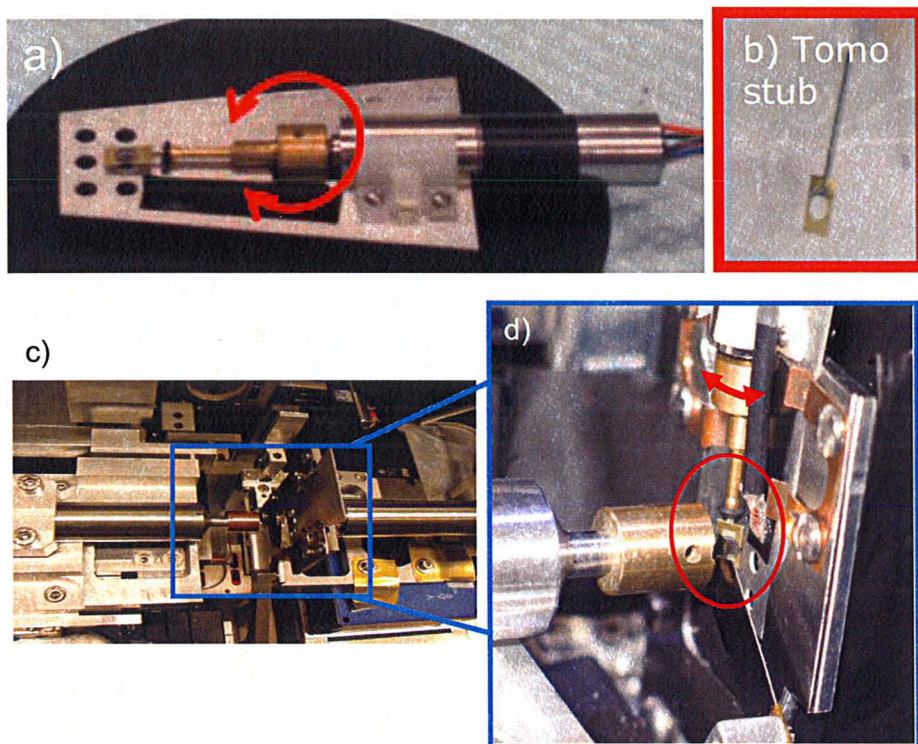


Figure 3.2 – (a): Photo of the tomography rotation stage, along with the inserted tomo stub containing a mounted TEM grid. Rotation about the y-axis may be specified by the user from an external computer when the tomo stage is positioned vertically inside the STXM tank. (b): Tomo stub with the TEM grid sample removed. (c) Inside of STXM; (d) Zoomed-in view of the geometry and configuration of the ZP, OSA, sample and tomo stage components within STXM.

STXM (Figures 3.2 (c) and (d)), which is limited by the A_0 (OSA-to-sample distance) parameter of 300-900 μm .

The third method, suggested by Bonnie Leung, involved mounting the sample on a wedge. In this method, the sample on a TEM grid is mounted across a 2.4-mm hole on an aluminum wedge inclined at 30° (Figure 3.3), which is

affixed over a hole in the sample plate. This method also worked well due to its compact structure.

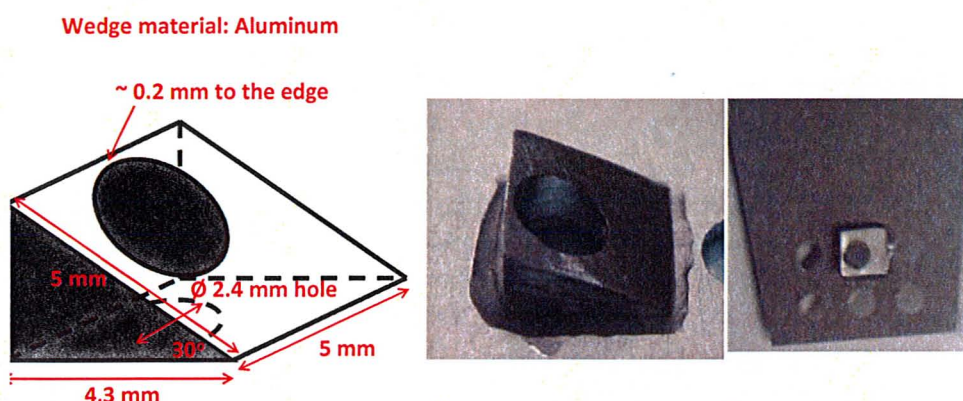


Figure 3.3 – Left: Wedge dimensions; Middle: Close-up of wedge; Right: Zoomed-out view of wedge mounted on a sample plate.

3.2.3 XMCD measurement

3.2.3.1 XMCD maps

In order to make XMCD measurements, spectromicroscopy signals are acquired with left and right circular polarizations of light. Switching to a desired circular polarization is done via the STXM_control software (Figure 3.4) and by following the EPU codes listed in Table 3.1. Because we are interested in measuring XMCD, a preliminary check can be done by obtaining an XMCD map, analogous to the way that elemental on/off-edge maps are measured. However, rather than measuring images at two different energies, images are measured at a single energy but at both circular polarizations – left (LCP) and right (RCP). The

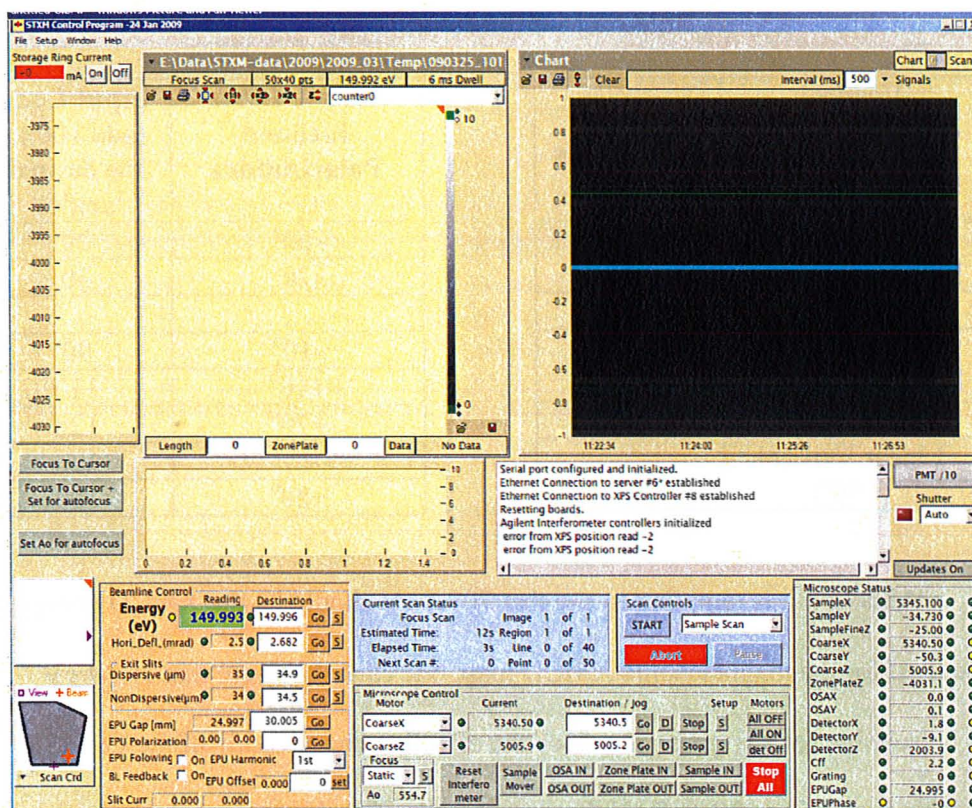


Figure 3.4 – Screenshot of the STXM control window. Polarization is changed in the text box labeled “EPU Polarization” under the Beamline Control box in orange. (see Table 3.1 for codes)

XMCD energy, the energy of maximum XMCD signal, is 708.9 eV for magnetite.

In the case of stoichiometric magnetite, the maximum XMCD signal is known to occur at the d^6O_h site of the crystal structure, which corresponds to the first negative peak in the XMCD spectrum. The energy for this peak may be determined either by referring to an XMCD spectrum obtained previously or from literature. In this case, a reference XMCD spectrum of magnetite from the work of Goering *et al.*, (2007) shows that the d^6O_h XMCD peak occurs at 709.4 eV.

Table 3.1 – EPU control codes

Vertical, Circular and Horizontal Polarizations	Input Code	Inclined Polarizations	Input Code (add 100 to the desired angle)
Linear Vertical (-90°)	-2	-80°	20
Circular left	-1	-70°	30
Linear Horizontal (0°)	0
Circular right	+1	-10°	90
Linear Vertical (+90°)	+2	+10°	110
		+20°	120
	
		+80°	180

Although it is tempting to say that 709.4 eV should be the XMCD energy to be used for the magnetosome XMCD map, one cannot be sure that 709.4 eV will be suitable for any given run since the effective energy scale of the CLS-SM beamline varies from 0.1 to 2 eV from run-to-run. For this reason, the best energy for XMCD mapping should be determined experimentally at the time of any given run. In fact, when CLS-SM is properly calibrated, the maximum XMCD signal (d^6O_h) of magnetite magnetosomes is measured at 708.9 eV. As this value has been confirmed in multiple runs on separate occasions, therefore, we can say with confidence that the maximum XMCD energy occurs at 708.9 eV. In cases where there are slight shifts in the energy scale between runs, the peak in the spectrum containing a single sharp peak is assigned a value of 710.1 eV, since the energy difference between the XMCD d^6O_h peak and the peak maximum in the polarized spectrum is 1.2 eV, as explained below.

3.2.3.2 Fe 2p spectroscopy of magnetite

Given that there is a component of the magnetosome chain magnetic moment projected out-of-plane of the sample, depending on the alignment of the chain magnetic moment with respect to the helicity of light, the Fe 2p L_3 -edge spectrum will show either: a) a single sharp peak, in the case of parallel alignment; or b) a broad peak with a slight shoulder on the left, in the case of anti-parallel alignment (Figure 3.5). If the spectrum shows a single sharp peak, the maximum XMCD energy can be determined by the following formula: Maximum XMCD energy = Energy at peak – 1.2 eV, since the energy difference between the d^6O_h XMCD peak and the consecutive d^5T_d XMCD peak is 1.2 eV.

On the other hand, if the spectrum shows a shoulder on the low energy side of the main peak, the formula is: Maximum XMCD energy = Energy of shoulder, since overlay of the parallel and anti-parallel spectra reveals that the maximum XMCD energy (ie. Energy of first negative peak in XMCD spectrum) is directly related to the position of the shoulder in the anti-parallel spectrum (Figure 3.5). Once the maximum XMCD energy is determined, measurement of the XMCD map may now be carried out.

From the analysis of an XMCD map (see Section 3.3.2), one can determine whether the region studied contains sufficient XMCD signal worthy of further detailed and thorough XMCD investigation. If not, XMCD maps are measured until a candidate region that shows XMCD is found. The regions of

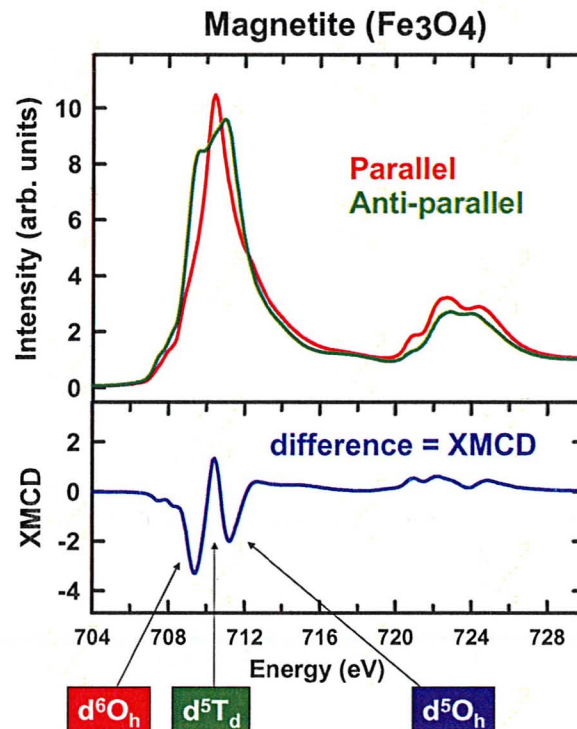


Figure 3.5 - Fe L_3 spectra of magnetite measured with the magnetic moment aligned parallel and anti-parallel to the helicity of circular polarized x-rays, with the resulting XMCD difference spectrum plotted along the bottom. (Plotted with data from Goering *et al.*, (2007)). The 3 XMCD peaks correspond to the 3 types of Fe sites ions in the crystal structure.

interest were chosen to be those areas which contain magnetosome chains that are oriented orthogonal to the axis of the tilt/rotation of the sample mount. It is important that the selected magnetosome chains are orthogonal to the axis of rotation of the sample since for chains parallel to the axis of rotation, the magnetic moment remains in-plane at all tilt angles. This concept is illustrated in Figure 3.6. In all sample mounts used in this work, the sample was rotated about the y-axis, and thus, *horizontally-oriented* magnetosome chains were studied.

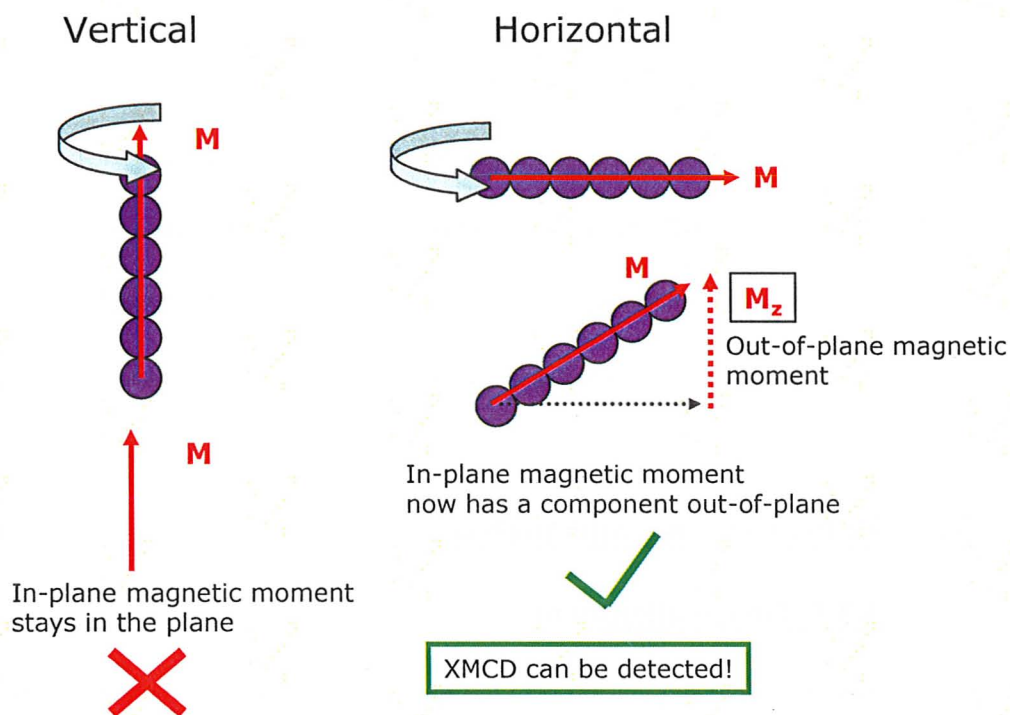


Figure 3.6 – Illustration of the effect of magnetosome chain orientation on the detection of the in-plane magnetic moment. The current case illustrated assumes a tilted sample mount about the y-axis, demonstrating the need for selection of a horizontally-oriented magnetosome chain.

3.2.3.3 XMCD stacks

XMCD stacks are image sequences measured over an user-defined energy range, which are additionally measured at both left and right circular polarizations at each photon energy. They are a preferred method for achieving high quality XMCD data. The alternative, and less favourable, method to measure XMCD signal is to acquire an entire stack at one circular polarization then switch to the

other. Description of how to set-up XMCD stacks and define necessary parameters are given in the CLS-STXM beamline manual. In both methods of XMCD stack acquisition, the need to account for 0.1 - 0.5 μm drifts in small-scale stacks (dimensions \sim 1-2 μm or less) continues to apply. The analysis, as well as the advantages and disadvantages, for the two methods of XMCD stack measurement are described in sections 3.3.1 and 5.1 below, respectively.

3.3 Data processing and analysis

3.3.1 Image alignment

Stacks (image sequences) provide spectral data per image pixel, however, meaningful spectral data can only be derived if the signal corresponds to the same location in each image at each energy. Typically, despite interferometer control, there are image-to-image shifts of 10-20 nm leading to overall shifts of 0.1 - 0.5 μm in a stack (Figure 3.7). These must be removed by a combination of auto- and manual alignment prior to extraction of the spectra of individual magnetosomes. Auto-alignment using the ‘Zimba’ routines in aXis2000 are generally performed first. In cases where a single round of auto-alignment is not sufficient to obtain optimal image alignment, multiple re-alignments are carried out and manual alignments (using ZIMBA) may even be performed. In a 1-point manual alignment, an image feature seen in each image is aligned to the same co-

ordinate. This is followed by a spatial truncation of the image sequence to that same region present in all images. The quality of alignment is monitored by summing images and performing successive alignments until the halo-like regions of misalignment surrounding the magnetosomes or cells are minimized. It is important that alignment is performed on image sequences prior to the selection of an internal I_0 region and subsequent conversion into optical density.

When considering the alignment of XMCD stacks, the method of alignment is the same with the exception of a few additional steps prior to and following the alignment procedure, depending on the type of XMCD stack. If an XMCD stack is collected such that a single stack at a given circular polarization is acquired separately from that at the other polarization, the processing of that data requires the following steps: 1) individual alignment of stacks collected at left and right circular polarizations (LCP and RCP); 2) appending LCP and RCP stacks into a single stack; 3) alignment of the combined LCP-and-RCP stack; and 4) separation of the combined stack into the original respective LCP and RCP

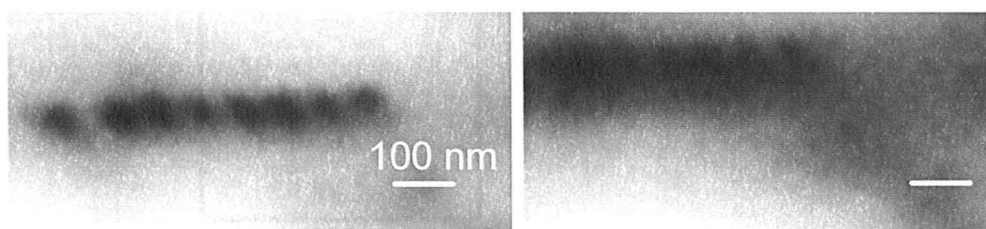


Figure 3.7 – Two images from an image sequence showing drift in the field of view over time, thereby, highlighting the importance of alignment procedures prior to data analysis.

component stacks. Depending on the magnitude of drift observed in the respective LCP and RCP stacks, the alignment (step 3) of the combined stack can be a time-consuming and lengthy procedure. Furthermore, another disadvantage of acquiring discrete XMCD stacks is the inability to properly align and correct for image distortions that can occur over time and vary between the LCP and RCP stacks (Figure 3.8). Under these circumstances, the two stacks were not appended and thus, were only aligned individually, meaning that the regions of interest (ROI) studied did not correspond to the same pixel locations in both stacks.

In the case of an XMCD stack, the alignment procedure requires: 1) alignment of the entire stack, while keeping images sorted in ascending order of

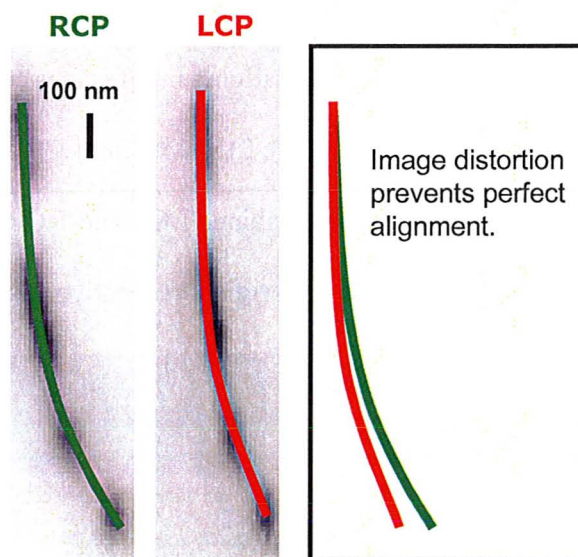


Figure 3.8 – Example of image distortion occurring in a pair of discrete XMCD stacks, which prevents the two stacks from being appended and properly aligned together.

energy; and 2) separation of the stack into the respective LCP and RCP component stacks. The higher precision, shorter time and greater ease with which alternating XMCD stacks are processed are all significant advantages of acquiring XMCD stacks over measuring the LCP and RCP stacks sequentially.

3.3.2 Maps: on/off elemental and XMCD

Measurement of a series of two images – on and off an absorption edge of interest – allows identification of regions that contain the element of interest. In order to ‘highlight’ these regions, alignment of the 2 images is performed, followed by conversion of the transmission images to optical density, and finally subtracting the ‘off-edge’ image from the ‘on-edge’ image. The resulting difference image cancels out any background absorption present at the two energies and reveals only those regions that have a net absorption from the element of interest (Figure 3.9). Multiple elemental maps can be combined as RGB colour composites to show the relative spatial distribution of different elements.

Analysis of XMCD maps follows a similar procedure. However, the ‘highlighted’ regions correspond to those regions containing XMCD signal, rather than a particular chemical element of interest. In the study of magnetosomes, these XMCD maps provide a quick glimpse of potential XMCD regions for detailed XMCD studies. Figure 3.10 is an example of an XMCD map from a

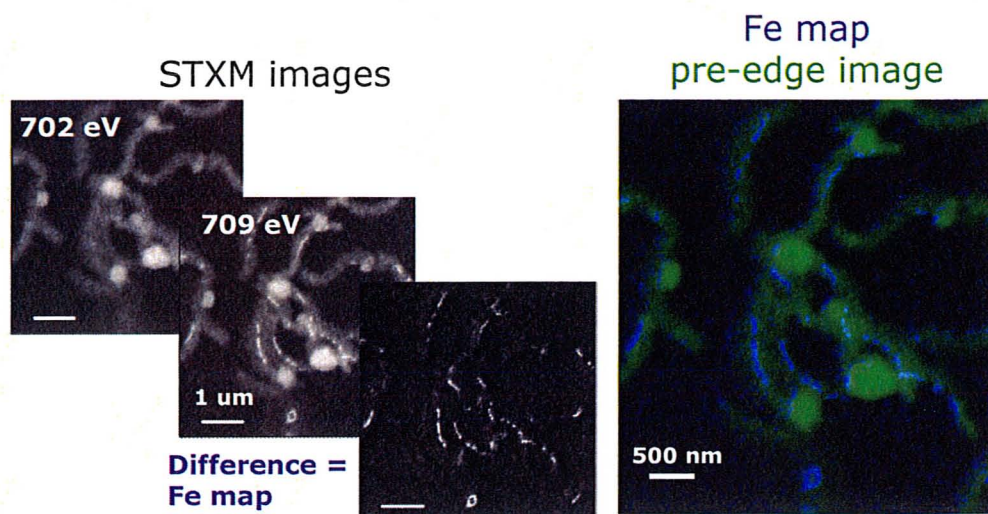


Figure 3.9 – Left: Example of single component mapping (of Fe, in this case). Subtracting the off-edge (702 eV) image from the on-edge (709 eV) image reveals those areas containing the element of interest (Fe). Right: The resulting difference Fe map in colour (*blue*: Fe; *green*: organic matter).

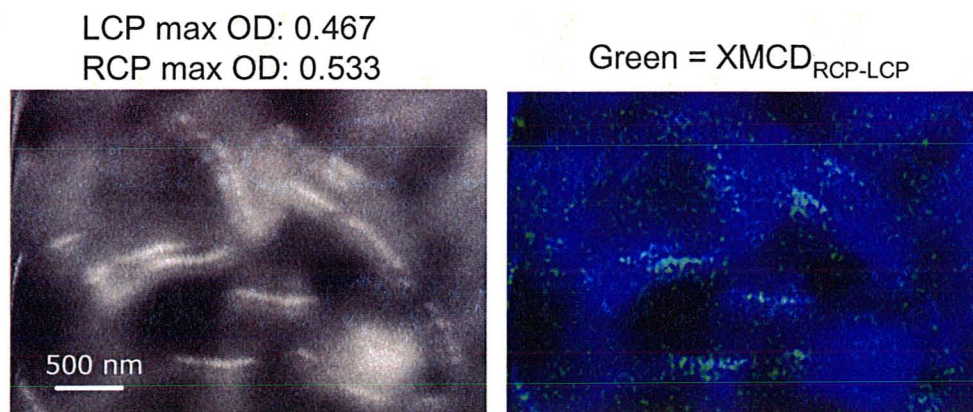


Figure 3.10 – Example of an XMCD map. Left: An optical density image taken at either LCP or RCP; Right: The difference between the LCP and RCP optical density images produces an XMCD map, which is highlighted in *green*. Green regions indicate the presence of XMCD, which is mainly observed in horizontal chains in this case.

region of MV-1 cells. It reveals that the sample mount rotated about the y-axis, as used here, results in the presence of XMCD in mainly the horizontally-oriented magnetosome chains. This observation is consistent with the concept illustrated earlier in Figure 3.6 and is evidence of the magnetosome chains' magnetic dipoles being in the plane of the sample. Regions that do not show XMCD in the XMCD map would not be considered for follow-up XMCD investigations.

3.3.3 I₀ region

Measurement of an I₀ region, which does not contain absorption by cells or magnetosomes, is needed to convert the transmission signal into optical density (absorbance). An I₀ region may be measured separately at a single point in the form of a point scan or could be included within the field of view (FoV) of the stack measurement. The latter, which constitutes the measurement of an *internal* I₀, as opposed to an *external* I₀, is preferred since it helps correct for variations in beam intensity.

Whereas the measurement of an external I₀ merely requires the measurement of spectra at a single point away from the region of interest, the selection of an internal I₀ region requires certain criteria to be met prior to its consideration as an appropriate I₀ region: 1) the region must be free of any other material of interest (eg. No biological material); and 2) the region should be sufficiently large such there are adequate statistics. Figure 3.11 shows an

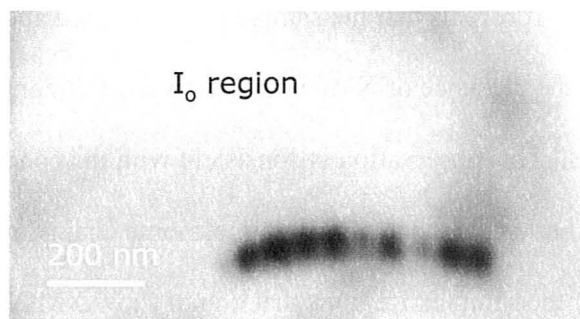


Figure 3.11 – Example of an image showing an appropriate internal I_0 region within the field of view.

example of an appropriate internal I_0 region within the field of view of an image sequence.

An XMCD image sequence consists of two stacks collected at both circular polarizations. The conversion into optical density requires a common internal I_0 region. Following the proper alignment of the appended LCP/RCP stack, the desired internal I_0 region is selected and the appended stack is converted into optical density by the software. The appended OD stack may then be separated into their respective LCP and RCP component stacks. Alternatively, OD conversion may also take place after the appended stack has been separated. In this case, selection of the internal I_0 region from one stack at a given polarization will need to be saved as an ROI (region-of-interest) file such that the same region may be used as the internal I_0 in the other stack.

3.3.4 Extracting XMCD spectra from image sequences

XMCD spectral data are obtained from image sequences at both left and right circular polarizations, whether acquired in two separate stacks or by a single XMCD stack. Once the individual LCP and RCP stacks have been converted to OD, spectra from each of the stacks may be extracted by selecting regions of interest (ie. magnetosomes). In order to ensure that the spectra correspond to identical regions in each stack, the selected areas/pixels are saved as ROI files, which can then be read into the second stack file for extraction of spectral data from the identical set of pixels. To allow for comparisons of XMCD signal between individual magnetosomes and the overall chain average, multiple ROI files corresponding to individual magnetosomes and the total chain area are created.

XMCD spectral data are generated by subtracting the LCP signal from the RCP signal. The XMCD spectral signature may be observed in the difference of the two image sequences. Observation of the images at each of the L_3 XMCD peaks shows inversion of the negative-to-positive signal and vice versa, which reflects the antiferromagnetic coupling of the three Fe cation sites: $\text{Fe}^{2+} \text{O}_h$, $\text{Fe}^{3+} \text{T}_d$, and $\text{Fe}^{3+} \text{O}_h$. Figure 3.12 shows an example of such a difference stack in which two magnetosome chains are revealed to possess identical directionality in their respective magnetic moments, along with inversion of signal at the three peak energies of the magnetite XMCD signal.

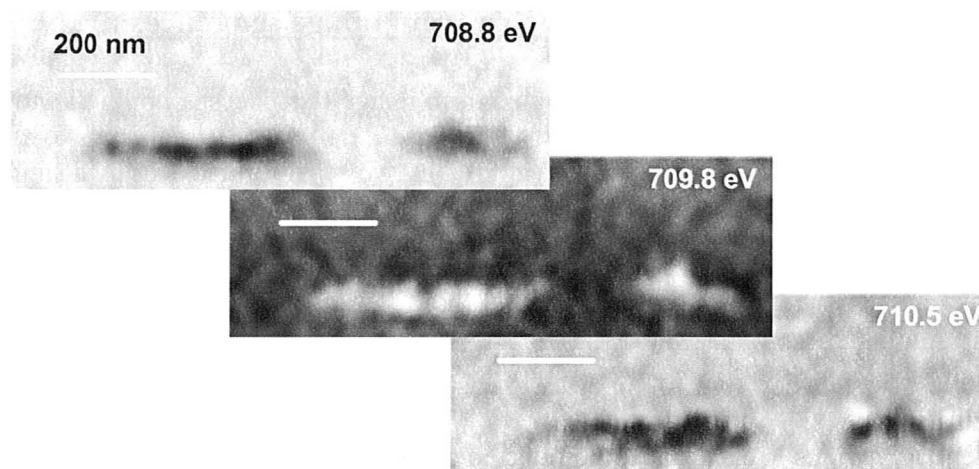


Figure 3.12 – Example of XMCD difference images generated by the subtraction of one stack at a given polarization from the other (RCP minus LCP, in this case). Both magnetosome chains possess identical magnetic orientation. Furthermore, their relative positive/negative signals are inverted at the three XMCD peak energies of magnetite.

3.3.5 Verification of data

When the data is of good quality and the analysis is done correctly, the three-peak XMCD signature of magnetite is readily observed. Once XMCD is confirmed to be present, the magnitude of the observed XMCD signal relative to that of reference magnetite is determined and compared. In this project, the magnetite spectra that were used for reference and quantification purposes were taken from the published work of Goering *et al.* (2007). To quantify the XMCD signal of magnetosomes relative to that of reference bulk magnetite, corrections are needed to take into account sample thickness and the experimental geometry. Prior to generating the XMCD spectrum, the edge jump ($I_{730\text{ eV}} - I_{702\text{ eV}}$) of the Fe edge in

the magnetosome spectra of magnetosomes and of bulk magnetite, which show a single sharp peak, are normalized to 1. The spectrum of the other polarization is then multiplied by the same normalization/scaling factor. In comparison to the literature data, the XMCD spectrum of bulk magnetite was reduced by a factor of 2 in order to account for the fact that only 50% of the XMCD signal would be detected in the 30° geometry (see Figure 3.13). In the quantification of the XMCD signal of individual magnetosomes, the intensity of the Fe L_3 edge is also normalized to 1.

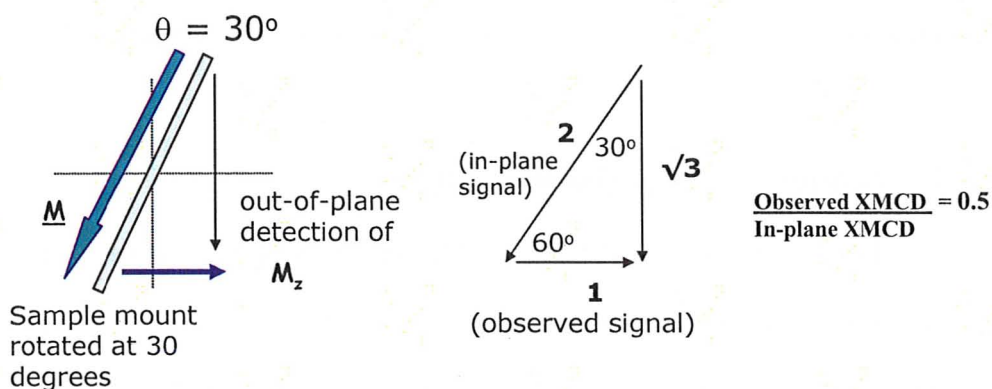


Figure 3.13 – Illustration of the effect of sample geometry on the magnitude of the measured XMCD signal relative to the intrinsic in-plane XMCD signal.

3.3.6 Spectral fitting (Q-Fit) for determining site occupancies

Q-Fit is a fitting program developed by Neil Telling (while at Daresbury Laboratory, Warrington, U.K). It fits the three theoretical components, ($\text{Fe}^{2+} \text{O}_h$, $\text{Fe}^{3+} \text{T}_d$, and $\text{Fe}^{3+} \text{O}_h$) in stoichiometric magnetite (1:1:1) to experimental spectra in order to deduce the occupancy at each site. Theoretical magnetite spectra are

calculated using the atomic multiplet/charge transfer method developed by van der Laan and Thole (1991). The intensities of the three peaks at the L_3 of the XMCD magnetite spectrum were fit over 704-712 eV by first performing auto-fitting by the software which is based on linear least-squares analysis, and then carrying out subsequent manual refinements of the fit. The experimental spectra were fit over the L_3 region only. The relative energy positions of XMCD signal from the different Fe sites in the calculated spectra were shifted as needed to obtain the best fit to the experimental spectra. An example of spectral fitting by Q-Fit in order to determine cation site occupancies is found in Appendix 5.

3.4 Sequence of experimental studies

The development of STXM-XMCD, which was the main achievement of my thesis study, consisted of a number of stages. Table 3.2 outlines the sequence of these stages, as well as the associated highlights and/or challenges encountered in each stage. While the next chapter is a publication of STXM-XMCD measurements made on MV-1, examples of some of the STXM-XMCD data measured on MMP are found in Appendix 3.

Table 3.2 – Summary and sequence of experimental studies

Dates	Location	Sample	Source	Comment
Sept. – Dec. 2007	ALS BM 5.3.2	FeGd multilayer	Hitachi Global Storage Technologies	ALS 5.3.2 revealed XMCD from large out-of-plane domains in sample with opposing magnetic orientations
		CoPt multilayer		CLS STXM has the ability to measure XMCD from small (100 nm) out-of-plane magnetic domains in sample with opposing magnetic orientations
Dec. 2007 – Feb. 2008	CLS 10ID-1	Strain MC-1 MTB	Supplied by Dr. Arash Komeili and cultured at NWRI	Observation of Fe 2p signal and differences in Fe(II) and Fe(III) oxidation states found in magnetosomes → Evidence of cell lysis: cells do not show the expected coccoid and spherical morphologies of MC-1 → better sample preparation is needed
Feb. 21-24, 2008				First XMCD attempt on MC-1 at CLS STXM but lack of a tilted sample mount prevents detection of in-plane magnetic moments of magnetosomes → cell lysis still observed
April 2008				→ 30°-rotated sample mount was used (from this point forward) to create an out-of-plane component of the in-plane magnetosome magnetic moments → first XMCD observation in <i>lysed</i> MC-1 cells
Nov. 14-15, 2008	ALS BM 5.3.2	Strain MC-1 and MMP MTBs	Supplied by Profs. Ulysses Lins and Dennis Bazylinski	→ both MC-1 and MMP samples show intact cells → unable to find magnetosomes in MC-1 cells
Jan. 2009	CLS 10ID-1	Strain MV-1 MTB	Supplied by Prof. Ulysses Lins	→ MV-1 shows neatly aligned single magnetosome chains → measurement on a vertical chain does not yield any XMCD

Table 3.2 – Summary and sequence of experimental studies (cont'd)

Dates	Location	Sample	Source	Comment
March 2009	CLS 10ID-1	Strain MV-1 MTB	Supplied by Prof. Ulysses Lins	→ first observation of XMCD in single magnetosomes of MTB (!) → see differences in XMCD intensity between horizontal and vertical magnetosome chains
May 2009				→ confirmation of XMCD signal with sample mounted on 30°-inclined aluminum wedge
July 2009				→ first attempt at simultaneous x-, z-scanning for a greater field of view at 30 degrees → XMCD signal still measured even without x, z-scanning working yet
Sept. 2009				→ first successful XMCD measurement with alternating polarization at each photon energy (best data to date) → observation of opposite XMCD signal in two magnetosome chains having oppositely aligned magnetic orientations – observed within the same field of view
Nov. 2009		MTB with mixed magnetosomes (Fe ₃ O ₄ and Fe ₃ S ₄)	Supplied by Prof. Dennis Bazylinski	→ Fe ₃ O ₄ and Fe ₃ S ₄ magnetosomes can be differentiated by STXM via O 1s spectroscopic measurements
January 2010				XMCD measurements to be continued...

Chapter 4

CHARACTERIZING MAGNETISM OF INDIVIDUAL MAGNETOSOMES BY X-RAY MAGNETIC CIRCULAR DICHROISM IN A SCANNING TRANSMISSION X-RAY MICROSCOPE

(Under the supervision of A.P. Hitchcock, all measurements and data analysis were performed by K.P. Lam, in addition to preparation of the manuscript.)

This chapter of the thesis is derived from the published manuscript:

Lam, K.P., A.P. Hitchcock*, M. Obst, J.R. Lawrence, G.D.W. Swerhone, G.G. Leppard, T. Tyliczszak, C. Karunakaran, J. Wang, K. Kaznatcheev, D.A. Bazylinski and U. Lins (2010), *Chemical Geology*, 270, 110-116.

Reproduced with permission from © Elsevier B.V.



Characterizing magnetism of individual magnetosomes by X-ray magnetic circular dichroism in a scanning transmission X-ray microscope

Karen P. Lam^a, Adam P. Hitchcock^{a,*}, Martin Obst^{a,1}, John R. Lawrence^b, George D.W. Swerhone^b, Gary G. Leppard^c, Tolek Tyliczszak^d, Chithra Karunakaran^e, Jian Wang^e, Konstantin Kaznatcheev^e, Dennis A. Bazylinski^f, Ulysses Lins^g

^a Brockhouse Institute for Materials Research, McMaster University, Hamilton, ON, Canada L8S 4M1

^b Environment Canada, National Water Research Institute, Saskatoon, SK, Canada S7N 3H5

^c Environment Canada, National Water Research Institute, Burlington, ON, Canada L7R 4A6

^d Advanced Light Source, Lawrence Berkeley National Laboratory, Berkeley, CA, 94720, USA

^e Canadian Light Source Inc., University of Saskatchewan, Saskatoon, SK, Canada S7N 5C6

^f School of Life Sciences, University of Nevada at Las Vegas, Las Vegas, NV, 89154-4004, USA

^g Departamento de Microbiologia Geral, Instituto de Microbiologia Professor Paulo de Góes, Universidade Federal do Rio de Janeiro, 21941-590, Rio de Janeiro, RJ, Brazil

ARTICLE INFO

Article history:

Received 14 August 2009

Received in revised form 16 November 2009

Accepted 16 November 2009

Editor: J. Fein

Keywords:

X-ray magnetic circular dichroism

XMCD

Scanning Transmission X-Ray Microscopy

STXM

Magnetotactic bacteria

Magnetosomes

Magnetite

Fe O

Marine vibrio

Strain MV-1

ABSTRACT

Soft X-ray scanning transmission X-ray microscopy (STXM) was used to measure the Fe L_{2,3} X-ray magnetic circular dichroism (XMCD) signal from individual, 30 nm diameter magnetosomes in a magnetotactic bacterium, specifically the marine vibrio strain MV-1. The Fe L_{2,3} spectra recorded with circularly polarized X-rays from an elliptically polarizing undulator were very similar in shape and magnitude to those of fully saturated magnetite (Fe₃O₄). As previously determined by other techniques, our results show that the magnetic moments of individual magnetosomes arranged in linear chains in intact cells of strain MV-1 are all oriented in the same direction. The magnitude of the XMCD signal averaged over a chain of 9 magnetosomes in one cell is similar to that of single crystal magnetite. The spectral shape is slightly different, and indicates that magnetosomes have excess Fe^{III}, as noted in previous bulk studies of biogenic magnetite. To our knowledge, this is the first measurement of the XMCD of individual magnetosomes in magnetotactic bacteria.

© 2009 Elsevier B.V. All rights reserved.

1. Introduction

Magnetotactic bacteria (MTB) are Gram-negative, motile, aquatic and microaerophilic/anaerobic bacteria, found in both freshwater and marine environments, that migrate with respect to the earth's magnetic field (approximately 0.5 G) in a phenomenon called magnetotaxis (Blakemore, 1975, 1982). The magnetic behaviour of these organisms is associated with intracellularly synthesized magnetic nano-crystals enclosed within membrane vesicles (Frankel and Blakemore, 1980), referred to as magnetosomes (Balkwill et al., 1980). The magnetosome mineral phase consists of single crystals of

either the ferrimagnetic iron oxide, magnetite (Fe₃O₄) (Frankel et al., 1979), or the iron sulfide, greigite (Fe₃S₄) (Heywood et al., 1991). The size of magnetosome crystals, regardless of whether they consist of magnetite or greigite, depends on the species of MTB and generally ranges from 35–120 nm (Bazylinski and Frankel, 2004). This is the size range where magnetite crystals are expected to be limited to a single magnetic domain (Dunlop, 1973; Butler and Banerjee, 1975; Kirschvink and Lowenstam, 1979; Muxworthy and Williams, 2006).

Magnetosomes have uniform, species-specific crystal habits with narrow size distributions (Devouard et al., 1998; Arato et al., 2005; Lins et al., 2005), features consistent with a biologically-controlled mineralization process (biomineralization) (Bazylinski and Frankel, 2003). Recent genetic studies confirm that the formation and arrangement of magnetosomes in magnetotactic bacteria is strongly biologically regulated (Komeili et al., 2004, 2006; Scheffel et al., 2006) although there is also evidence that environmental factors also play a

* Corresponding author. Tel.: +1 905 525 9140.

E-mail address: aph@mcmaster.ca (A.P. Hitchcock).

¹ Now Center for Applied Geoscience, Eberhard Karls University, 72076 Tuebingen, Germany.

role in the biomineralization of magnetite and greigite by magnetotactic bacteria (Blakemore et al., 1985; Bazylinski, 1996; Schüler and Baeuerlein, 1998; Bazylinski et al., 2004). Various methods of examining the chemistry, crystallography and magnetism of the magnetic materials associated with individual cells of magnetotactic bacteria or individual or chains of magnetosomes have great potential to advance the fields of magnetism, magnetic materials and biomineralization. The narrow size and shape distribution of magnetosomes has led to their consideration as candidate materials in technological, medical and environmental applications, such as magnetic recording media, ferrofluids, and magnetic resonance imaging (MRI) (Lee et al., 2005) as well as removal of Au(III) from wastewater (Song et al., 2008). Mimicking the biogenic mineralization process, uniform, superparamagnetic magnetite nano-crystals were successfully synthesized using specific proteins from magnetotactic bacteria in order to control crystal size and habit (Prozorov et al., 2007). Most recently, magnetotactic bacteria have been studied as controlled, MRI-trackable propulsion and steering systems for medical nanorobots operating in the human microvasculature (Martel et al., 2009).

Nanoscale magnetite crystals also have environmental significance. In some deep sea and freshwater lake sediments and soils, fossil bacterial magnetite appears to be the main carrier of natural remnant magnetization (e.g., Petersen et al., 1986; Kim et al., 2005) suggesting that in natural environments the biogenic formation of magnetosomes contributes significantly to the magnetic susceptibility of soils and sediments (Oldfield, 2007). Moreover, the presence of fossil magnetosomes, so-called magnetofossils, has been used as a biomarker for the past presence of magnetotactic bacteria on ancient Earth (Chang et al., 1989) and Mars (Thomas-Keprta et al., 2002).

Many different magnetic techniques have been applied to study biogenic magnetic minerals, including magnetic force microscopy (MFM) (Albrecht et al., 2005), low-temperature SQUID magnetometry (Moskowitz et al., 1993), ferromagnetic resonance (Weiss et al., 2004), and coercivity deconvolution (Egli, 2004). In addition, off-axis electron holography in the transmission electron microscope (TEM) using a Lorentz lens has been applied to visualize the magnetic microstructure of magnetosome chains (Dunin-Borkowski et al., 1998; McCartney et al., 2001; Simpson et al., 2005). X-ray magnetic circular dichroism (XMCD) (Stöhr, 1999) is a synchrotron-based technique that provides an element and site specific probe of magnetism. XMCD uses circularly polarized X-rays to measure the magnitude of the projection of the magnetic moment on the propagation direction of the X-rays. Sette et al. (1990), provided one of the earliest reports of the XMCD spectrum of magnetite. Many other studies of the XMCD of magnetite have been conducted (Kuiper et al., 1997; de Castro et al., 2001; Patrick et al., 2002; Chen et al., 2004; Huang et al., 2004; Pearce et al., 2006; Goering et al., 2006, 2007; Yamasaki et al., 2009). Recently XMCD has been applied to greigite (Letard et al., 2005), to comparison studies involving biogenic and abiogenic nano-magnetite (Coker et al., 2007; Carvallo et al., 2008) and to the monitoring of *in-vivo* formation of magnetosomes in *Magnetospirillum gryphiswaldense* strain MSR-1 (Staniland et al., 2007).

The Fe L₃ (2p_{3/2}) XMCD spectrum of magnetite (Goering et al., 2006, 2007) shows three characteristic peaks. The detailed structure is related to the presence of Fe ions in three distinct sites (Patrick et al., 2002). Specifically, the sites corresponding to the three peaks in the XMCD spectrum of magnetite are: d⁵ O_h (octahedral Fe²⁺ site, 708.1 eV), d⁵ T_d (tetrahedral Fe³⁺ site, 709.1 eV) and d⁶ O_h (octahedral Fe³⁺ site, 709.9 eV). The negative–positive–negative sense of these contributions is the result of the antiferromagnetic coupling between the spins on the O_h and T_d sites (Brice-Profeta et al., 2005). The site occupancies (relative amounts of Fe present in the three sites) in a given magnetite sample can be obtained from the relative intensities of these signals. Comparisons of the experimental XMCD spectrum with that calculated using ligand field atomic multiplet theory have shown that the proportion of magnetic contributions from the Fe²⁺(O_h): Fe³⁺(T_d): Fe³⁺(O_h) in fully magnet-

ically saturated magnetite is nearly 1:1:1 (Morrall et al., 2003; Carvallo et al., 2008). Thus accurate measurements of XMCD from biologically generated magnetite can be used to deduce information about biomineralization mechanisms and possible biochemical control of inorganic crystallization.

Scanning transmission X-ray microscopy (STXM) allows measurements of spatially-resolved near-edge X-ray absorption fine structure (NEXAFS) spectra with ~30 nm spatial resolution (Howells et al., 2007; Ade and Hitchcock, 2008). STXMs on beamlines equipped with an elliptically polarizing undulator (EPU) allow measurements of XMCD, and thus provide a means to characterize magnetic materials such as magnetosomes at high spatial resolution. In addition, if XMCD at Fe L_{2,3} edges is combined with studies of the biochemical components at the K-edges of C, N, O and the Ca L-edge, etc. (Hitchcock et al., 2005), it is possible to place the magnetic results in the context of the local biochemistry. We believe a program of research of this type offers good prospects to further understand biomineralization processes in magnetotactic bacteria and other organisms. In this initial study, we demonstrate the potential by measuring the magnetic properties of individual magnetosome chains, and individual magnetosomes in the magnetotactic marine vibrio, strain MV-1. This is the first report of an XMCD measurement of the magnetism of individual magnetosomes in intact cells to our knowledge.

2. Materials and methods

2.1. Growth and preparation of bacteria

Cells of the marine magnetotactic vibrio strain MV-1 were grown as previously described (Dean and Bazylinski, 1999). Three ml of a liquid culture of the organism was centrifuged at 4 °C at 10,000 g and washed twice in artificial sea water (Bazylinski et al., 2004). A drop (5–10 µL) of the washed cells was deposited onto 200 mesh glow discharged copper grids coated with a thin layer of carbon (~3 nm, TedPella Inc. Catalog # 01822, www.tedpella.com). The drop was left to stand for 1 min prior to removing excess liquid by placing the grid over a filter paper, followed by air-drying the samples.

2.2. Fe L_{2,3} X-ray magnetic circular dichroism (XMCD)

Fe L_{2,3} X-ray absorption spectra were measured using the STXM at BL 10ID1, the soft X-ray spectromicroscopy (SM) beamline of the Canadian Light Source (CLS, Saskatoon, Canada). The source point for the CLS-STXM is an elliptically polarizing undulator (EPU) which provides nearly 100% circularly polarized light at the Fe L_{2,3} edge (Kaznatcheev et al., 2007). Fe L_{2,3} spectra recorded in different runs at the CLS-STXM were found to have energy shifts of up to 0.5 eV, with respect to each other. The absolute energy scale of the spectra was thus determined by shifting it to give the best match to the shape of the Fe L_{2,3} spectrum of magnetite (with appropriate circular polarization) (Goering et al., 2006, 2007). Data was collected in transmission mode by acquiring sequences of images over a range of X-ray energies (image sequence or “stack” mode – Jacobsen et al., 2000). The transmission signals were converted to optical densities (absorbance) using incident flux signals measured through regions a few microns off the MV-1 bacterium under study. In order to obtain adequate statistical quality, we used extensive over-sampling (6 or 8 nm pixel sizes, even though the X-ray spot size is 30 nm) and long dwell times (5–8 ms/pixels, in contrast to typical acquisitions of 0.5–1.0 ms/pixel).

In order to determine the Fe L_{2,3} XMCD, spectra and images were recorded with right circularly polarized (RCP) and left circularly polarized (LCP) X-rays. An additional magnetic field was not applied, and thus we are measuring remnant magnetization. The magnetic moment of intact magnetosome chains is known to lie in the plane of the cell (Simpson et al., 2005). Since XMCD measures the component

of magnetization parallel to the direction of the X-ray beam, measurements were made with the sample mounted such that the plane of the sample was at 60° relative to the incident beam direction. Some measurements were made with the sample plane at 90° to the X-ray beam (conventional STXM geometry), where the XMCD signal was found to be extremely weak, confirming that the magnetic moment lies in the plane of the cells, which lie flat on the support surface. The XMCD signal is dependent on the directionality of the magnetic moment or the spatial orientation of the magnetic dipole being measured. To confirm the dependence of the XMCD signal on the directionality of magnetic moments, the MV-1 sample (still maintained at a 60-degree tilt relative to the X-ray propagation direction) was rotated by 180°. Measurements were then repeated on the same region at both circular polarizations. After this sample rotation, the distinct spectral signatures were interchanged – the spectrum measured with RCP light prior to rotation was the same as that measured by LCP light after rotation, and vice versa. XMCD thus provides the capability to map both the direction and magnitude of magnetic moments in a sample. In addition, since multiple crystal sites contribute to the magnetism of magnetite and their individual XMCD spectral contributions are well resolved (Patrick et al., 2002), it is possible to vector map the magnetization of the individual sites.

At the time measurements were made, the conventional back-and-forth alternation between RCP and LCP at each photon energy was not possible at the CLS SM-beamline due to limitations of the EPU control system and interference with other ring insertion devices. It is anticipated that use of this mode will further improve the quality and thus sensitivity of our XMCD results.

2.3. Data analysis

Although the CLS-STXM is equipped with an interferometric control system (Kilcoyne et al., 2003) which stabilizes the region under study as the energy is scanned, there is always a small amount of residual drift in the images from energy to energy, as we are pushing the instrument to its limits in this study. The measured RCP and LCP image sequences were combined into a single file, and then aligned using a combination of Fourier transform cross-correlation and manual alignment. Careful inspection of each image sequence to ensure proper alignment was essential to detect meaningful XMCD signal from the individual magnetosomes. The quality of alignment was monitored by summing images in the region of the 2p → 3d resonances. Multiple alignments were carried out as needed until the halo-like regions of misalignment surrounding the magnetosomes were minimized. The XMCD from individual magnetosomes was extracted by using thresholding techniques to select signal only from the magnetosome (typically 15–20 pixels). Data analysis was performed using aXis2000.²

3. Results

The TEM grid with the deposited MV-1 cells was mounted on a polar rotation stage (Johansson et al., 2007) and the plane of the sample was oriented at 60° relative to the X-ray direction. Images at the carbon K-edge (1s, 288.1 eV) revealed the presence of intact cells (Fig. 1a) with the curved-rod morphology typical of strain MV-1. The C and O K-edge spectroscopy of the cells revealed the protein-like spectral signatures characteristic of biological materials. The occasional 'blobs' (red in Fig. 1a), which had only a weak C 1s signal and no O 1s signal, are residual salts from the artificial sea water used to wash the sample. Imaging with higher magnification at 709 eV (Fig. 1b) revealed discrete Fe particles aligned in chains inside many, but not all, of the MV-1 cells. The absence of magnetosome chains in some

² aXis2000 is written in Interactive Data Language (IDL). It is available free for noncommercial use from <http://unicorn.mcmaster.ca/aXis2000.html>.

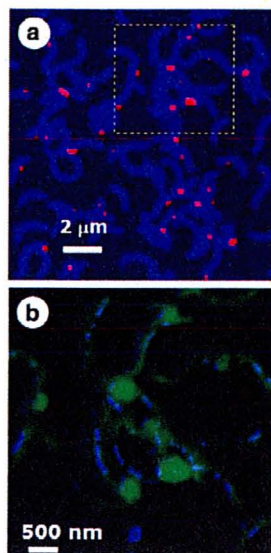


Fig. 1. (Upper) Color composite of two STXM images (optical density, OD) of intact cells of strain MV-1 in the C 1s edge – 280 eV (red) and 288 eV (blue). (Lower) Fe $L_{2,3}$ map ($OD_{709\text{ eV}} - OD_{702\text{ eV}}$, blue = Fe) of the sub-region of the upper image defined by the dotted line, superimposed on the OD image at 702 eV (green = organic matter).

cells is likely due to mutations which form non-magnetic vibrio sp. strains (Dubbels et al., 2004). A region containing both horizontally and vertically aligned magnetosome chains (Fig. 2a) was selected as the focus of our investigation. Fig. 2b, which shows the magnetosomes more clearly, displays the average of 10 images from 706–708 eV minus the average of the Fe pre-edge images from 697–704 eV, both taken from the LCP image sequence. An expanded view of 2 magnetosomes from the sum of images in the Fe L_3 peak (different sample) is shown in Fig. 2c. Fig. 2d shows a 3-D presentation of the signal in Fig. 2c to illustrate the spatial resolution and ability of the STXM to acquire signal from individual magnetosomes.

Fig. 3 plots the average Fe $L_{2,3}$ signal from the horizontal chain of magnetosomes in Fig. 2, recorded with the polarization vector of the light parallel to the magnetic vector of the chain (RCP for the sample orientation and magnetic moment of this chain) and with the polarization vector of the light anti-parallel to the magnetic vector of the chain (LCP), in each case compared with the corresponding spectrum of magnetite (Goering et al., 2006, 2007). There is very good agreement in the shapes of the Fe L_3 signal and good, but not exact agreement for the Fe L_2 signal. As shown by Kuiper et al. (1997) and Arenholz et al. (2006), magnetite also exhibits a linear magnetic dichroism (XMLD) signal which could affect these results since the experimental geometry is such that there is a component of z linear polarized light in both the right and left circular polarized measurements. However the magnitude of the XMLD signal is less than 30% of the XMCD signal, and will only be partially exhibited given the experimental geometry. Thus, while there will be a small change from the results of a measurement of the Fe $L_{2,3}$ spectrum without XMLD, this is likely at the level of our statistical uncertainty. Further this will not affect the measured XMCD signal since the linear dichroic effect is constant for both circular polarizations.

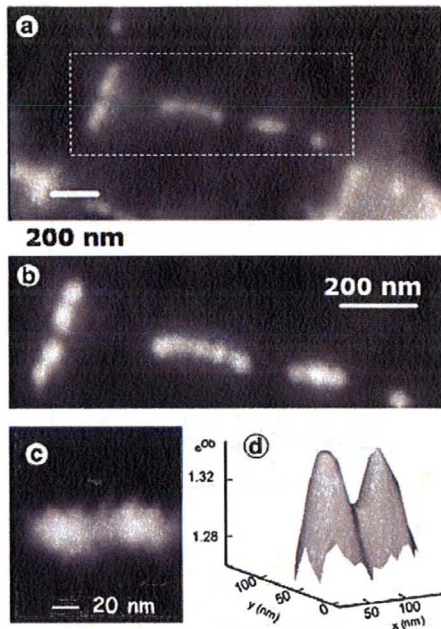


Fig. 2. (a) $Fe L_{2,3}$ optical density image at 709.3 eV of several MV-1 magnetosome chains (recorded with horizontal linear polarization). The sample is in a region free of applied magnetic field, rotated such that the plane of the TEM grid is at 60° to the X-ray beam direction. (b) Sum of 10 OD images in the region of the $Fe L_3$ peak (706–708 eV) minus the sum of 14 images in the pre- $Fe L_{2,3}$ region (697–704 eV). (c) Expansion of the $Fe L_{2,3}$ image of two MV-1 magnetosomes (different region of the same sample) showing that each is 30 nm in diameter, with a 53 nm centre-to-centre spacing. (d) 3D presentation of the signal in 3c, using an e^{90} scaling showing distinct resolution of adjacent magnetosomes at the 8% contrast level, consistent with the spatial resolution predicted for zone plates with 25 nm outer zones. All images in this figure have been smoothed using a 3 point Savitsky–Golay procedure.

An overlap plot of the parallel and anti-parallel spectra is shown in Fig. 4. The insert image indicates the 9 magnetosomes from which this signal was obtained. The XMCD signal, the difference (parallel – anti-parallel) of these spectra, is plotted in the lower panel of Fig. 4, in comparison to the published XMCD signal from single crystal magnetite (Goering et al., 2006, 2007). The XMCD intensity scale for both the magnetosome and magnetite data is based on normalizing the $Fe L_{2,3}$ edge jump ($I_{730} - I_{702}$) to unity. At the sample geometry used, 50% of the in-plane magnetic moment is projected onto the X-ray propagation axis. Thus, if these magnetosomes had the same magnetization as bulk magnetite and the moment was fully in the plane of the grid, the XMCD signal from this magnetosome chain would be 50% that of the bulk magnetite. For this reason, the intensity of the XMCD spectrum of abiotic bulk magnetite in the lower panel of Fig. 4 has been reduced by a factor of 2. The $Fe L_3$ XMCD signal of the magnetosomes is in generally good agreement in both shape and magnitude with that of magnetite. However, the first XMCD structure at 708 eV is more intense relative to that of the 709 and 710 eV features, as compared to that found in the XMCD of bulk magnetite (Goering et al., 2006, 2007). An increase in the signal of the 708 eV peak in the $Fe L_3$ spectrum of biogenic magnetite has been observed previously both in species that produce it intracellularly, as seen in *M. gryphiswaldense* (Coker et al., 2007), and extracellularly, as seen in *Shewanella putrefaciens* (Carvallo

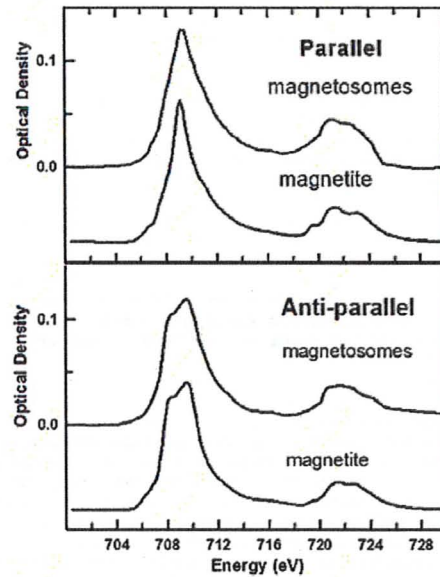


Fig. 3. $Fe L_{2,3}$ spectrum of nine magnetosomes from one horizontal chain (see insert to Fig. 4), recorded with circularly polarized light parallel (red) and anti-parallel (green) to the magnetic moment of the sample, compared to that of magnetite (Goering et al., 2007), rescaled to match the intensities of the magnetosome chain. A linear background, corresponding to the signal from the non-Fe component, has been subtracted.

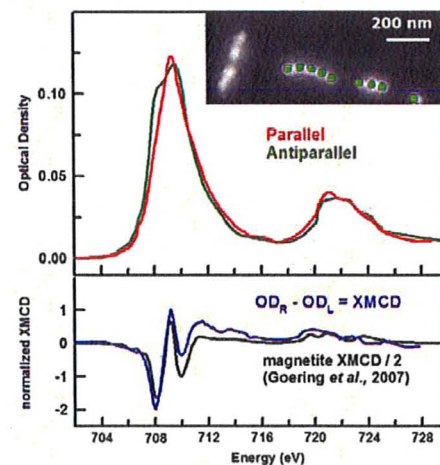


Fig. 4. (Upper) Overplot of the average spectra of 9 magnetosomes in a horizontal chain (see insert image) recorded with circularly polarized X-rays parallel (red) and anti-parallel (green) to the magnetic moment of the sample. The intensity has been scaled such that $Fe L_{2,3}$ edge jump ($I_{730} - I_{702}$) is normalized to 1. (Lower) Comparison of the resulting XMCD of the magnetosome to that of magnetite (Goering et al., 2007). The intensity scale for the XMCD of the magnetosomes is the same as that for the jump-normalized spectra in the upper plot, while that of magnetite was multiplied by 0.50.

et al., 2008) and *Geobacter sulfurreducens* (Coker et al., 2009). Coker et al. (2007, 2009) attributed the increased intensity of the 708 eV peak to non-stoichiometry, in particular excess Fe^(II), which could occur if the bio-magnetite is under-oxidized in the anoxic environment. The occupancy ratios of the three components may be determined using fitting methods, by means of non-linear least-squares analysis using calculated spectra for each Fe site, that have been well-established by Patrick et al. (2002) for a variety of spinel ferrites. The shape and magnitude of the Fe L₂ XMCD signal measured from the magnetosome chain is in less good agreement with that of magnetite, which is most likely a reflection of the limitations of the statistical precision of our present results. Higher precision is needed in the STXM-XMCD measurements to correctly reproduce the much weaker Fe L₂ XMCD structures.

Fe L₃ spectra recorded with right and left circularly polarized light from each of four individual magnetosomes in the horizontal chain are shown in Fig. 5, along with the derived XMCD, in comparison to that of abiotic magnetite. While the precision is not as good as in the spectrum averaged over all 9 magnetosomes in one chain, the Fe L₃ XMCD signal is detected, and it clearly shows the characteristic 3-peak shape of the L₃ XMCD of magnetite. Furthermore, there appears to be statistically significant variations in the 3 individual components among the four single magnetosomes sampled, suggesting that crystal-to-crystal variations within a single chain of magnetosomes could be detected with this approach. The crystal-to-crystal variations in the XMCD spectral shape are most likely due to nonstoichiometric occupancies in the three Fe sites — d⁰ O_h, d⁵ T_d, and d⁵ O_h. The non-stoichiometry is due to vacant cation sites in the structure, which arise from either oxidation or conversely, under-oxidation, of Fe (II) to Fe (III), thereby, leading to a charge imbalance (Coker et al., 2007). In the case of oxidation of Fe (II) to Fe (III), a structure having the formula, (Fe³⁺)_{1-3δ}[Fe²⁺_{1+2δ}Fe³⁺_{1+2δ}]₂O₄ = Fe_{3-δ}O₄ would result, in which the parentheses and square brackets indicate tetrahedral and octahedral sites, respectively, and δ represents the deviation from stoichiometry due to cation vacancies (Pearce et al., 2006). Since the magnetosome crystals were studied in intact bacterial cells, it is of interest to speculate how and when the magnetosome(s) could undergo oxidation. Under what conditions might the magnetite in magnetosomes in intact cells be stoichiometric? Is it possible that the observed non-stoichiometry is an artifact of sample preparation and air exposure? These and other questions will be investigated in future studies.

4. Discussion

This work has presented the first spatially-resolved observation of the magnetism of individual magnetosomes using XMCD signals measured by STXM. Comparison of the XMCD spectra of magnetosome chains to that of abiotic magnetite confirmed the mineral character of MV-1 magnetosomes, showed that the magnetization is essentially saturated, and revealed an off-stoichiometry distribution of oxidation states, which had previously been seen in bulk XMCD measurements of biogenic magnetite. These results demonstrate that STXM has the sensitivity to measure the XMCD signal of single magnetosomes. Most previous bulk studies of XMCD of magnetosomes have been carried out with total electron yield detection, which is highly surface sensitive, raising questions of possible modifications from sample oxidation. The transmission signal recorded by STXM fully samples all of the magnetosome and thus is less sensitive to such effects. At present the quality of the STXM-XMCD data is limited more by systematic than random errors. It will be greatly improved when the measurements are made by alternating between right and left circular polarization at each photon energy (i.e. a time delay of minutes between images recorded at the opposite polarizations, as opposed to the multiple hour delay, which was the case for this study).

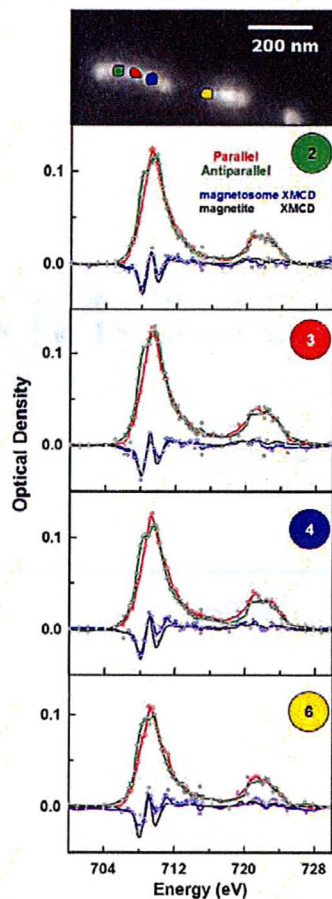


Fig. 5. Spectra of 4 individual magnetosomes in the horizontal chain — at both circular polarizations of light, with the resulting XMCD signal (on the same OD scale) superimposed on a scaled XMCD signal of magnetite (Goering et al., 2007). The image at the top identifies the areas of each of the individual magnetosomes from which these four spectra were obtained.

These results show that the STXM-XMCD technique is a sensitive tool that can determine the direction of magnetic moments at the nanoscale. With further improvements it should be possible to perform quantitative vector mapping of magnetic moments in individual magnetosomes. Applying that capability to studies of immature magnetotactic cells containing under-developed magnetite crystals, to strains with induced doping of magnetosomes (Staniland et al., 2008; Keim et al., 2009; Kundu et al., 2009), and to different MTB species, will help better understand biomineralization by magnetotactic bacteria. The technique could also be applied to abiotic or other biological nanomagnetic systems.

Acknowledgements

This work was supported by NSERC (Canada) (Hitchcock) and by U.S. National Science Foundation grant EAR-0920718 (Bazylinski). We

thank Dr. Eberhard Goering for supplying the Fe $L_{2,3}$ spectra of magnetite and Gerrit van der Laan for a helpful critical reading of a draft. Olav Hellig and Eric Fullerton (Hitachi Global Storage Technologies) and Jeff Kortrright (Lawrence Berkeley National Lab) provided synthetic out-of-plane magnetized (Pt-Co) multilayer and FeGd samples which were very useful in developing the STXM-XMCD methodology. The Canadian Light Source is supported by the Canada Foundation for Innovation (CFI), NSERC, Canadian Institutes of Health Research (CIHR), National Research Council (NRC) and the University of Saskatchewan.

References

- Ade, H., Hitchcock, A.P., 2008. NEXAFS microscopy and resonant scattering: composition and orientation probed in real and reciprocal space. *Polymer* 49, 643–675.
- Albrecht, M., Janke, V., Sievers, S., Siegner, U., Schüller, D., Heyen, U., 2005. Scanning force microscopy study of biogenic nanoparticles for medical applications. *J. Magn. Mater.* 290–291, 269–271.
- Arato, B., Szanyi, Z., Fliés, C., Schuler, D., Frankel, R.B., Buseck, P.R., Pósfai, M., 2005. Crystal size and shape distributions of magnetite from uncultured, magnetotactic bacteria, and magnetite as a potential biomarker. *Am. Mineral.* 90, 1233–1241.
- Arenholz, E., van der Laan, G., Chopdekar, R.V., Suzuki, Y., 2006. Anisotropic X-ray magnetic linear dichroism at the Fe $L_{2,3}$ edges in Fe $_3$ O $_4$. *Phys. Rev. B* 74 094407-(1-7).
- Balkwill, D.L., Maratea, D., Blakemore, R.P., 1980. Ultrastructure of a magnetotactic spirillum. *J. Bacteriol.* 141, 1399–1408.
- Bazylinski, D.A., 1996. Controlled biomineralization of magnetic minerals by magnetotactic bacteria. *Chem. Geol.* 132, 191–198.
- Bazylinski, D.A., Frankel, R.B., 2003. Biologically controlled mineralization in prokaryotes. In: Dove, P.M., De Yoreo, J.J., Weiner, S. (Eds.), *Biomineralization. Reviews in Mineralogy*, vol. 54. Mineralogical Society of America, Washington, D.C., pp. 95–114.
- Bazylinski, D.A., Frankel, R.B., 2004. Magnetosome formation in prokaryotes. *Nature Rev. Microbiol.* 2, 217–230.
- Bazylinski, D.A., Dean, A.J., Williams, T.J., Long, L.K., Middleton, S.L., Dubbels, B.L., 2004. Chemolithoautotrophy in the marine, magnetotactic bacterial strains MV-1 and MV-2. *Arch. Microbiol.* 182, 373–387.
- Blakemore, R.P., 1975. Magnetotactic bacteria. *Science* 190, 377–379.
- Blakemore, R.P., 1982. Magnetotactic bacteria. *Annu. Rev. Microbiol.* 36, 217–238.
- Blakemore, R.P., Short, K.A., Bazylinski, D.A., Rosenblatt, C., Frankel, R.B., 1985. Microaerobic conditions are required for magnetite synthesis within *Aquaspirillum magnetotacticum*. *Geomicrobiol. J.* 4, 53–71.
- Brice-Profera, S., Arrio, M.-A., Tronc, E., Letard, I., Cartier dit Moulin, C., Sainctavit, P., 2005. XMCD investigation of spin disorder in γ -Fe $_2$ O $_3$ nanoparticles at the Fe $L_{2,3}$ edges. *Phys. Scr.* T115, 626–628.
- Butler, R.F., Banerjee, S.K., 1975. Theoretical single-domain size range in magnetite and titanomagnetite. *J. Geophys. Res.* 80, 4049–4058.
- Carvalho, C., Sainctavit, P., Arrio, M.-A., Menguy, N., Wang, Y., Ona-Nguema, G., Brice-Profera, S., 2008. Biogenic vs. abiogenic magnetite nanoparticles: a XMCD study. *Am. Mineral.* 93, 880–885.
- Chang, S.-B., Stolz, J.F., Kirschvink, J.L., Awaramik, S.M., 1989. Biogenic magnetite in stromatolites. II. Occurrence in ancient sedimentary environments. *Precambrian Res.* 43, 305–315.
- Chen, J., Huang, D.J., Tanaka, A., Chang, C.F., Chung, S.C., Wu, W.B., Chen, C.T., 2004. Magnetic circular dichroism in Fe 2p resonant photoemission of magnetite. *Phys. Rev. B* 69 085107/1-8.
- Coker, V.S., Pearce, C.I., Lang, C., van der Laan, G., Patrick, R.A.D., Telling, N.D., Schüller, D., Arenholz, E., Lloyd, J., 2007. Cation site occupancy of biogenic magnetite compared to polygenic ferrite spinels determined by X-ray magnetic circular dichroism. *Eur. J. Mineral.* 19, 707–716.
- Coker, V.S., Telling, N.D., van der Laan, G., Patrick, R.A.D., Pearce, C.I., Arenholz, E., Tuna, F., Wimpenny, R., Lloyd, J.R., 2009. Harnessing the extracellular bacterial production of nanoscale cobalt ferrite with exploitable magnetic properties. *ACS Nano* 3, 1922–1928.
- de Castro, A.R.B., Fonseca, P.T., Pacheco, J.G., da Silva, J.C.V., da Silva, E.G.L., Santana, M.H.A., 2001. L-edge inner shell spectroscopy of nanostructured Fe $_3$ O $_4$. *J. Magn. Mater.* 233, 69–73.
- Dean, A.J., Bazylinski, D.A., 1999. Genome analysis of several magnetotactic bacterial strains using pulsed-field gel electrophoresis. *Curr. Microbiol.* 39, 219–225.
- Devouard, B., Pósfai, M., Hua, X., Bazylinski, D.A., Frankel, R.B., Buseck, P.R., 1998. Magnetite from magnetotactic bacteria size distributions and twinning. *Am. Mineral.* 83, 1387–1399.
- Dubbels, B.L., Dispirito, A.A., Morton, J.D., Semrau, J.D., Neto, J.N.E., Bazylinski, D.A., 2004. Evidence for a copper-dependent iron transport system in the marine, magnetotactic bacterium strain MV-1. *Microbiology* 150, 2931–2945.
- Dunin-Borkowski, R.E., McCartney, M.R., Frankel, R.B., Bazylinski, D.A., Pósfai, M., Buseck, P.R., 1998. Magnetic microstructure of magnetotactic bacteria by electron holography. *Science* 282, 1868–1870.
- Dunlop, D.J., 1973. Superparamagnetic and single-domain threshold sizes in magnetite. *J. Geophys. Res.* Solid Earth 78, 1780–1793.
- Egli, R., 2004. Characterization of individual rock magnetic components by analysis of remanence curves. 1. Unmixing natural sediments. *Stud. Geophys. Geod.* 48, 391–446.
- Frankel, R.B., Blakemore, R.P., 1980. Navigational compass in magnetic bacteria. *J. Magn. Mater.* 15–18, 1562–1564.
- Frankel, R.B., Blakemore, R.P., Wolfe, R.S., 1979. Magnetite in freshwater magnetic bacteria. *Science* 203, 1355–1357.
- Goering, E., Gold, S., Lafkoti, M., Schütz, G., 2006. Vanishing Fe 3d orbital moments in single-crystalline magnetite. *Europhys. Lett.* 73, 97–103.
- Goering, E.J., Lafkoti, M., Gold, S., Scheutz, G., 2007. Absorption spectroscopy and XMCD at the Verwey transition of Fe $_3$ O $_4$. *J. Magn. Mater.* 310, e249–e251.
- Heywood, B.R., Bazylinski, D.A., Garratt-Reed, A.J., Mann, S., Frankel, R.B., 1991. Controlled biosynthesis of greigite (Fe $_3$ S $_4$) in magnetotactic bacteria. *Naturwissenschaften* 77, 536–538.
- Hitchcock, A.P., Morin, C., Zhang, X., Araki, T., Dynes, J.J., Stover, H., Brash, J.L., Lawrence, J.R., Leppard, G.G., 2005. Soft X-ray spectromicroscopy of biological and synthetic polymer systems. *J. Electron Spectrosc.* 144–147, 259–269.
- Howells, M., Jacobsen, C., Warwick, T., 2007. Principles and applications of zone plate X-ray microscopes. In: Hawkes, P.W., Spence, J.C.H. (Eds.), *Science of Microscopy*. Springer, NY.
- Huang, D.J., Chang, C.F., Jeng, H.-T., Guo, G.Y., Lin, H.-J., Wu, W.B., Ku, H.C., Fujimori, A., Takahashi, Y., Chen, C.T., 2004. Spin and orbital magnetic moments of Fe $_3$ O $_4$. *Phys. Rev. Lett.* 93 077204/1-4.
- Jacobsen, C., Wirrick, S., Flynn, G., Zimba, C., 2000. Soft X-ray microscopy from image sequences with sub-100 nm spatial resolution. *J. Microsc.* 197, 173–184.
- Johansson, G.A., Tylliszczak, T., Mitchell, G.E., Keefe, M., Hitchcock, A.P., 2007. Three dimensional chemical mapping by scanning transmission X-ray spectromicroscopy. *J. Synchrotron Radiat.* 14, 395–402.
- Kaznatcheev, K.V., Karunakaran, C., Lanke, U.D., Urquhart, S.G., Obst, M., Hitchcock, A.P., 2007. Soft X-ray spectromicroscopy beamline at the CLS commissioning results. *Nucl. Instrum. Methods A* 582, 96–99.
- Keim, C.N., Lins, U., Farina, M., 2009. Manganese in biogenic magnetite crystals from magnetotactic bacteria. *FEMS Microbiol. Lett.* 292, 250–253.
- Kilcoyne, A.L.D., Tylliszczak, T., Steele, W.F., Fakra, S., Hitchcock, P., Franck, K., Anderson, E., Harteneck, B., Rightor, E.G., Mitchell, G.E., Hitchcock, A.P., Yang, L., Warwick, T., Ade, H., 2003. Interferometrically controlled scanning transmission microscopes at the advanced light source. *J. Synchrotron Radiat.* 10, 125–136.
- Kim, B.Y., Kodama, K.P., Moeller, R.E., 2005. Bacterial magnetite produced in water column dominates lake sediment mineral magnetism: Lake Ely, USA. *Geophys. J. Int.* 163, 26–37.
- Kirschvink, J.L., Lowenstam, H.A., 1979. Mineralization and magnetization of chiton teeth: paleomagnetic, sedimentologic, and biologic implications of organic magnetite. *Earth Planet. Sci. Lett.* 44, 193–204.
- Komeili, A., Vali, H., Beveridge, T.J., Newman, D.K., 2004. Magnetosome vesicles are present before magnetite formation, and MamA is required for their activation. *Proc. Natl. Acad. Sci. U.S.A.* 101, 3839–3844.
- Komeili, A., Li, Z., Newman, D.K., Jensen, G.J., 2006. Magnetosomes are cell membrane invaginations organized by the actin-like protein MamK. *Science* 311, 242–245.
- Kuiper, P., Searle, B.G., Duda, L.-C., Wolf, R.M., van der Zaag, P.J., 1997. Fe $L_{2,3}$ linear and circular magnetic dichroism of Fe $_3$ O $_4$. *J. Electron Spectrosc.* 86, 107–113.
- Kundu, S., Kale, A.A., Banpurkar, A.G., Kulkarni, G.R., Ogale, S.B., 2009. On the change in bacterial size and magnetosome features for *Magnetospirillum magnetotacticum* (MS-1) under high concentrations of zinc and nickel. *Biomaterials* 30, 4211–4218.
- Lee, Y., Lee, J., Bae, C.J., Park, J.-G., Noh, H.-J., Park, J.-H., Hyeon, T., 2005. Large-scale synthesis of uniform and crystalline magnetite nanoparticles using reverse micelles as nanoreactors under reflux conditions. *Adv. Funct. Mater.* 15, 503–509.
- Letard, I., Sainctavit, P., Menguy, N., Valet, J.-P., Isambert, A., Dekkers, M., Gloter, A., 2005. Mineralogy of greigite Fe $_3$ S $_4$. *Phys. Scr.* T115, 489–491.
- Lins, U., McCartney, M.R., Farina, M., Buseck, P.R., Frankel, R.B., 2005. Crystal habits and magnetic microstructures of magnetosomes in coccoid magnetotactic bacteria. *Appl. Environ. Microbiol.* 71, 4902–4905.
- Martel, S., Mohammadi, M., Felfoul, O., Lu, Z., Pouponneau, P., 2009. Flagellated magnetotactic bacteria as controlled MRI-trackable propulsion and steering systems for medical nanorobots operating in the human microvasculature. *Int. J. Robot. Res.* 28, 571–582.
- McCartney, M.R., Lins, U., Farina, M., Buseck, P.R., Frankel, R.B., 2001. Magnetic microstructure of bacterial magnetite by electron holography. *Eur. J. Mineral.* 13, 685–689.
- Morrall, P., Schedin, F., Case, G.S., Thomas, M.F., Dudzik, E., van der Laan, G., Thornton, G., 2003. Stoichiometry of Fe $_3-x$ O $_4$ (111) ultrathin films on Pt(111). *Phys. Rev. B* 67 214408/1-7.
- Moskowitz, B.M., Frankel, R.B., Bazylinski, D.A., 1993. Rock magnetic criteria for the detection of biogenic magnetite. *Earth Planet. Sci. Lett.* 120, 283–300.
- Muxworthy, A.R., Williams, W., 2006. Critical single-domain/multidomain grain sizes in noninteracting and interacting elongated magnetite particles: implications for magnetosomes. *J. Geophys. Res.* 111, B12512.
- Oldfield, F., 2007. Sources of fine-grained magnetic minerals in sediments: a problem revisited. *Holocene* 17, 1265–1271.
- Patrick, R.A.D., van der Laan, G., Henderson, C.M.B., Kuiper, P., Dudzik, E., Vaughan, D.J., 2002. Cation site occupancy in spinel ferrites studied by X-ray magnetic circular dichroism developing a method for mineralogists. *Eur. J. Mineral.* 14, 1095–1102.
- Pearce, C.I., Henderson, C.M.B., Patrick, R.A.D., van der Laan, G., Vaughan, D.J., 2006. Direct determination of cation site occupancies in natural ferrite spinels by $L_{2,3}$ X-ray absorption spectroscopy and X-ray magnetic circular dichroism. *Am. Mineral.* 91, 880–893.
- Petersen, N., von Döbenek, T., Vali, H., 1986. Fossil bacterial magnetite in deep-sea sediments from the South Atlantic Ocean. *Nature* 320, 611–615.
- Prozorov, T., Mallapragada, S.K., Narasimhan, B., Wang, L., Palo, P., Nilsen-Hamilton, M., Williams, T.J., Bazylinski, D.A., Prozorov, R., Canfield, P.C., 2007. Protein-mediated synthesis of uniform superparamagnetic magnetite nanocrystals. *Adv. Funct. Mater.* 17, 951–957.
- Scheffel, A., Gruska, M., Faivre, D., Linaoudis, A., Plitzko, J.M., Schüller, D., 2006. An acidic protein aligns magnetosomes along a filamentous structure in magnetotactic bacteria. *Nature* 440, 110–114.

- Schuler, D., Baeuerlein, E., 1998. Dynamics of iron uptake and Fe_3O_4 biomineralization during aerobic and microaerobic growth of *Magnetospirillum gryphiswaldense*. *J. Bacteriol.* 180, 159–162.
- Sette, F., Chen, C.T., Ma, Y., Modesti, S., Smith, N.V., 1990. Magnetic circular dichroism studies with soft X-rays. *AIP Conf. Proc.* 215, 787–795.
- Simpson, E.T., Kasama, T., Posfai, M., Buseck, P.R., Harrison, R.J., Dunin-Borkowski, R.E., 2005. Magnetic induction mapping of magnetite chains in magnetotactic bacteria at room temperature and close to the Verwey transition using electron holography. *J. Phys. Conf. Ser.* 17, 108–121.
- Song, H.-P., Li, X.-G., Sun, J.-S., Xu, S.-M., Han, X., 2008. Application of a magnetotactic bacterium, *Stenotrophomonas* sp. to the removal of Au(III) from contaminated wastewater with a magnetic separator. *Chemosphere* 72, 616–621.
- Staniland, S., Ward, B., Harrison, B.A., van der Laan, G., Telling, N., 2007. Rapid magnetosome formation shown by real-time X-ray magnetic circular dichroism. *Proc. Natl. Acad. Sci. U.S.A.* 104, 19524–19528.
- Staniland, S., Williams, W., Telling, N., van der Laan, G., Harrison, A., Ward, B., 2008. Controlled cobalt doping of magnetosomes in vivo. *Nat. Nanotechnol.* 3, 158–162.
- Stöhr, J., 1999. Exploring the microscopic origin of magnetic anisotropies with X-ray magnetic circular dichroism (XMCD) spectroscopy. *J. Magn. Mater.* 200, 470–497.
- Thomas-Keprta, K.L., Clemett, S.J., Bazylinski, D.A., Kirschvink, J.L., McKay, D.S., Wentworth, S.J., Vali, H., Gibson Jr., E.K., Romanek, C.S., 2002. Magnetofossils from ancient Mars: a robust biosignature in the Martian meteorite ALH84001. *Appl. Environ. Microbiol.* 68, 3663–3672.
- Weiss, B.P., Kim, S.S., Kirschvink, J.L., Kopp, R.E., Sankaran, M., Kobayashi, A., Komeili, A., 2004. Ferromagnetic resonance and low-temperature magnetic tests for biogenic magnetite. *Earth Planet. Sci. Lett.* 224, 73–89.
- Yamasaki, A., Kobori, H., Osawa, H., Nakamura, T., Sugimura, A., 2009. Soft X-ray magnetic circular dichroism study of magnetite nanoparticles. *J. Phys. Conf. Ser.* 150 042235/1–4.

Chapter 5

ADDITIONAL STUDIES

This section describes other studies on MTB samples that were undertaken concurrently with STXM-XMCD studies. These include: improvements to the STXM data acquisition process allowing for measurement of much higher quality XMCD data, Fe 2p spectromicroscopy studies on MTB cytoplasm, and biochemical NEXAFS studies of MTB performed at C 1s and O 1s edges.

5.1 Improved XMCD using XMCD-scanning

As mentioned in section 3.2.3.3, there are two methods with which XMCD stacks may be measured – single polarization mode or alternating polarization mode. Prior to August 2009, all XMCD stacks were measured sequentially at a single circular polarization before switching to the other circular polarization. With this acquisition method, one of the biggest challenges is the inability to fully align and correct for image distortions which vary over time between the LCP and RCP stacks. Although variations in beam intensity between the two stacks can be corrected, data processing of such stacks requires a lot of time. An important factor contributing to variations in the signal is carbon buildup, which can greatly modify the absorbance of the second acquired stack.

The XMCD-scanning (alternating polarization) mode was implemented during 2009 through the efforts of CLS staff as well as those of Dr. Tolek Tyliczszak, the developer of the STXM control program. XMCD-scanning involves switching between left and right circular polarizations at each photon energy. This acquisition method has much less distortion from sample drifts and variations in the beam intensity. This method greatly reduces data artifacts, which greatly improves the quality of XMCD data and allows the data to be processed much more easily and rapidly. Figure 5.1 shows a cartoon of the differences in the EPU phase changes, as well as the respective LCP and RCP spectra of MV-1 magnetosomes in the acquisition of XMCD stacks, before and after August 2009.

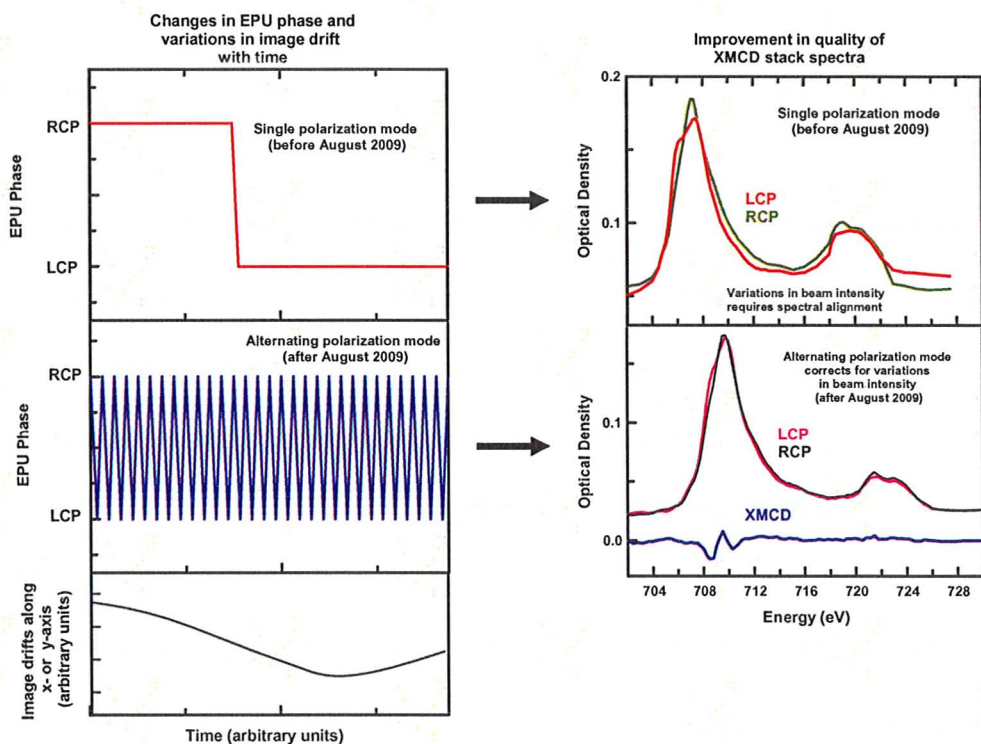


Figure 5.1 – Comparison of EPU-phase changes (left) and the resulting acquired LCP/RCP spectra (right) before and after August 2009.

5.2 Fe in cytoplasm of MV-1

In addition to observing Fe signal on the magnetosomes, Fe $2p$ signal was also observed in the cytoplasm surrounding the magnetosomes. Weak hints of this signal were observed throughout our investigations of MV-1, yet it was only confirmed in the latter portion of the studies. The observation of the presence of Fe in the cytoplasm around the magnetosomes, which has not yet been reported in literature, is a significant piece of evidence that can help to uncover the mechanisms of the biomineralization process in MTBs. Figure 5.2 (inset) shows the region (in red) around MV-1 magnetosomes, in which the Fe signal is detected. Figure 5.2 (a) plots a non-rescaled overlay of the magnetosome and cytoplasm spectra, which reveals that the optical density of the cytoplasm is less than that of the magnetosomes by roughly a factor of 10. Measuring the spectra at both left and right circular polarizations of this region does not reveal any XMCD as shown in Figure 2.5 (b), yet the spectral signature strongly corresponds to that of Fe (Figure 5.2 (c)), which is confirmation of the presence of Fe in the cytoplasm.

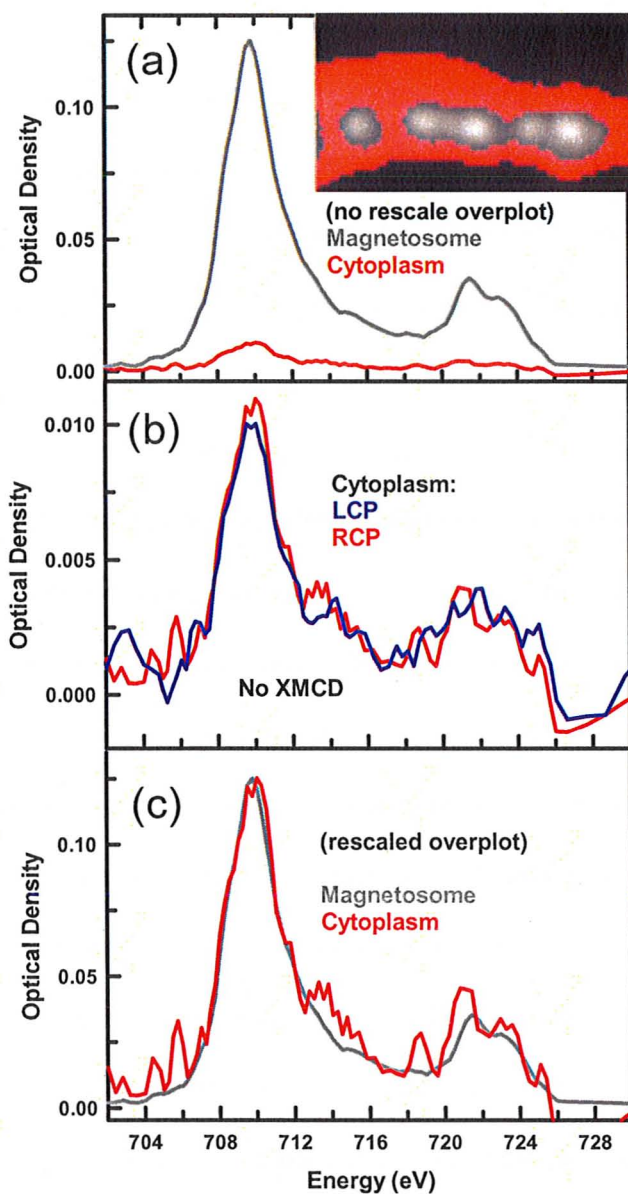


Figure 5.2 – (a) A non-rescaled overplot of the magnetosomal and cytoplasmic spectra; (inset) the region of interest (in red) surrounding magnetosomes from which the cytoplasmic spectrum is obtained; (b) cytoplasmic spectra measured at both polarizations reveal no XMCD; (c) a rescaled overlay of the cytoplasmic and magnetosome spectra confirms the presence of Fe in the cytoplasm.

5.3 Biochemical studies by C-N-O NEXAFS

In order to provide biological significance and context to our measurements of the magnetosome XMCD signal, it is important to do follow-up investigations at other biologically-pertinent edges, such as C1s, N1s and O1s. So far, measurements at the C1s and O1s absorption edges have been made on the various samples of MTBs studied. Typically, measurements at these edges were shown to be dominated by a strong protein signal, followed by lesser contributions from the sugar and lipid signals, as seen in Figure 5.3. The C1s and O1s spectra of MV-1 are a sum of various protein, saccharide and lipid component signals. The contribution of each component can be determined by using spectral and spectromicroscopy fitting procedures.

Furthermore, regions with different chemical compositions may be investigated by comparison of the respective extracted spectra (Figure 5.4) or by chemical mapping (Figure 5.5). Quantitative chemical mapping provides spatial distributions of multiple chemical components by fitting the image sequences (“stacks”) to the reference model spectra of different chemical species using singular value decomposition (SVD) (Hitchcock *et al.*, 2005; Koprinarov *et al.*, 2002). The amounts of each component at a given pixel are given by the fit coefficient for that component and thus, the array of those fit coefficients is a component map. Three such maps from a given image sequence can be converted to an RGB colour-coded composition map, which provides the true thickness of

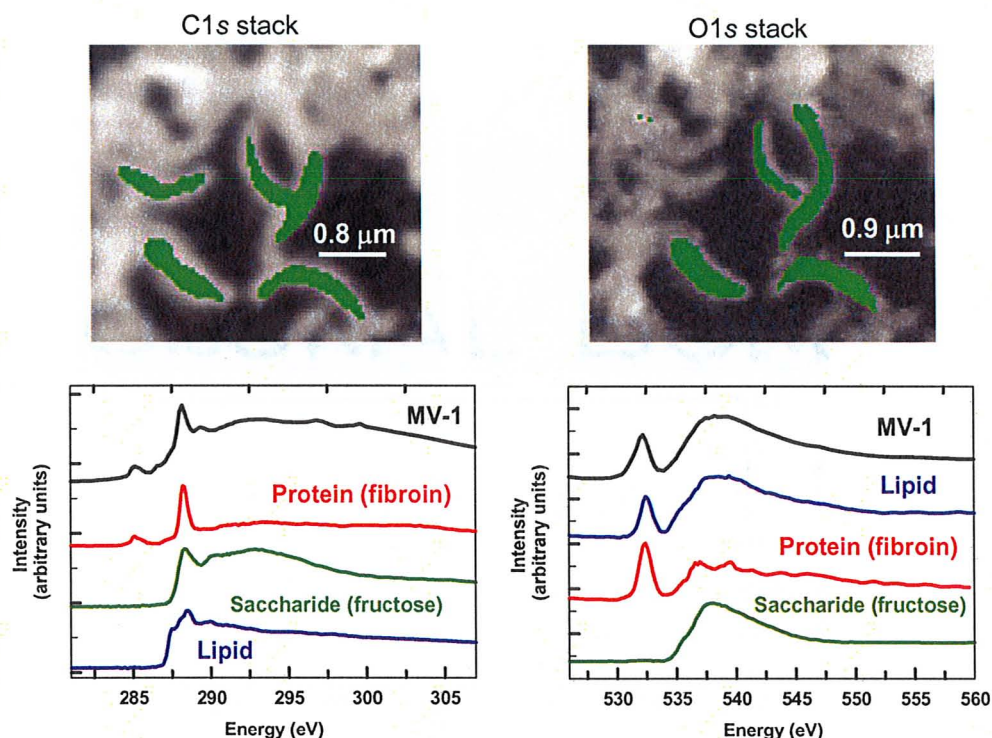


Figure 5.3 – Spectra of MV-1 measured at the C1s and O1s edges, compared against reference spectra of various biological components, such as protein, saccharide and lipid. Regions from which the MV-1 spectra are extracted are highlighted in green in the respective images located above the spectral overplots.

each of the components involved if the reference spectra are quantitative. To assess the overall quality of the spectral fit, the residual signal is generated by taking the difference between the data and the fit, averaged over the energy range of the image sequence. Elemental component maps may be generated more simply by taking the difference of two images taken respectively above and below the absorption edge of the component, as seen earlier in Section 3.3.2 with Fe

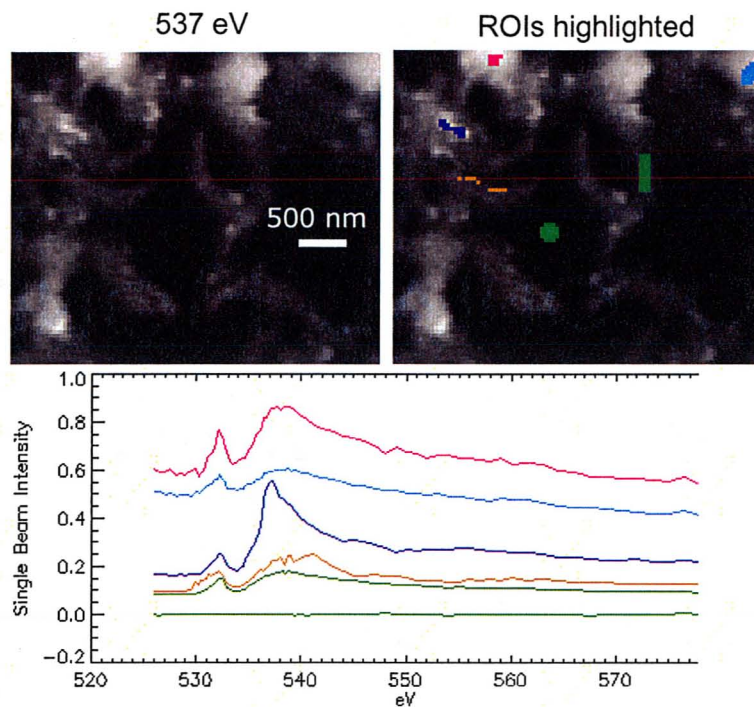


Figure 5.4 – Spectral comparison (using Zimba) of various components present in the MV-1 sample, with the respective regions of interest highlighted in the image on the top-right.

maps. The RGB component map on the right-hand side of Figure 5.5 reveals the presence of an unidentified component.

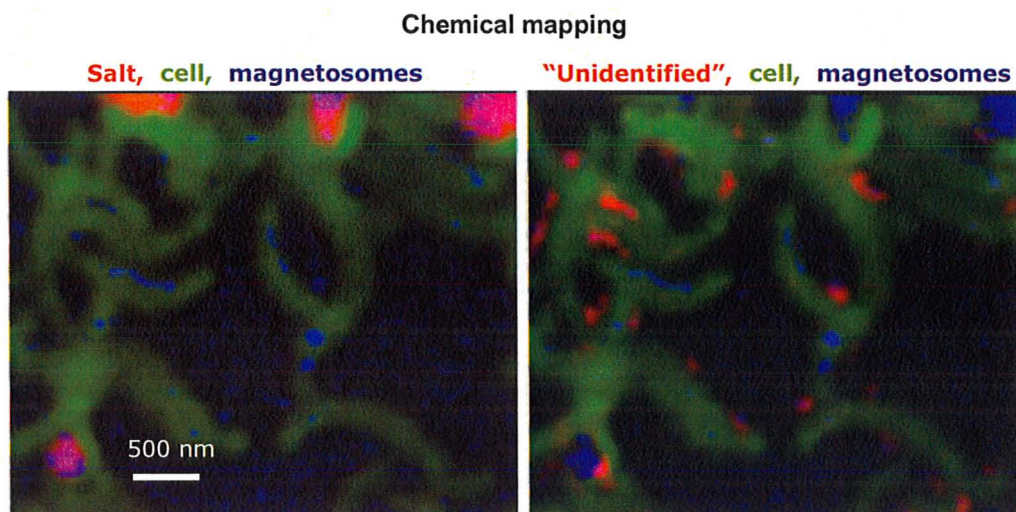


Figure 5.5 – Three-component RGB mapping allows for visual differentiation of different chemical components present in the sample. Image on the right reveals the presence of an unidentified component (in red).

Chapter 6

SUMMARY & FUTURE WORK

This chapter concludes the thesis by providing a brief summary of the work involved herein, as well as a short discussion of possible future directions, including the study of other MTB strains and the investigation of magnetosome anomalies.

6.1 Summary and significance of work

The work described in this thesis has shown, for the first time, that x-ray magnetic circular dichroism signal from individual magnetosomes in a magnetotactic bacterium (strain MV-1) can be measured using scanning transmission x-ray microscopy. Other XMCD studies of magnetosomes reported to date have involved non-spatially resolved studies of ensemble of MTBs or extracted magnetosomes. In this work, the magnetosomes were non-isolated and were studied while in their native state within unfixed and intact magnetotactic bacterial whole cells. Furthermore, in contrast to the total electron yield mode of detection reported in literature for all measurements of magnetosome XMCD signal so far, this work has explored and demonstrated detection by transmission, which is less sensitive to possible surface artifacts.

This work showed that detection of XMCD of in-plane magnetic moments requires: 1) the sample to be tilted or rotated, and 2) selection of magnetosome chain(s) to be orthogonal to the axis of tilt/rotation. Other conclusions in regards to the magnetosome XMCD signal are that the magnetite spectra of the magnetosomes have an excess of Fe(II), which is consistent with previously published reports in literature of bulk biogenic magnetite (Coker *et al.*, 2007, 2009; Carvallo *et al.*, 2008), which suggest that the deviation is a result of the under-oxidation of Fe(II). Finally, a new finding that has not yet been published from our work is the detection of iron within the cytoplasm surrounding

magnetosomes. Further study of this signal may help elucidate the biomineralization mechanism, which involves pre-concentration of iron around the magnetosome membrane prior to the controlled precipitation of iron oxide or iron sulphide magnetosomes.

There is evidence that, in addition to magnetotactic bacteria, certain protocists and aquatic organisms also contain single-domain magnetite minerals, including chiton (Lowenstam 1962), yellowfin tuna (Walker *et al.*, 1984), Chinook salmon (Kirschvink *et al.*, 1985), and sockeye salmon (Walker *et al.*, 1988; Mann *et al.*, 1988). Biogenic magnetite is also present in certain higher organisms including bees (Gould *et al.*, 1978), homing pigeons (Walcott *et al.*, 1979), dolphins (Zoeger *et al.*, 1981), bats (Holland *et al.*, 2008) and humans (Kirschvink *et al.*, 1992), where it may function as a compass or magnetic field receptor (Kirschvink *et al.*, 2001) to aid in orientation, homing and/or foraging. Recent work by Mora *et al.* (2004) and Holland *et al.*, (2008) has confirmed the use of magnetite as a magnetoreceptor in the homing pigeon and the bat, respectively. Combining these findings with those of magnetosome and magnetotactic bacteria studies will someday lead to a global understanding of the relationship between the evolutionary origins and adaptive significance of a finely tuned sensory system involving magnetism in diverse organisms.

6.2 Future directions

6.2.1 Study of other MTB strains

The field of magnetotactic bacteria studies is still relatively young. Although much remains to be explored and learned about these exotic organisms, the next immediate steps that can be taken to continue the work of this thesis include measurement of XMCD on other less-studied MTB strains, including greigite and greigite-magnetite producers, and possibly even those MTBs reported in literature that are capable of producing Co-, Ni- and Mn-doped magnetosomes. As well, it would be of interest to compare the magnitude of XMCD signals across different MTB strains.

Preliminary STXM Fe $2p$ and O $1s$ measurements (found in Appendix 4) have recently been made on a sample of a non-isolated MTB strain prepared by Dr. Bazylinski and collected from a pond in Utah, which produce both magnetite (Fe_3O_4) and greigite (Fe_3S_4) magnetosomes within the same chain. In order to confirm the presence of sulphur content in magnetosomes and follow-up on these preliminary O $1s$ spectroscopic data, which so far show differentiation between the two magnetosome compositions, future work on this MTB could involve measurements at the S $1s$ edge, in addition to the measurement and comparison of XMCD signals of both magnetite and greigite magnetosomes. Also, biochemical mapping at other edges, including N $1s$, S $2s$ and S $2p$ edges, may be explored to visualize and compare the internal biology of different MTB strains.

Lastly, using the Q-Fit program, comparisons of the relative site occupancies in magnetite and greigite may be made between various strains. If differences are found, we can proceed with further inquiries to answer such questions as: How do differences in site occupancies between different MTB strains arise? What are the effects of these differences on the crystal structure?

6.2.2 Investigation of magnetosome anomalies

Other future studies of interest on MTBs could include a more detailed probing and investigation of possible magnetosome anomalies, some of which have been occasionally observed in the measurements involved in the course of this thesis work. For example, some of the STXM-XMCD measurements have revealed that the magnetic moments of magnetosome chains in MV-1 cells may not necessarily all be aligned in the same direction (Appendix 6). This is a rather significant observation since if the MV-1 cells are indeed *polar* MTBs – meaning that they preferentially swim in one direction along the magnetic field – the magnetic moments of the MV-1 cells in the sample should collectively all be aligned in the same direction.

Aside from observing bi-directional alignment of the polar MV-1 cells along a single axis, many examples from the data have also shown the presence of a minority population of MV-1 cells aligned orthogonally to those of the majority population. This is yet another observed contradiction (which is also worthy of

further investigation) to the well-established fact that the magnetic moment of magnetosomes is large enough to allow alignment of the MTBs with respect to the geomagnetic field. In one such example (Appendix 6), it is believed that an MV-1 cell is actually aligned orthogonal to the plane of the sample, such that the magnetosome chain in the STXM image appears to be in a circular formation (believed to be the result of the magnetosome chain oriented in a ‘corkscrew’ fashion such that its magnetic moment is pointing out-of-plane of the sample). In this case, it would be of great interest to determine the true magnitude of the unaltered XMCD in the magnetosome chain, measured using the conventional 90° sample configuration mount in STXM.

On the other hand, if the axis of the magnetosome chain in this particular MV-1 cell were actually lying in the sample plane, it would be even more striking to probe the XMCD signal of individual magnetosomes and then, characterize the angular-dependence of XMCD on the directionality of the individual magnetosome magnetic moments, which somehow managed to align themselves in a circle. Lastly, measurements of XMCD on seemingly under-developed magnetosomes and its comparison to those of mature magnetosomes would be of considerable relevance to understanding the biomineralization process in MTBs.

6.2.3 Outlook

The importance of magnetosome studies has only been recognized within the past decade after their potential to be used in various applications and technologies as nano-magnets were realized in diverse disciplines. The work performed here will open up novel areas of magnetosome research and innovative avenues of potential magnetosome applications. At the same time that new information on magnetosomes has been obtained, this project has witnessed tremendous growth and progress in the STXM instrumentation and its data acquisition capabilities, which continue to expand and evolve. Coupling the ever-evolving capabilities of STXM with the unexpected challenges and surprises of new samples, studies on magnetotactic bacteria promise to bring excitement, challenges and satisfaction to those curious enough to embark on such a journey of discovery for many years to come.

APPENDICES

A.1 Collection of MTB cells from Princess Point/Hamilton

Harbour

Several water-sediment samples had been collected from various locations along the Princess Point and Hamilton Harbour Waterfront trails for the collection of MTB cells. Since MTBs live in the aerobic/anaerobic interface of water environments, which is located within the first few centimeters of sediments in shallow waters, a turkey baster was used as a syringe to collect water and mud samples close to the anoxic sediments, filling approximately two-thirds of glass jars. The loosely-capped jars were left undisturbed at room temperature with magnetic stir bars positioned at the water-sediment interface outside of the jars. After a few days, a water sample near the position of the stir bar was collected from each jar and examined under a visible light microscope (VLM). The jars were sampled periodically for the presence of MTBs, however, in this case, none were found in any of the collected water samples.

A.2 Preparation of MTB Growth Medium: Liquid and

Semisolid Media

Requiring a chemically defined medium for their growth in pure culture, a sample of MTBs, strain MC-1, acquired from Arash Komeili (University of California, Berkeley), were attempted to be cultured in both liquid and agar growth media. The growth medium was prepared by following a recipe similar to the one described by Blakemore *et al.* (1979). The medium consisted of (per Liter of distilled water): 0.035g ascorbic acid, 0.07g sodium acetate, 0.10g sodium thiosulfate, 0.12g sodium nitrate, 0.37g succinic acid, 0.37g tartaric acid, 0.68g potassium phosphate monobasic and 5.0mL Wolfe's mineral solution (ATCC). The pH of the medium was adjusted to 6.9 with NaOH. To half of this medium, 3.5g of agar was added to prepare the semisolid (agar) growth medium. The two growth media were stirred and subsequently autoclaved while covered.

In the case of the semisolid (agar) growth medium, 5mL Wolfe's vitamin solution (ATCC) and 1mL 0.01 M ferric quinate solution were filter-sterilized and combined into the autoclaved agar medium through a sterile 0.2- μ m pore size filter unit. The ferric quinate solution was prepared by combining 0.045g of FeCl_3 and 0.019g of quinic acid with 10mL of distilled water. 10 mL of the medium were added to each of 10 sterilized agar plates. Prior to inoculation, the agar plates were let to stand overnight while being stored in a closed environment,

in which air was evacuated with He. Agar plates were inoculated under a N₂ atmosphere: with 50µL and 100µL of the MC-1 sample, and various water/sediment samples collected from Princess Point/Hamilton Harbour with magnetic separation. The inoculated agar plates were stored under N₂ atmosphere at room temperature.

In the case of the liquid medium, the autoclaved medium was let to stand overnight prior to the filter-sterilized addition of 5mL Wolfe's vitamin solution (ATCC) and 1mL 0.01 M ferric quinate solution (same as the one used above) through a sterile 0.2-µm pore size filter unit. Five mL of the medium were dispensed into each of 3 screw-capped culture tubes, which were then inoculated with 100µL, 500µL and 1mL, of the MC-1 sample, respectively. The tubes were stored in a closed environment maintained at 30°C and in which air was evacuated with He.

Unfortunately, in all of the above-mentioned attempts to culture MC-1, no cell culture or growth was observed in any of the liquid or agar growth media. Since MTBs are highly notorious for their difficulty to be grown in axenic culture, it is very likely that even a slight deviation from their optimal growth conditions could have prevented them from proliferating in the lab environment. For example, since MTBs require microaerobic conditions, specifically 5-6% O₂, for their growth (Blakemore *et al.*, 1979), it is possible that any oxygen concentrations outside of this narrow window could have inhibited their

reproduction. Since the environments, under which the growth media were stored or inoculated, were not monitored for exact O₂ concentrations, it is more than likely that the N₂- or He-filled atmospheres used here could have contained too little to no oxygen. Alternatively, one may also suspect that slight exposure of the MTBs to atmospheric concentrations of oxygen (20%) could have led to their cell death - specifically in the part of the procedure when the liquid media were inoculated in an open environment.

A.3 STXM Measurements on Multi-cellular Magnetotactic

Prokaryote (MMP)

The multi-cellular magnetotactic prokaryote (MMP) is characterized by a aggregation or colony of magnetotactic Gram-negative cells, which are all morphologically indistinct. The number of cells in a colony can vary anywhere from a dozen to 45 flagellated cells, with a diameter ranging from 4 to 9.5 μm, depending on the type, location and level of maturation (Keim *et al.*, 2004). Magnetosomes in MMPs are usually ferrimagnetic iron sulphide crystals of three possible types: the weakly magnetic greigite (cubic Fe₃S₄), and the non-magnetic mackinawite (tetragonal FeS) and cubic FeS (Pósfai *et al.*, 1998). In a cell, up to 50 magnetosomes may be found per cell and these are located near the periphery of the cell where they are arranged in planar arrays composed of two to five

chains (Winklhofer *et al.*, 2007). Existing as an organized cell colony, the MMP migrates with highly complex coordinated movement.

In contrast to those cells of other multicellular prokaryotes, such as cyanobacteria, the individual cells of MMPs are incapable of surviving unicellularly. The MMP samples analyzed by STXM (Figure A.1) were acquired and prepared by collaborators, Professors Ulysses Lins and Dennis Bazylinski, as described in Chapter 3.1. Measurements on the MMP at the C 1s and O 1s edges are compared to the spectra of the major biological components in Figure A.2. Although Fe 2p spectral data of MMPs had been measured by STXM within this project, the data will not be shown here since Fe 2p reference spectra for iron sulphide has not yet been acquired for the analysis, comparison and validation of data. Future work at the sulfur edge will be carried out on this sample, in addition to measurement of the XMCD signal in the greigite magnetosomes.

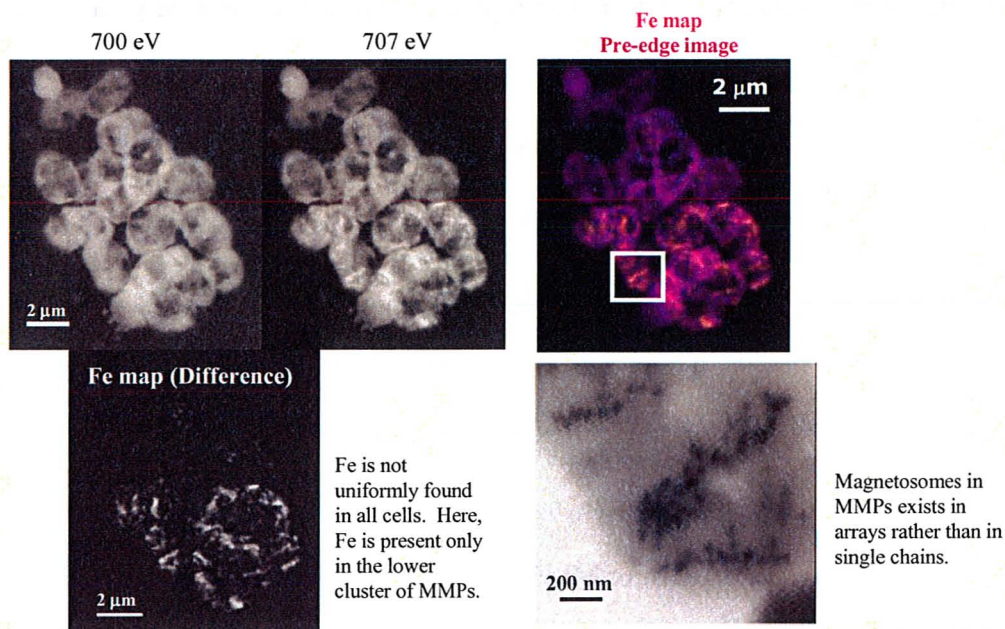


Figure A.1 –Fe maps of MMP show that the magnetosomes are arranged in multi-chain arrays, located near the periphery of the entire cell cluster.

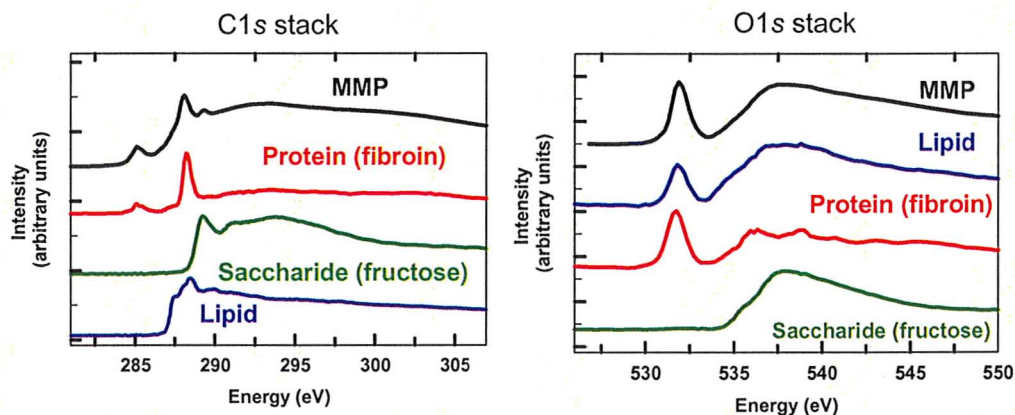


Figure A.2 – Spectra of MMP measured at the C1s and O1s edges, compared against reference spectra of various biological components, such as protein, saccharide and lipid.

A.4 Preliminary STXM Measurements on a Magnetite- and Greigite-Producing Magnetotactic Bacterium

A magnetotactic bacterium from Pettaquamscutt Estuary (Rhode Island) that produces magnetosomes of both magnetite and greigite compositions within the same chain of a cell was first reported by Bazylinski *et al* (1993b). Recently, a similar large rod-shaped MTB has been collected from a small pond in Utah by Bazylinski. Preliminary measurements (Figure A.3) on this sample by STXM confirm the presence of multiple magnetosome chains with irregularity in the morphology and arrangement of the magnetosome crystals – consistent with previous observations of magnetite and greigite possessing distinct morphologies (Bazylinski *et al.*, 1995). Future work on this sample includes measurements at the sulfur edge and comparison of the XMCD signals between magnetite and greigite at the Fe 2*p* edge.

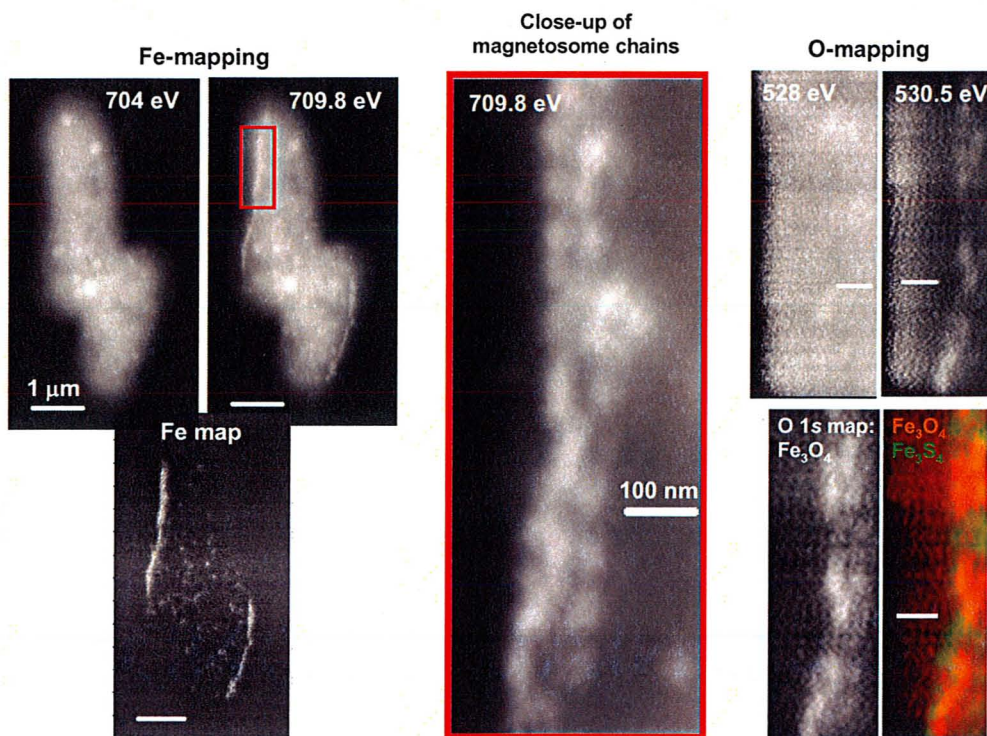


Figure A.3 – Left: Iron mapping on two overlapping cells of a magnetite- and greigite-producing MTB shows the proximity of the magnetosome chains to the cell wall. Centre: Zoomed-in image of the region highlighted in the red box (in image at left) shows irregularity in both the morphology and alignment of magnetosomes. Right: Oxygen mapping reveals differential composition of magnetosomes within the same chain, in which the absence of oxygen signal *implies* the presence of iron sulphide (greigite) magnetosomes (to be confirmed in future measurements), as opposed to iron oxide (magnetite).

A.5 Data Analysis using Q-Fit

Developed by Neil Telling (Daresbury Laboratory, Warrington, UK), Q-Fit is a software program that allows for the fitting of experimental magnetite spectra in order to determine cation site occupancies. The fitting is done via linear least-squares analysis using calculated spectra for each of the Fe sites. In this thesis, Q-Fit was merely used as a diagnostic and confirmatory tool to justify the observation of an unusually intense peak at the $\text{Fe}^{2+} \text{O}_h$ peak in the XMCD spectrum as being a result of under-oxidation of Fe^{2+} ions to the octahedral site. In stoichiometric magnetite, cation site occupancies are 1:1:1 in the $\text{Fe}^{2+} \text{O}_h$, $\text{Fe}^{3+} \text{T}_d$, $\text{Fe}^{3+} \text{O}_h$ sites, respectively.

In the case of the published MV-1 magnetosome spectra, the cation site occupancies were found to be 1.80 : 0.85 : 0.16 (± 0.005), which shows a huge excess and deficiency of $\text{Fe}^{2+} \text{O}_h$ and $\text{Fe}^{3+} \text{O}_h$, respectively. However, in more recent MV-1 data (September 2009), the cation site occupancies have been found to be closer to stoichiometric magnetite such that the values are 1.54 : 0.94 : 1.09 (± 0.005). Since no investigation has been conducted in this thesis to determine the range of differences in the occupancy ratios between individual magnetosomes or between single cells, no conclusion can be reached regarding the discrepancies in the ratios. As a result, these findings call for a more rigorous use of Q-Fit in future work, especially in the quantitative comparison of

magnetosome spectra between magnetosomes within the same chain, between cells within the same sample and possibly even between different MTB strains.

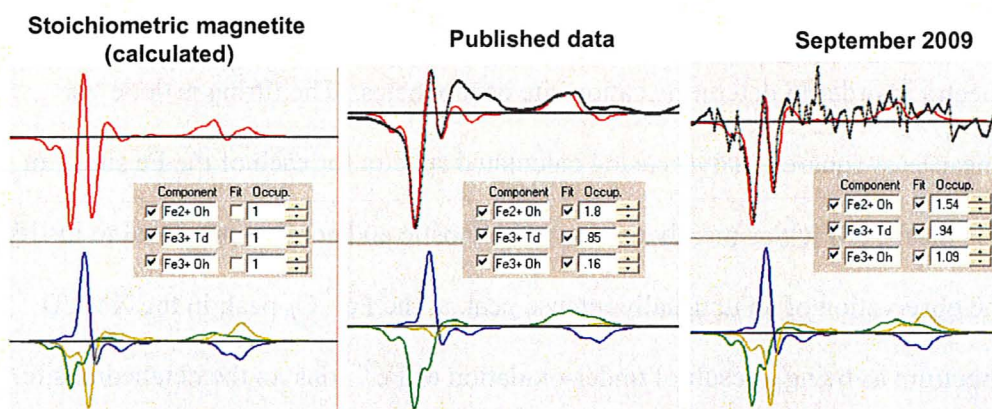


Figure A.4 – Examples of spectral fitting of magnetosome (magnetite) spectra using Q-Fit. Left: Calculated spectrum of stoichiometric magnetite (1:1:1); Centre: Fitting of the published MV-1 data reveals an excess and deficiency of Fe²⁺ O_h and Fe³⁺ O_h, respectively; Right: Fitting of recent data on MV-1 shows that the occupancy ratios are closer to stoichiometry.

A.6 Magnetosome Anomalies

As MV-1 is a polar MTB, the finding of two MV-1 cells pointing in opposite directions in recent measurements is rather surprising. The following figures reveal opposite directionality in the magnetic moments of two overlapping MV-1 cells in: 1) the spectra of entire magnetosome chains (Figure A.5), of individual magnetosomes (Figure A.6) and in XMCD images (Figure A.7), which show inversion of signal at each of the peak energies in the XMCD spectrum of magnetite. The reason for why this anomaly is observed is unknown, yet it could serve as a starting point for future MTB studies. Another notable anomaly observed among measurements is the presence of a circular arrangement of magnetosomes (Figure A.8). It is not known for sure whether the circular arrangement is a result of the cell pointing *perpendicularly* to the sample plane (TEM grid) or whether the cell is curled into a circle within the sample plane.

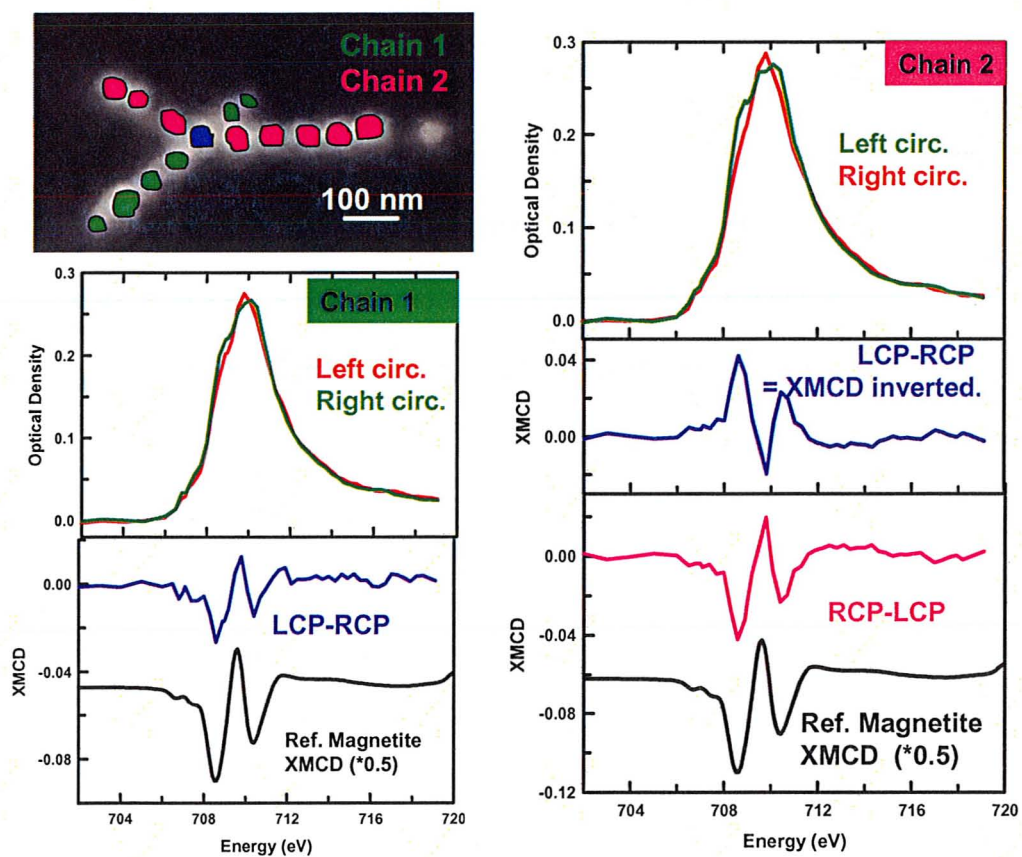


Figure A.5 – XMCD spectra measured for two overlapping magnetosome chains of distinct cells reveal opposing magnetic dipoles.

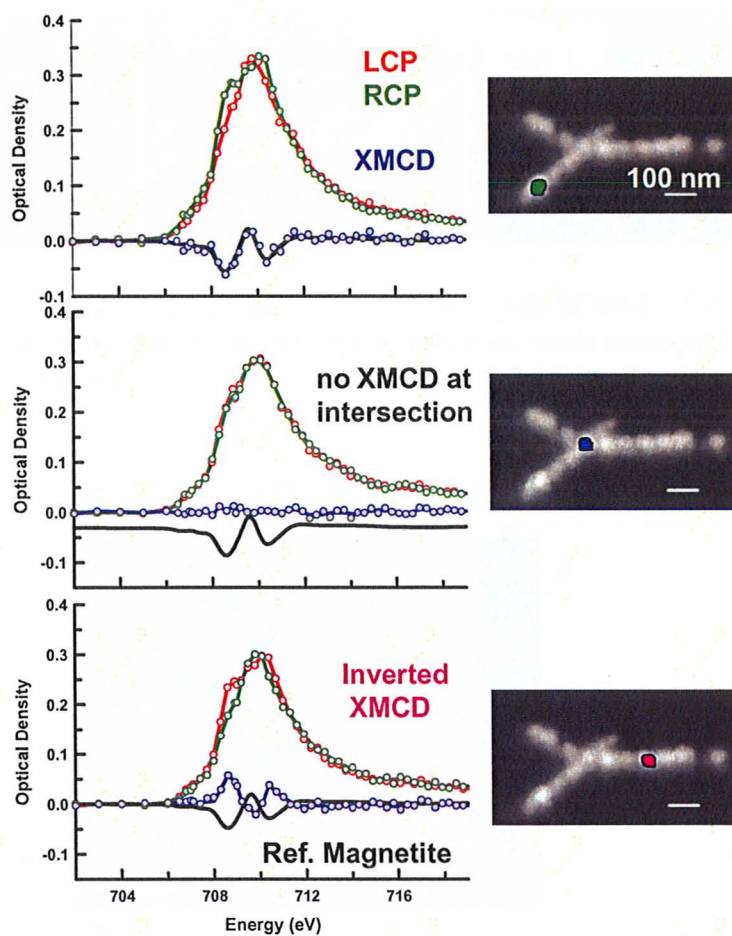


Figure A.6 – Opposing directionality in the magnetic moments of overlapping magnetosome chains is strongly evident from the measurement of XMCD in individual magnetosomes.

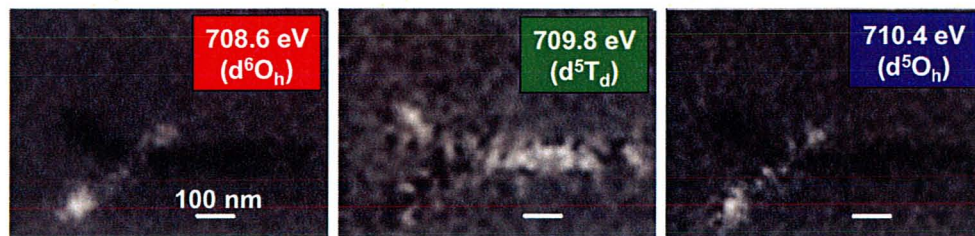


Figure A.7 – XMCD images at each of the peak energies in the magnetite XMCD spectrum show inversion of signal between the two magnetosome chains – a clear visualization of opposite orientation of magnetic dipoles.

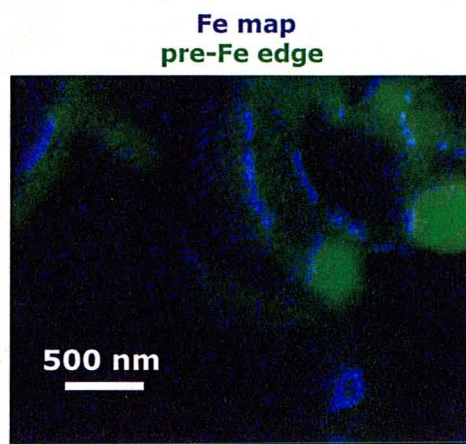


Figure A.8 – An interesting magnetosome anomaly – a circular arrangement of magnetosomes is observed in the lower portion of the STXM image above. It is not known whether the magnetosome chain is lying within the sample plane or is spiraling out of the sample plane.

REFERENCES

- * aXis2000 is written in Interactive Data Language (IDL) and developed by Chris Jacobsen, Carl Zimba, Adam Hitchcock and others. It is available free for non-commercial use from <http://unicorn.mcmaster.ca/aXis2000.html>.
Version used: March 2009.
- ** CTM4XAS is developed by Frank de Groot. It is available free for non-commercial use from:
<http://www.anorg.chem.uu.nl/people/staff/FrankdeGroot/SLS/ctm4xas2008.htm>
- *** Q-Fit is developed by Neil Telling (Daresbury Laboratory, Warrington, UK). The software was acquired through private communication. Version used: November 2009.
- Adamkiewicz, V.W., A. Authier, S. Dumont, S. Garzon, S. Leduc, D. Morency, N. Nakhostin and H. Strykowski (1991), *J. Microbiol. Meth.* 13, 255-258.
- Ade, H. and A.P. Hitchcock (2008), *Polymer* 49, 643-675.
- Altarelli, M. (1993), *Phys. Rev. B.*, 47, 597.
- Arakaki, A., H. Nakazawa, M. Nemoto, T. Mori and T. Matsunaga (2008), *J. R. Soc. Interface*, 5, 977-999.
- Arato, B., Z. Szanyi, C. Flies, D. Schüler, R.B. Frankel, P.R. Buseck and M. Pósfai (2005), *Am. Mineral.* 90, 1233-1241.
- Attwood, D. (1999), *Soft X-rays and Extreme Ultraviolet Radiation: Principles and Applications*, Cambridge University Press.
- Bahaj, A.S., I.W. Croudace, P.A.B. James, F.D. Moeschler and P.E. Warwick (1998), *J. Magn. Magn. Mater.*, 184, 241–244.
- Balkwill, D.L., D. Maratea and R.P. Blakemore (1980), *J. Bacteriol.* 141, 1399-1408. Bazylinski, D. A., A.J. Garratt-Reed, A. Abedi, and R.B. Frankel (1993a), *Arch. Microbiol.* 160, 35–42.
- Bazylinski D.A., B.R. Heywood, S. Mann, R.B. Frankel (1993b), *Nature*, 366, 218.

- Bazyliniski, D.A., A.J. Garratt-Reed and R.B. Frankel (1994), *Microsc. Res. Techniq.* *27*, 389-401.
- Bazyliniski, D.A., R.B. Frankel, B. R. Heywood, S. Mann, J.W. King, P.L. Donaghay, and A.K. Hanson (1995), *Appl. Environ. Microbiol.* *61*, 3232-3239.
- Bazyliniski, D.A., and R.B. Frankel (2003), *Rev. Mineral. Geochem.* *54*, 217-247.
- Bazyliniski, D.A. and R.B. Frankel (2004), *Nat. Rev. Microbiol.* *2*, 217–230.
- Bellini, S. (2009a), *Chin. J. Oceanol. Limnol.* *27*(1), 3-5.
- Bellini, S. (2009b), *Chin. J. Oceanol. Limnol.* *27*(1), 6-12.
- Blakemore, R.P. (1975), *Science*, *190*, 377-379.
- Blakemore, R.P. (1982), *Annu. Rev. Microbiol.*, *36*, 217-238.
- Blakemore, R.P., D. Maratea, and R.S. Wolfe (1979), *J. Bacteriol.* *140*(2), 720-729.
- Blakemore, R.P., R.B. Frankel and A.J. Kalmijin, (1980), *Nature*, *286*, 384-385.
- Brice-Profeta, S., M.-A. Arrio, E. Tronc, I. Letard, Ch. Cartier dit Moulin and P. Sainctavit (2005), *Phys. Scripta*, *T114*, 626-628.
- Burns, R.G. (1993), *Mineralogical applications of crystal field theory*, Cambridge University Press, Cambridge.
- Butler, R.F. and S.K. Banerjee (1975), *J. Geophys. Res.* *80*, 4049-4058.
- Cao, X., Y. Xie, F. Yu, Z. Yao and L. Li (2003), *J. Mater. Chem.* *13*, 893-896.
- Carra, P. B.T. Thole, M. Altarelli and X.-D. Wang (1993), *Phys. Rev. Lett.* *70*, 694-697.
- Carvalho, C., P. Sainctavit, M.-A. Arrio, N. Menguy, Y. Wang, G. Ona-Nguema and S. Brice-Profeta (2008), *Am. Mineral.* *93*, 880-885.

- Chang, S.-B. R. and J.L. Kirschvink, (1989) *Annu. Rev. Earth Planet. Sci.* 17, 169–195.
- Coker, V.S., A.G. Gault, C.I. Pearce, G. van der Laan, N.D. Telling, I.M Charnock, D.A. Polya and J.R. Lloyd (2006), *Environ. Sci. Technol.* 40, 7745-7750.
- Coker, V.S., C.I. Pearce, C. Lang, G. van der Laan, R.A.D. Patrick, N.D. Telling, D. Schüler, E. Arenholz and J. Lloyd (2007), *Eur. J. Mineral.* 19, 707-716.
- Coker, V.S., C.I. Pearce, R.A.D. Patrick, G. van der Laan, N.D. Telling, J.M. Charnock, E. Arenholz and J.R. Lloyd (2008), *Am. Mineral.* 93, 1119.
- Coker, V.S., N.D. Telling, G. van der Laan, R.A.D. Patrick, C.I. Pearce, E. Arenholz, F. Tuna, R.E.P. Winpenny and J.R. Lloyd (2009), *ACS Nano*, 3, 1922-1928.
- Cornell, R. M. and U. Schwertmann (2003), *The Iron Oxides: Structure, Properties, Reactions, Occurrences and Uses*, 2nd Edition, Wiley-VCH, Weinheim, Germany.
- Dahlberg, E.D., R.B. Proksch, B.M. Moskowitz, D.A. Bazylinski and R.B. Frankel (1995), *J. Magn. Magn. Mater.* 140-144, 1459-1461.
- de Groot, F. and A. Kotani (2008), *Core level spectroscopy of solids*, CRC Press.
- Devouard, B., M. Pósfai, X. Hua, D.A. Bazylinski, R.B. Frankel, R.B., and P.R. Buseck (1998), *Am. Mineral.* 83, 1387-1399.
- Donaghay, P.L., H. M. Rines, and J. M. Sieburth (1992), *Arch. Hydrobiol. Beih. Ergebn. Limnol.* 36, 96-108.
- Dunin-Borkowski, R.E., M.R. McCartney, R.B. Frankel, D.A. Bazylinski, M. Pósfai and P.R. Buseck (1998), *Science*, 282, 1868-1870.
- Dunlop, D.J. (1973), *J. Geophys. Res. Solid Earth*, 78, 1780-1793.
- Eimüller, T., P. Fischer, M. Köhler, M. Scholz, P. Guttman, G. Denbeaux, S. Glück, G. Bayreuther, G. Schmahl, D. Attwood and G. Schütz (2001), *Appl. Phys. A* 73, 697-701.

- Erskine, J.L. and E.A. Stern (1975), *Phys. Rev. B*, *12*, 5016-5024.
- Faivre, D., L. Böttger, B. Matzanke and D. Schüler (2007), *Angew. Chemie. Int. Edn.* *46*, 8647–8652.
- Faivre, D. and P. Zuddas (2006), *Earth. Planet. Sci. Lett.*, *243*, 53-60.
- Faivre, D. and D. Schüler (2008), *Chem. Rev.* *108*, 4875-4898.
- Farina, M., D. M. S. Esquivel and H. G. P. Lins de Barros (1990), *Nature*, *343*, 256-258.
- Fischer, P., T. Eimuller, R. Kalchgruber, G. Schutz, G. Schmahl, P. Guttmann and G. Bayreuther (1999), *J. Synchrotron Radiat.* *6*, 688-690.
- Fischer, H., G. Mastrogiacomo, J. F. Loffler, R. J. Warthmann, P. G. Weidler, and A. U. Gehring (2008), *Earth Planet. Sci. Lett.* *270*, 200-208.
- Frankel, R.B. (2009), *Chin. J. Oceanol. Limnol.* *27(1)*, 1-2.
- Frankel, R.B., R.P. Blakemore and R.S. Wolfe (1979), *Science*, *203*, 1355-1357.
- Frankel, R.B. and R.P. Blakemore (1980), *J. Magn. Magn. Mater.* *15-18*, 1562-1564.
- Frankel R.B., R.P. Blakemore, F.F. Torres de Araujo, D.M.S Esquivel, and J. Danon (1981), *Science*, *212*, 1269–1270.
- Frankel, R. B., D.A. Bazylinski, M. Johnson and B.L. Taylor (1997), *Biophys. J* *73*, 994–1000.
- Frankel, R.B. and D.A. Bazylinski (2004), *ASM News*, *70*, 176-183.
- Frankel, R. B., G.C. Papaefthymiou, R.P. Blakemore and W. O'Brien (1983), *Biochim. Biophys. Acta*, *763*, 147–159.
- Generalic, E. (27 Feb. 2010). Argon. *EniG. Periodic Table of the Elements*. KTF-Split. Accessed: 5 March 2010, from: <http://www.periodni.com/en/ar.html>
- Glasauer, S., P.G. Weidler, S. Langley and T.J. Beveridge (2003), *Geochim. Cosmochim. Acta*, *67(7)*, 1277-1288.

- Goering, E., S. Gold, M. Lafkioti and G. Schütz (2006), *Europhys. Lett.* 73, 97-103.
- Goering, E.J., M. Lafkioti, S. Gold and G. Schütz (2007), *J. Magn. Magn. Mater.* 310, e249 – e251.
- Golden, D. C., D.W. Ming, C.S. Schwandt, H.V. Lauer and R.A. Socki (2001), *Amer. Mineral.* 8, 370–375.
- Goodenough, J.B. and A.L. Loeb (1955), *Phys. Rev.* 98, 391-408.
- Gorby, Y.A., T. J. Beveridge and R. P. Blakemore (1988), *J. Bacteriol.* 170, 834-841.
- Gould, J.L., J.L. Kirschvink and K.S. Deffeyes (1978), *Science*, 201(4360), 1026-1028.
- Grunberg, K., C. Wawer, B. M. Tebo and D. Schuler (2001), *Appl. Environ. Microbiol.* 67, 4573-4582.
- Hanzlik, M., M. Winklhofer and N. Peterson (2002), *J. Magn. Magn. Mater.* 248, 258-267.
- Hitchcock, A.P., C. Morin, X. Zhang, T. Araki, J.J. Dynes, H. Stover, J.L. Brash, J.R. Lawrence and G.G Leppard (2005), *J. Electron Spectrosc. Relat. Phenom.* 144- 147, 259-269.
- Hoffman, V. (1992), *Phys. Earth Planet. Inter.* 70, 288–301.
- Holland, R.A., J.L. Kirschvink, T.G. Doak¹ and M. Wikelski¹ (2008), *PLoS ONE*, 3(2), e1676, 1-6.
- Jacobs, I.S. and C.P. Bean (1955), *Phys. Rev.* 100, 1060-1067.
- Johansson, G.A., T. Tyliczszak, G.E. Mitchell, M. Keefe and A.P. Hitchcock (2007), *J. Synchrotron Radiat.* 14, 395-402.
- Kalmijn, A.J. and R.P. Blakemore (1978), The Magnetic Behavior of Mud Bacteria. In: Schmidt-Koenig K, Keeton WT, eds. *Animal Migration, Navigation and Homing*. Berlin: Springer-Verlag. 354 p.

- Kaznatcheev, K.V., C. Karunakaran, U.D. Lanke, S.G. Urquhart, M. Obst and A.P. Hitchcock, (2007), Soft X-ray spectromicroscopy beamline at the CLS commissioning results. *Nucl. Instrum. Meth. A* 582, 96-99.
- Keim, C.N., F. Abreu, U. Lins, H.G.P. Lins de Barros and M. Farina (2004), *J. Struct. Biol.* 145, 254–262.
- Keim, C.N., U. Lins and M. Farina (2009), *FEMS Microbiol. Lett.* 292(2), 250-253.
- Kilcoyne, A.L.D., T. Tyliczszak, W.F. Steele, S. Fakra, P. Hitchcock, K. Franck, E. Anderson, B. Harteneck, E.G. Rightor, G.E. Mitchell, A.P. Hitchcock, L. Yang, T. Warwick and H. Ade (2003), *J. Synchrotron Rad.* 10, 125-136.
- Kim, B.Y, K.P. Kodama and R.E. Moeller (2005), *Geophys. J. Int.* 163, 26-37.
- Kirschvink, J.L. (1980): *J. Exp. Biol.* 86, 345-347.
- Kirschvink, J.L., and H.A. Lowenstam (1979), *Earth. Planet. Sci. Lett.* 44, 193-204.
- Kirschvink, J.L., M.M. Walker, S.–B. Chang, A.E. Dizon and K.A. Peterson (1985), *J. Comp. Physiol. A.*, 157, 375-381.
- Kirschvink, J.L., A. Kobayashi-Kirschvink, and B. J. Woodford (1992), *Proc. Nat. Acad. Sci.*, 89, 7683–7687.
- Kirschvink, J.L., M.M. Walker and C.E. Diebel (2001), *Curr. Opin. Neurobiol.* 11, 462–467.
- Kirz, J. and D.T. Attwood (1986), Center for X-ray Optics (CXRO), *X-Ray Data Booklet*, Lawrence Berkeley Lab, Rev. 1.
- Klein, C., C.S. Hurlbut Jr, and J.D. Dana (1999), *Manual of mineralogy*, 21st ed., Wiley, New York.
- Komeili, A., Z. Li, D.K. Newman and G.J. Jensen (2006), *Science*, 311, 242–245.
- Koprinarov, I.N., A.P. Hitchcock, C.T. McCrory and R.F. Childs (2002), *J. Phys. Chem. B.* 106, 5358-5364.

- Kuiper P., B.G. Searle, L.-C. Duda, R.M. Wolf, P.J. van der Zaag (1997), *J. Electron Spectrosc.* 86, 107-113.
- Kundu, S., A.A. Kale, A.G. Banpurkar, G.R. Kulkarni and S.B. Ogale (2009), *Biomaterials*, 30(25), 4211-4218.
- Lam, K.P., M. Obst, A.P. Hitchcock, J.J. Dynes, J.R. Lawrence, G.D.W. Swerhone, G.G. Leppard, D. Bazyliniski, D. Bertwistle, K. Kaznatcheev and C. Karunakaran (2008), *2007 CLS Activity Report*, 108-109.
- Lam, K.P., A.P. Hitchcock, M. Obst, J.R. Lawrence, G.D.W. Swerhone, G.G. Leppard, T. Tyliczszak, C. Karunakaran, J. Wang, K. Kaznatcheev, D.A. Bazyliniski and U. Lins (2010), *Chem. Geol.* 270, 110-116.
- Lang, C., D. Schüler and D. Faivre (2007), *Macromol. Biosci.* 7, 144-151.
- Lefever, R.A. in: Landolt-Börnstein III/12b, Springer, Berlin, 1980, p. 55.
- Letard, I., P. Saintavit, N. Menguy, J.-P. Valet, A. Isambert, M. Dekkers, and A. Gloter (2005), *Phys. Scripta*, T115, 489-491.
- Lovesey, S.W. and S.P. Collins (1996), *X-ray Scattering and Absorption by Magnetic Materials*, Oxford University Press Inc., New York.
- Lowenstam, H.A. (1962), *Geol. Soc. Am. Bul.* 73, 435-438.
- Lowenstam, H.A. (1981), *Science*, 211, 1126–1131.
- Mandernack, K.W., D.A. Bazyliniski, W.C. Shanks and T.D. Bullen (1999), *Science*, 285, 1892-1896.
- Mann, S., R.B. Frankel & R.P. Blakemore (1984), *Nature*, 310, 405–407.
- Mann, S., N.H.C. Sparks and R.P. Blakemore (1987a), *Proc. R. Soc. Lond. B Biol. Sci.* 231, 469–476.
- Mann, S., N.H.C. Sparks and R.P. Blakemore (1987b), *Proc. R. Soc. Lond. B Biol. Sci.* 231, 477–487.

- Mann, S., N.H.C. Sparks, M.M. Walker and J.L. Kirschvink (1988), *J. exp. Biol.* *140*, 35-49.
- Mann, S. and R.B. Frankel (1989), *Biomineralization: Chemical and Biochemical Perspectives*, eds. Mann, S., Webb, J. & Williams, R. J. P., VCH Publishers, New York, 389–426.
- Mann, S. N.H.C. Sparks, R. B. Frankel, D.A. Bazylinski and H.W. Jannasch (1990), *Nature*, *343*, 258-261.
- Martel, S., M. Mohammadi, O. Felfoul, Z. Lu and P. Pouponneau (2009), *Int. J. Robot. Res.* *28*, 571-582.
- Matsunaga, T., Y. Okamura and T. Tanaka (2004), *J. Mater. Chem.* *14*, 2099-2105.
- McCartney, M.R., U. Lins, M. Farina, P.R. Buseck and R.B. Frankel (2001), *Eur. J. Mineral.* *13*, 685-689.
- McKay, D. S., E.K. Gibson Jr., K.L. Thomas-Keprta, H. Vali, C.S. Romanek, S.J. Clemett, X.D.F. Chillier, C.R. Maechling and R.N. Zare (1996), *Science*, *273*, 924–930.
- Meldrum, F. C., B.R. Heywood, S. Mann, R.B. Frankel and D.A. Bazylinski (1993a), *Proc. R. Soc. Lond. B Biol. Sci.* *251*, 231–236.
- Meldrum, F. C., B.R. Heywood, S. Mann, R.B. Frankel & D.A. Bazylinski (1993b), *Proc. R. Soc. Lond. B Biol. Sci.* *251*, 237–242.
- Moench, T.T. and W.A. Konetzka (1978), *Arch. Microbiol.* *119*, 203-212.
- Mora, C.V., M. Davison, J.M. Wild and M.M. Walker (2004), *Nature*, *432*, 508-511.
- Morrall, P., F. Schedin, G.S. Case, M.F. Thomas, E. Dudzik, G. van der Laan, and G. Thornton (2003), *Phys. Rev. B* *67*, 214408-1/7.
- Moskowitz, B.M., R.B. Frankel and D.A. Bazylinski (1993), *Earth Planet. Sci. Lett.* *120*, 283-300.
- Muxworthy, A.R., and W. Williams (2006), *J. Geophys. Res.* *111*, B12S12.

- Nave, C.R. (2005), Circular Polarization. *Hyperphysics*. Accessed: 5 January 2010, from: <http://hyperphysics.phy-astr.gsu.edu/hbase/phyopt/polclas.html>
- Ofer, S., I. Nowik, E.R. Bauminger, G.C. Papaefthymiou, R.B. Frankel and R.P. Blakemore (1984), *Biophys. J.* 46, 57-64.
- Oldfield F. (2007), *Holocene*, 17, 1265-1271.
- Pankhurst, Q.A., J. Connolly, S.K. Jones and J. Dobson (2003), *J. Phys. D: Appl. Phys.* 36, R167-R181.
- Patrick, R.A.D., G. van der Laan, C.M.B. Henderson, P. Kuiper, E Dudzik and D.J. Vaughan (2002), *Eur. J. Mineral.* 14, 1095-1102.
- Pearce, C.I., Henderson, C.M.B., Patrick, R.A.D., van der Laan, G. and Vaughan, D.J. (2006), *Am. Mineral.* 91, 880-893.
- Penninga, I., H. deWaard, B.M. Moskowitz, D.A. Bazylinski and R.B. Frankel (1995), *J. Magn. Magn. Mater.* 149, 279–286.
- Petersen, N., T. von Döbeneck and H. Vali (1986), *Nature*, 320, 611-615.
- Pósfai, M., Buseck, P.R., Bazylinski, D.A., Frankel, R.B. (1998), *Science*, 280, 880–883.
- Proksch, R. B., T.E. Schäffer, B.M. Moskowitz, E.D. Dahlberg, D.A. Bazylinski and R.B. Frankel (1995), *Appl. Phys. Lett.* 66, 2582–2584.
- Prozorov, T., S.K. Mallapragada, B. Narasimhan, L. Wang, P. Palo, M. Nilsen-Hamilton, T.J. Williams, D.A. Bazylinski, R. Prozorov and P.C. Canfield (2007), *Adv. Funct. Mater.* 17, 951-957.
- Rightor, E.G., A.P. Hitchcock, H. Ade, R.D. Leapman, S.G. Urquhart, A.P. Smith, G. Mitchell, D. Fischer, H.J. Shin and T. Warwick (1997), *J. Phys. Chem. B* 101, 1950-1960.
- Rodgers, F. G., R.P. Blakemore, N.A. Blakemore, R.B. Frankel, D.A. Bazylinski, D. Maratea and C. Rodgers (1990), *Arch. Microbiol.* 154, 18–22.
- Rosenblatt, C., F. Flavio Torres de Araujo, and R.B. Frankel (1982b), *Biophys. J.* 40, 83- 85.

- Rosenblatt, C., F. Flavio Torres de Araujo, and R.B. Frankel, (1982a) *J. Appl. Phys.* 53, 2727-2729.
- Safarik, I. and M. Safarikova (2002), *Monats. Fur Chem.* 133, 737-759.
- Schüler, D. and E. Baeuerlein (1996), *Arch. Microbiol.* 166, 301–307.
- Schütz, G., W. Wagner, W. Wilhelm, P. Kienle, R. Zeller, R. Frahm and G. Materlik (1987), *Phys. Rev. Lett.* 58, 737-740
- Schütz, G., P. Fischer, E. Goering, K. Attenkofer, D. Ahlers and W. Röhl (1997), *Synchrot. Rad. News*, 10(4), 13-26.
- Sette, F., C.T. Chen, Y. Ma, S. Modesti and N.V. Smith (1990), *AIP* 215, 787-795.
- Simpson, E.T., T. Kasama, M. Posfai, P.R. Buseck, R.J. Harrison and R.E. Dunin-Borkowski (2005), *J. Phys. Conf. Ser.* 17, 108-121.
- Song, H.-P., X.-G. Li, J.-S. Sun, S.-M. Xu and X. Han (2008), *Chemosphere*, 72, 616-621.
- Staniland, S., B. Ward, B. A. Harrison, G. van der Laan and N. Telling (2007), *Proc. Natl. Acad. Sci. USA* 104, 19524-19528.
- Staniland, S., W. Williams, N. Telling, G. van der Laan, A. Harrison, G. and B. Ward (2008), *Nat. Nanotechnol.* 3(3), 158-162.
- Stöhr, J. (1992), *NEXAFS Spectroscopy*, Springer Series in Surface Sciences, Vol. 25, Springer-Verlag, Berlin Heidelberg New York.
- Stöhr, J. (1995), *J. Electron Spectrosc.* 75, 253-272.
- Stöhr, J. (1999), *J. Magn. Magn. Mater.* 200, 470-497.
- Stöhr, J., *Magnetic Dichroism Spectroscopy and Microscopy*. Accessed: 5 January 2010, from: <http://www-ssrl.slac.stanford.edu/stohr/xmcd.htm>
- Stolz, J. F., S.-B.R. Chang and J.L. Kirschvink (1986), *Nature*, 321, 849–851.

- Stolz, J.F., D.R. Lovley and S.E. Haggerty (1990), *J. Geophys. Res.* 95, 4355-4362.
- STXM 5.3.2 User Manual, Advanced Light Source, Berkeley California, (version April 2003).
- Taylor, A.P. and J.C. Barry, J.C (2004), *J. Microsc.* 213, 180-197.
- Telling, N.D., V.S. Coker, R.S. Cutting, G. van der Laan, C.I. Pearce, R.A.D. Patrick, E. Arenholz and J.R. Lloyd (2009), *Appl. Phys. Lett.* 95, 163701-1/3.
- Thole, B.T., G. van der Laan and G.A. Sawatzky (1985), *Phys. Rev. Lett.* 55, 2086-2088.
- Thole, B.T., P. Carra, F. Sette and G. van der Laan (1992), *Phys. Rev. Lett.* 68, 1943-1946.
- Thomas-Keprta, K.L., D.A. Bazylinski, J.L. Kirschvink, S.J. Clemett, D.S. McKay, S.J. Wentworth, H. Vali, E.K. Gibson Jr. and C.S. Romanek (2000), *Geochim. Cosmochim. Acta*, 64(23), 4049-4081.
- Thomas-Keprta, K. L., S.J. Clemett, D.A. Bazylinski, J.L. Kirschvink, D.S. McKay, S.J. Wentworth, H. Vali, E.K. Gibson Jr., M.F. McKay and C.S. Romanek (2001), *Proc. Natl Acad. Sci. USA* 98, 2164–2169.
- Thomas-Keprta, K. L., S.J. Clemett, D.A. Bazylinski, J.L. Kirschvink, D.S. McKay, S.J. Wentworth, H. Vali, E.K. Gibson Jr. and C.S. Romanek (2002), *Appl. Environ. Microbiol.* 68, 3663–3672.
- Thompson, A.C., D.T. Attwood, E.M. Gullikson, M.R. Howells, J.B. Kortright, A.L. Robinson, J.H. Underwood, K.-J. Kim, J. Kirz, I. Lindau, P. Pianetta, H. Winick, G.P. Williams, J.H. Scofield, and D. Vaughan (2001), Center for X-Ray Optics and Advanced Light Source, *X-ray Data Booklet*, Lawrence Berkeley Lab, Rev. 2.
- Thornhill, R.H., J.G. Burgess, T. Sakaguchi, and T. Matsunaga (1994), *FEMS Microbiol. Lett.* 115, 169–176.
- Towe, K. M. and T.T. Moench (1981), *Earth Planet. Sci. Lett.* 52, 213–220.

- van der Laan, G., B.T. Thole, G. Sawatzky, J.B. Goedkoop, J.C. Fuggle, J.M. Esteve, R. Karnatak, J.P. Remeika and H.A. Dabowska (1986), *Phys. Rev. B*, *34*, 6529-6531.
- van der Laan, G and B.T. Thole (1991), *Phys. Rev. B*, *43*, 13401-13411.
- van der Laan, G. and L.A. Welbourne (1996), *Endeavour*, *20*, 37-41.
- Walcott, C., J.L. Gould and J.L. Kirschvink (1979), *Science*, *205* (4410), 1027-1029.
- Walker, M.M., J.L. Kirschvink, S.-B.R. Chang and A.E. Dizon (1984), *Science*, *224*, 751-753.
- Walker, M.M., T.P. Quinn, J.L. Kirschvink and C. Groot (1988), *J. exp. Biol.* *140*, 51-63.
- Wang, J., G.A. Botton, M.M. West and A.P. Hitchcock (2009a), *J. Phys. Chem. B*, *113*, 1869-1876.
- Wang, J., C. Morin, L. Li, A.P. Hitchcock, A. Scholl and A. Doran (2009b), *J. Electron Spectrosc.* *170*, 25-36.
- Winklhofer, M., L.G. Abraçado, A.F. Davila, C.N. Keim and H.G.P. Lins de Barros (2007), *Biophys. J.* *92*, 661-670.
- Zoeger, J., J.R. Dunn and M. Fuller (1981), *Science*, *213*, 892- 894.